5-2018

Graphene Foam and Helically Coiled Carbon Nanotubes as Electrodes in Energy Storage Devices

Anthony Childress
Clemson University, achil010@gmail.com

GRAPHENE FOAM AND HELICALLY COILED CARBON NANOTUBES AS ELECTRODES IN ENERGY STORAGE DEVICES

A Dissertation
Presented to
the Graduate School of
Clemson University

In Partial Fulfillment
of the Requirements for the Degree
Doctor of Philosophy
Physics

---

by
Anthony Childress
May 2018

Accepted by:
Dr. Apparao M. Rao, Committee
Chair Dr. Ramakrishna Podila
Dr. George Chumanov
Dr. Terry Tritt

ABSTRACT

Since their inception, carbon nanomaterials have been exploited for use in energy storage. The discovery of carbon nanotubes and the later isolation of graphene opened new avenues in electrode research for batteries and electric double layer capacitors (EDLCs). Their combination of flexibility, mechanical robustness, and electronic conductivity make them ideal for use as active materials and additives. My research has focused on the synthesis and implementation of helical carbon nanotubes (HCNTs) for supercapacitors and few-layer graphene in the form of graphene foam (GF) for aluminum-ion batteries. The presence of defects and dopants was controlled in each system to determine how they relate to the performance of the electrode materials. For each material, Raman spectroscopy served as a key analytical tool. Over the past two decades, the Raman modes of carbon nanotubes and graphene have been well characterized and their relation to various aspects of the graphitic lattice such as defect density, dopant type, and lattice constants have been determined. I used these characteristics to correlate material properties to electrode performance.

In the first chapter, I give an overview of the properties and energy storage applications of graphene and carbon nanotubes. The second chapter concerns the basic information needed to understand the electrochemical and spectroscopic methods used to analyze the samples, as well as the instrumentation and equipment used for measurements. In the third chapter, I discuss graphene foam cathodes as used in aluminum-ion batteries. For the graphene foam studies, the methods of producing the foams and Al-ion battery components were optimized before beginning electrochemical characterization, and are

described in section 3.1.2. The intercalation process of the chloroaluminate anions was studied by in situ Raman spectroscopy applied to charge/discharge cycling of the cells. The role of surface defects and nitrogen dopants in the performance of few-layer graphene was studied using this method and correlated to performance using several electrochemical techniques.

The fourth and final chapter details my work with HCNTs. I first synthesized them using chemical vapor deposition methods which are commensurate with scalable processing, as described in section 4.2. They were prepared for electrochemical testing in two forms: vertically aligned arrays of various heights on metal substrates and freestanding entangled carpets known as buckypapers. They were then characterized spectroscopically and electrochemically and found to possess superior performance to that of linear carbon nanotube analogues. The HCNT buckypapers were also found to be superior scaffolds for polymer composites by virtue of retaining a greater mass loading of polymer, leading to improved capacitance.

DEDICATION

I dedicate this work to the memory of my father Brock Childress, to the memory of my grandfather John C. Henry, to my brother Brock Childress jr, and to my mother Michele Greene who has always encouraged me in my endeavors.

ACKNOWLEDGEMENTS

I would first like to acknowledge my advisor Dr. Apparao Rao, who gave me a second chance by allowing me to join his group in 2012. His guidance has made me a better scientist and person. I thank Dr. Ramakrishna Podila for his optimism and his insights on many things. I thank the other members of my committee, Dr. George Chumanov and Dr. Terry Tritt for the classes they have taught and the enthusiasm of their lectures.

I acknowledge my mother who never fails in her support. I must of course acknowledge the friends I have made during my time in Clemson. Chris Cortis, who has always extended me his hospitality and encouraged my studies. Ethan Kilgore, who is always ready to help in any situation. Chris Moore and Tara Lenertz, who provided much entertainment and who I hope continue their good life together. Sai Sunil Mallineni, with whom I spent several late nights working through homework problems, and whose food was always too spicy.

The support and efforts of all my coworkers at the Clemson Nanomaterials Institute is also greatly appreciated. Thank you to Herbert Behlow and Sriparna Bhattacharya for their help with editing this dissertation and for their daily efforts in the lab. A special thanks is given to Lakshman Ventrapragada, Fengjiao Liu, and Longyu Hu for help with sample preparation and characterization, and my predecessors Dr. Mehmet Karakaya, Dr. Deepika Saini, and Dr. Jingyi Zhu who taught me many techniques and served as good role models.

TABLE OF CONTENTS

Page

Page

Page

LIST OF FIGURES

Figure Page

Figure Page

Figure Page

Figure Page

Figure Page

LIST OF ABBREVIATIONS

$AlCl_3$: Aluminum trichloride, the precursor of the anionic component in EMI-$AlCl_4$ ionic liquid

BP : Buckypaper

CNT : Carbon Nanotube

CV : Cyclic Voltammetry

EIS : Electrochemical Impedance Spectroscopy

EMI : 1-ethyl-3-methylimidazolium, the cation of EMI-$AlCl_4$ ionic liquid

GIC : Graphite Intercalation Compound. Donor and Acceptor types refer to whether the intercalated species donates electrons to or accepts electrons from the graphene sheets.

HCNT : Helically Coiled Carbon Nanotube

MWNT : Multi-Wall Carbon Nanotube

N-FLG : Nitrogen doped Few Layer Graphene

Phonon modes iTO, oTO, LO, LA, iTA, oTA : the *i* and *o* are for *in* plane and *out* of plane, *T* and *L* are for transverse and longitudinal, *O* and *A* are for optical and acoustic.

PTFE : polytetrafluoroethylene

SEI : Solid-Electrolyte Interphase- occurs due to the breakdown of organic electrolytes during initial charge cycles of a battery.

SWCNT : Single-Wall Carbon Nanotube.

$TEABF_4$: Tetraethylammonium tetrafluoroborate, a salt commonly used in organic electrolytes.

VACNT : Vertically Aligned Carbon Nanotube array, composed of aligned MWNTs grown vertically from a substrate.

CHAPTER 1: GRAPHENE AND CARBON NANOTUBES

1.1 STRUCTURE AND PROPERTIES

Graphene is composed of a single layer of carbon atoms arranged into a hexagonal crystal structure. Single layer graphene was first isolated in 2004, and it was the only two-dimensional material available for study at that time.[1] Early investigations revealed the unique properties of graphene that arise from its low dimensionality. These include ballistic electron and hole transport reaching a mobility of 15,000 $cm^2\ V^{-1}\ s^{-1}$ [2,3], high room temperature thermal conductivity of 5300 $W\ mK^{-1}$ [4], and linear energy dispersion about the K-point of the Brillouin zone. The crystal structure of graphene is shown in Fig. 1.1a where the dark and light circles indicate inequivalent carbon atoms within the diamond-shaped unit cell. The first Brillouin zone is displayed in Fig. 1.1b, which is also hexagonal in shape. The key points within the Brillouin zone are the zone center marked by Γ and the *K*-point where the valence and conduction bands meet. In single layer graphene, the bands do not overlap at the *K*-point, making it a zero-bandgap semiconductor. Conversely, few-layer graphene is a semimetal with a band overlap of ~40 meV. By virtue of having only two atoms in its unit cell, graphene has six phonon branches as shown in Fig. 1.1c. There are three acoustic and three optical phonon branches. The LO and iTO modes are Raman active while the oTO mode is infrared active. The electronic energy bands and phonon dispersion of graphene are closely connected due to the high degree of electron-phonon coupling. Focus has also been given to the relation between the material properties and

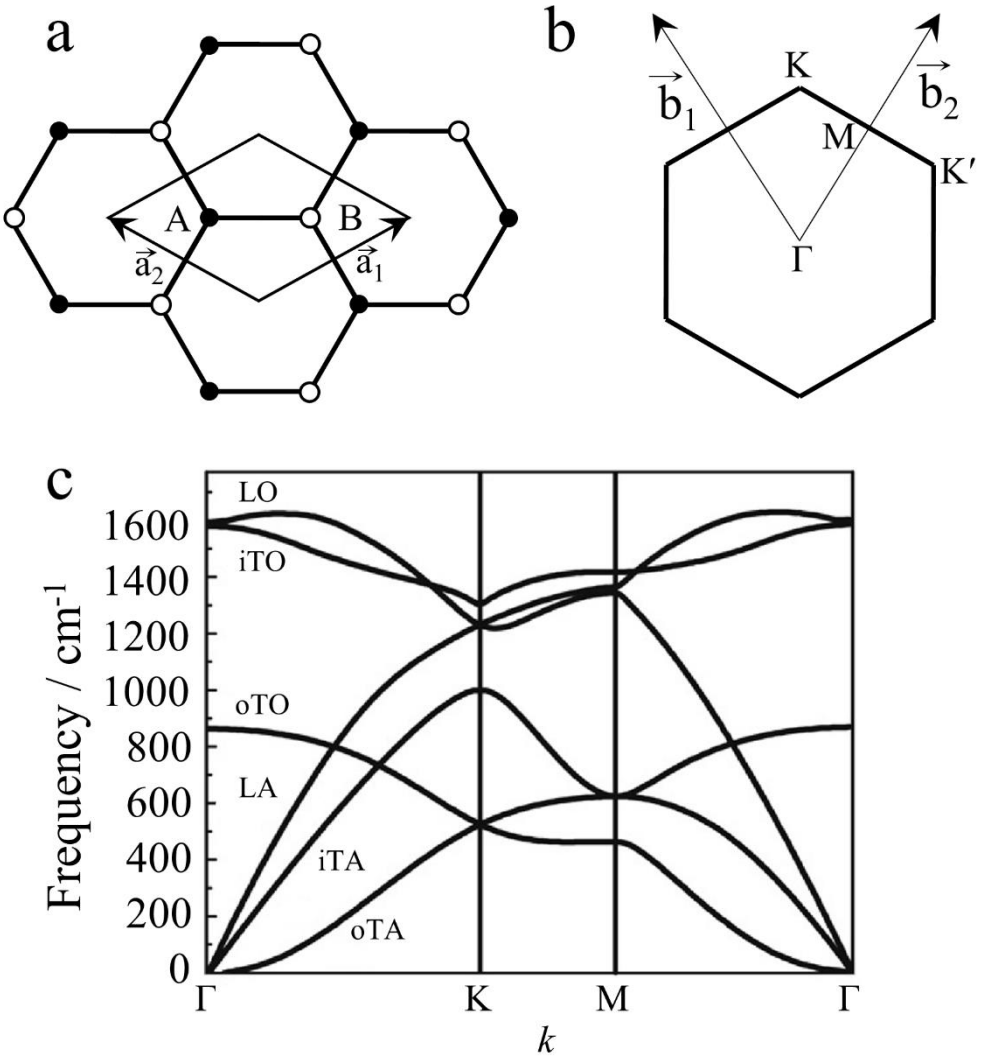

Figure 1.1: a) Two-dimensional crystal lattice of graphene. "A" and "B" represent carbon atoms within the repeat unit. b) Brillouin zone of graphene, showing various points of symmetry within the zone as well as the reciprocal lattice vectors. c) Phonon dispersion within the Brillouin zone.

defects. The influence of defects is a matter of great importance for graphene, as its two-dimensional nature makes its properties very sensitive to alterations at its surface. These aspects will be explored in more detail in sections 3 and 4.

A SWCNT is a one-dimensional nanostructure in the shape of a seamless, hollow cylinder formed from a single layer of graphite, otherwise known as graphene. The crystal lattice of graphene is composed of only carbon atoms arranged in a hexagonal pattern, thus seamless SWCNTs can only be formed from certain orientations of the lattice such that the edges of the hexagons mesh perfectly. This lattice orientation defines the chirality of the SWCNT and has a large effect on its optical and electronic properties. For instance, the chirality dictates whether a SWCNT will be metallic or semiconducting, and the bandgap of a SWCNT is highly dependent upon its diameter and chirality.[5] Being that a SWCNT is made from a graphene sheet, it possesses essentially the same phonon dispersion and electronic band structure as graphene. An important difference between the two arises because of their difference in dimensionality. While graphene is a two-dimensional material, a SWCNT is a one-dimensional quantum wire and thus has a different density of electronic states. In a CNT, the density of states takes on a more discrete nature, and the electronic energy levels occur at Van Hove singularities. While SWCNTs can be either metallic or semiconducting depending on their chirality and diameter, this is not the case for a multi-wall carbon nanotube (MWNT). A MWNT is composed of concentric SWCNTs with an interlayer spacing of ~0.34 nm, similar to turbostratic graphite. The electronic coupling between the nested SWCNTs results in MWNTs being always metallic, though it has been found that externally applied current tends to only pass through the outermost tube.

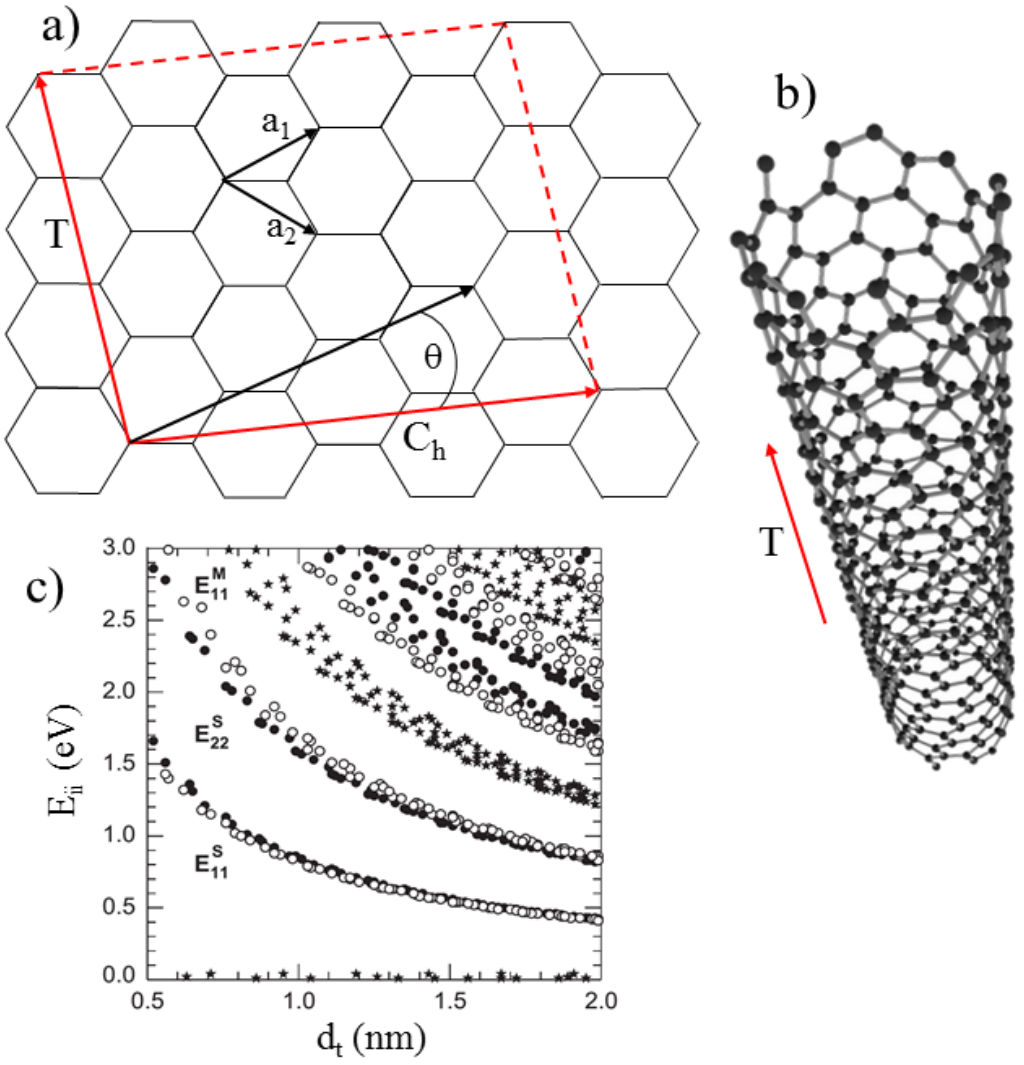

Figure 1.2: a) Diagram showing the formation of a nanotube from graphene. The parallelogram formed by the translational (T) and chiral (C_h) vectors is the repeat unit of the SWCNT. b) A SWCNT showing T directed along its axis. c) A Kataura plot showing electronic transition energies as a function of SWCNT diameter, from reference[5].

1.2 GRAPHENE AND CARBON NANOTUBES IN ENERGY STORAGE

Due to their mechanical strength, chemical stability, and high electrical and thermal conductivities, CNTs and graphene have received a great deal of attention for use as electrode materials in both supercapacitors and batteries. In this section, I will introduce the general principles of EDLCs and batteries, and mention how graphene and CNTs can be used to their benefit.

1.2.1 EDLCs

A capacitor is an energy storage system that functions via the principle of electrostatic interactions. When a potential is applied across two conductive electrodes separated by a dielectric medium, opposing charges will build up on the surface of each electrode as shown at the top of Figure 1.3. The amount of charge stored per volt applied is called the capacitance, and it depends on the surface area of the conductive electrodes, the distance between the electrodes, and the dielectric constant of the material separating the electrodes. The stored charge can be accumulated and discharged very quickly, meaning capacitors can achieve very high power densities. In order to maximize the capacitance, the conductive surface area should be maximized while the distance between electrodes should be minimized. This can be accomplished by allowing the charge separation to take place across the interface of an electronically conductive solid and a liquid electrolyte that has a high concentration of dissolved ions. The interface is known as the electric double layer and capacitors that use this approach are known as electric double layer capacitors (EDLCs) or supercapacitors. The ions in the electrolyte are not as neatly arranged at the

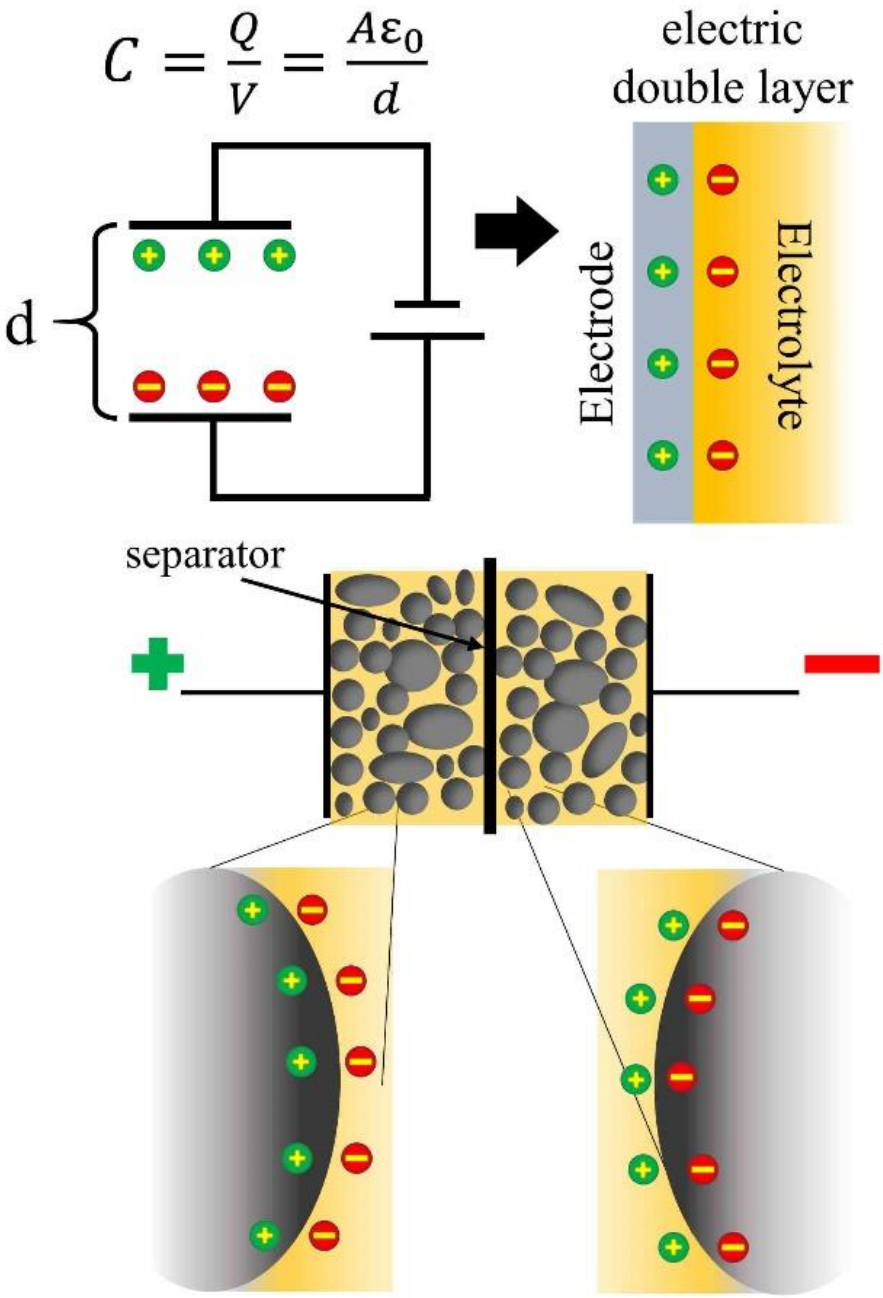

Figure 1.3: Top) A depiction of the electric double layer where charge is stored in EDLCs. Bottom) A depiction of the high surface area active material of a symmetric EDLC showing two capacitive surfaces in series.

interface as depicted in Fig. 1.3. When a potential is present across the interface, the ions will form what is known as a diffuse layer, as described in the Gouy-Chapman-Stern theory of the double layer.[6–8] The diffuse layer forms due to the interplay of electrostatic attraction at the electrode surface and thermal diffusion of the ions in the electrolyte. Ion concentration is greatest at the surface of the electrode and will gradually decrease with distance from the interface until the bulk concentration is reached. The thickness of the diffuse layer will vary depending on the applied potential and ion concentration, and is less than a nanometer thick for concentrations typically used in EDLCs (>0.1 M). It is important to note that the positive and negative electrode both display the double layer, meaning that they act as two capacitors in series. This series configuration must be accounted for when calculating the specific capacitance for an electrode material in a symmetric EDLC.

EDLCs are capable of storing more charge than traditional electrolytic capacitors, but their voltage range is limited by the need for a suitable electrolyte. Water is often used as an electrolyte medium, but it has a rather small voltage window of ~1.2 V, meaning the electrolyte will begin to decompose if this limit is exceeded. Electrolyte media are typically composed of a mixture of organic solvents that grant a larger voltage window than water. These include several types of alkyl carbonates, dioxolane, and acetonitrile. Even larger voltage windows are possible through the use of ionic liquids as electrolytes. They also posess greater heat capacity and negligible vapor pressure, making them much safer to use compared to flammable organics. However, ionic liquids tend to be more expensive and posess higher viscosity and slower diffusion kinetics due to greater coulomb interactions within the liquid. For all the work completed herein, I used only simple electrolytes. For

EDLCs, I have used $TEABF_4$ dissolved in acetonitrile, while for AIBs, I have used the ionic liquid $EMI{\cdot}AlCl_4$ as required for the cell chemistry.

Activated carbon is the standard material used in EDLC electrodes. It possesses a very large surface area on the order of 2000 $m^2\ g^{-1}$ and is very low cost. The high surface to mass ratio of activated carbons is due to the presence of micropores within the structure. Pores that are smaller than ~2 nm in size are classified as micropores, and the presence of such micropores has been linked to the performance of activated carbons.[9] The activated carbon is combined with conductive additives, binders, and adhesives and then mixed into a slurry before being applied to a current collector that is usually aluminum. It is this mixture of components that is the focus of nanomaterial integration into EDLCs.

One of the first commercial uses of CNTs was as a conductive filler in polymer composites. The CNTs granted enough conductivity to dissipate electric charge while also leading to better mechanical properties at lower mass loading than the carbon black that is typically used.[10] CNTs also serve to improve the conductivity in EDLC electrodes. Despite having a lower specific surface area than activated carbon, CNT based electrodes are able to achieve higher capacitance. This is thought to be due to the greater open space within CNT bundles comprising an electrode, thus allowing better electrolyte access.[11,12] The ability of CNT based EDLCs to maintain capacitance at high discharge rates and frequencies further emphasizes the importance of mesopores (pore diameter >2 nm), as the micropores in activated carbon are simply not large enough to accommodate the flow of ions at high flux rates. A further means to improve capacitance and rate capability is to use aligned CNTs that are directly connected to a current collector. In this

orientation, more CNT surface area is exposed to the electrolyte, and the electrolyte is free to pass between the CNTs. The high carrier mobility of the CNTs allows their length to be leveraged so that each CNT can take part in energy storage.[13–15]

Graphene has also been considered for use in EDLCs. With a theoretical specific surface area of 2,675 $m^2 g^{-1}$ leading to a theoretical capacitance of 550 F g^{-1},[16] graphene should be an ideal material for EDLCs. However, it has proven difficult to translate the high theoretical values into practical results. The theoretical limits are determined by considering graphene to be a plane, whereas such planar geometry is not readily achievable in an EDLC electrode which is typically ~100 μm thick, conductive throughout its volume, and must allow electrolyte to access the active surface area. For electrodes made from a slurry of graphene or reduced graphene oxide flakes, charge/discharge cycling tends to cause the flakes to realign, leading to a loss of active surface area. One method to overcome this issue has been to use exfoliated graphite oxide that has been treated with KOH.[17] Slurries made from this material have high specific surface area (~2000 g m^{-2}) and the flakes produced by KOH activation are more twisted in shape, preventing reshuffling of flakes during cycling. Other graphene media such as aerogels and foams possess too much void space and thus not enough active surface area to be practical at large sizes where the mass of electrolyte would become considerable.

1.2.2 BATTERIES

In a battery, energy is not stored through simple electrostatic separations, but through chemical reactions or charge transfer between an intercalated ion and the electrode

material. Energy is stored and released by reactions wherein the oxidation state of the active chemical species is changed. This reaction can only proceed if an electric circuit external to the cell is completed, thus allowing electrons to move freely between the electrodes and compensating the internal migration of ions. The potential difference that evolves within the cell will be explained in section 2.1.

Though graphene may not be an ideal candidate for EDLCs, graphitic materials have proven very useful as energy storage media for batteries. Graphite and few-layer graphene have been used as storage media for many different ions. It functions by allowing ions to nest between the graphene layers, a process called intercalation which will be discussed in section 2.1.1. Lithium is often the ion of interest due to the ubiquity of lithium-ion battery technology, but others such as sodium, potassium, magnesium, and aluminum derivatives have been considered. In chapter three, I will discuss the use of FLG as a storage medium for chloroaluminate anions. Beyond being used as the storage medium, graphene can also be used to enhance other battery electrode materials. Silicon has a large capacity for the storage of lithium ions, making it a material of great interest in battery research. However, the large expansion of Si during cycling leads to mechanical breakdown of the electrode material, resulting in a very poor lifetime. Graphene has been used to mitigate this issue by wrapping the electrode particles, thus granting them cohesion during cycling and improved electrical conductivity between particles.[18–20] Graphene has also been used to make flexible electrodes with mixed success. Such electrodes are often made from graphene papers prepared through filtration and augmented with other nanomaterials.[21]

Carbon nanotubes have found extensive use in battery electrodes and several review articles have been written on the topic.[22,23] In the simplest application, small amounts of MWNTs can be added to the electrode slurry of a Li-ion battery for improved mechanical properties and conductivity, leading to greater rate capability and more robust electrodes with longer lifetimes. More exotic methods have also been used to incorporate CNTs. The mesoporous structure of CNT arrays has proven useful in Li-S batteries. They allow the sulfur to be sequestered away from direct contact with the electrolyte while the redox reactions take place through a CNT barrier, preventing the formation of polysulfides.[24] MWNTs can be used as templates to create coaxial CNT-SnO_2 anodes for Li-ion cells,[25,26] and they can be mixed with Si nanoparticles to reduce structural damage of Si due to expansion and contraction during cycling.[27] VACNTs can be coated with silicon and carbon to make Li-ion anode material.[28]

From this brief overview of energy applications, the diverse benefits of graphene and CNTs can be seen. More specific applications that are germane to the respective topics of discussion will be found in chapters 3 and 4.

CHAPTER 2: CHARACTERIZATION METHODS

2.1 ELECTROCHEMICAL METHODS

The theory and application of several electrochemical techniques are outlined below. The techniques include cyclic voltammetry (CV), Electrochemical impedance spectroscopy (EIS), and galvanostatic charge/discharge cycling. Prior to the techniques is a discussion of cell potentials.

2.1.1 NOTE ON CELL POTENTIALS

The concept of the cell potential is important in analyzing the performance and features of supercapacitors and batteries. In a supercapacitor that functions solely through double layer capacitance, it is purely an electrostatic phenomenon since no chemical reactions are taking place. In this case the potential is a reactionary value that is either controlled directly or builds in proportion to the supplied current. The two electrodes of a supercapacitor cell, being made from the same material, have no inherent potential difference. However, for systems such as batteries where chemical reactions are taking place and ions are moving in and out of host materials, the concept is more complicated. Here I provide a brief introduction to the cell potential as used in battery systems.

In an electrochemical cell, the voltage is determined by the energy difference between the initial and final state of the reactants. This is quantified most conveniently by the Gibbs free energy and correlates with the stability of the chemical species formed during the reaction. When considering a battery that functions through intercalation the situation is more complicated, though the underlying thermodynamic principles are the

same. In this case the cell voltage is also dependent upon the stability of the intercalant within one electrode versus the reaction at the opposing electrode. To understand how the voltage can be controlled, we start with the simplest redox reactions.

A redox reaction involves two reactants exchanging electrons, resulting in a change in the oxidation state of each reactant. The change in oxidation state of each element can be treated as its own half-reaction. For example, consider the following redox reaction between lead and silver nitrate.

$$Pb(s) + 2AgNO_3(aq) \rightarrow Pb(NO_3)_2(aq) + 2Ag(s) \quad (1)$$

The solid lead transfers electrons to the silver, causing its oxidation number to change from 0 in the solid to +2 in the lead nitrate. This oxidation half reaction is written as

$$Pb(s) \rightarrow Pb^{2+}(aq) + 2e^- \quad (2)$$

Conversely, the silver is initially in the +1 state within the nitrate complex and is reduced to a solid after accepting electrons from the lead. This reduction half reaction is written as

$$Ag^+(aq) + e^- \rightarrow Ag(s) \quad (3)$$

Thermodynamically, this reaction will proceed if the change in Gibbs free energy ΔG between products and reactants is negative. This can be measured most directly by the electromotive force (emf) of the cell if the reaction is spontaneous, or by measuring the emf required to force the reaction to proceed if it is not spontaneous. If the reaction occurs under reversible conditions, then ΔG may be expressed as

$$\Delta G = -nFE \quad (4)$$

Where F is the Faraday constant (96.5 KJ V^{-1} mol^{-1} $(e^-)^{-1}$) and n is the number of electrons exchanged in the reaction. Note that the emf (E) will be positive if the reaction is spontaneous.

The cell emf (E_{cell}) is taken as the sum of the potentials of each half reaction, which cannot be measured individually, so we do not know the actual potential of any half reaction by itself. As a convention, the baseline of zero volts is assigned to the half reaction wherein hydrogen ions are reduced to gas as given by

$$2H^+(aq) + 2e^- \rightarrow H_2(g) \qquad E° = 0.0\ V \tag{5}$$

Now that a baseline has been set with this half reaction, the standard reduction potentials of other half reactions can be organized when they are measured counter to the hydrogen half reaction. When this is done in a practical experiment, gaseous hydrogen is bubbled through a solution and contacts an inert electrode (such as platinum) where it is oxidized to H^+ and the species in the opposing half reaction is reduced. For this reason, the measured emf values of half reactions are tabulated as standard reduction potentials ($E°$) instead of oxidation potentials. A higher standard reduction potential implies that the species is easier to reduce and thus acts as a stronger oxidizing agent. Conversely, the more negative the reduction potential, the more readily the species is oxidized and acts as a stronger reducing agent. A negative reduction potential also implies the species cannot be reduced by hydrogen under standard conditions, a stronger reducing agent would be required, one that has a lower reduction potential than the species to be reduced.

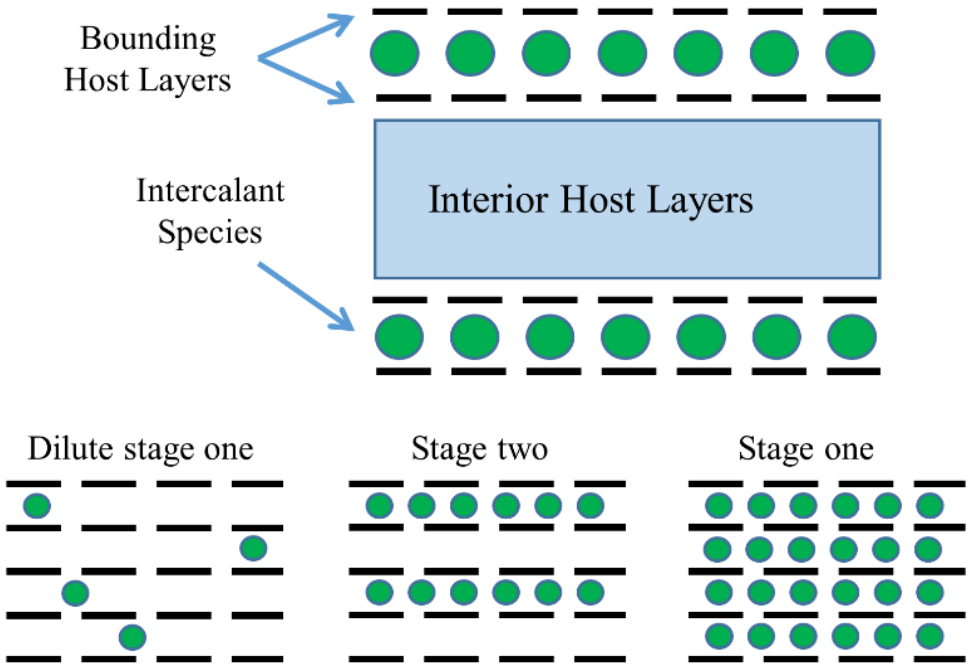

Figure 2.1: An illustration of intercalation. The upper panel illustrates bounding and interior layers of a layered structure while the lower illustrates the concept of staging in a layered structure.

If the battery is composed of two solid electrodes where the reaction occurs through plating and stripping of metals or the formation of polymers, the energetics are as explained above. However, in the case of ion intercalation into one or both electrodes, as in batteries, the energetics of the redox mechanism becomes more complicated. The concept of intercalation is illustrated in Fig. 2.1 and is a very important aspect of energy storage in batteries. Intercalation is the process by which ions in the electrolyte embed themselves within the host crystal structure of the active material to facilitate the charge transfer

process. Many materials are used as host structures in energy storage research. These include lithium iron phosphate, vanadium oxide, titanium dioxide, lithium nickel manganese cobalt, sulfur, silicon, and graphite. Among these, graphite is one of the most common. Graphite is a layered structure, though intercalation host media need not be layered. The layering of graphite gives rise to the phenomenon of staging, which is illustrated in the lower portion of Fig. 2.1.[29,30] In staging, intercalant species tend to enter into the gallery space (the space between adjacent layers) of the host material at the same sites, leading to intercalation materials forming their own interstitial layers. From a thermodynamic perspective, staging occurs because once an opening in the gallery space of the host has been forced, it then becomes the easiest site for subsequent intercalant species to infiltrate the host. The cell voltage is still determined by the chemical potential difference between the final and initial states of the system, but when intercalation is present, more interactions must be considered. For a layered structure, the energy needed to shift the layers must be considered as well as the stability and mobility of the intercalated ions within the layers.[31,32] These parameters are all contained within the expression for the free energy *A*.

$$A = T\Sigma_i[(1-\sigma_i)ln(1-\sigma_i) + \sigma_i ln\sigma_i] + \Sigma_i U(\sigma_i) + {}^1\!/_2\,\Sigma_{ij} V_{ij}\sigma_i\sigma_j - \mu\Sigma_i\sigma_i \qquad (6)$$

where σ_i is the fractional occupancy of the ith layer, V_{ij} embodies the mean field repulsion of different intercalant layers, and μ is the intercalant chemical potential. The first term denotes the contribution of the entropy of mixing within a layer and the $U(\sigma_i)$ component determines the effective in-plane interactions of intercalant molecules.

The free energy can be minimized with respect to the intercalant density σ_i to yield

$$\sigma_i(min) = \frac{exp\text{^}(\frac{\mu - \frac{1}{2}\Sigma_{ij}V_{ij}\sigma_j - \Sigma_i U(\sigma_i)}{T})}{1 + exp\text{^}(\frac{\mu - \frac{1}{2}\Sigma_{ij}V_{ij}\sigma_j - \Sigma_i U(\sigma_i)}{T})} \quad (7)$$

This equation shows how changing the intercalation medium would change the cell voltage as well as its charge/discharge characteristics. The effect becomes obvious when comparing the charge-discharge curves for media of differing crystal structures.[33] If the crystal lattice is an olivine or spinel, the bonding extends throughout the crystal, reducing expansion and rearrangement during intercalation. This tight binding results in very flat, steady voltage plateaus during charge-discharge cycles. For layered structures such as vanadium oxide or graphite, the secondary bonding between layers leaves them more free to flex and expand. This instability results in sloping profiles during charge-discharge cycles due to changing site energy as intercalation proceeds. For polymers, the effect is even more pronounced, as the voltage does not form plateaus during the charge/discharge process.

2.1.2 CYCLIC VOLTAMMETRY

In cyclic voltammetry (CV), the voltage of the system is changed at a known rate, called the can rate, while the response current is measured. This is one of the most common electrochemical techniques as it is easy to execute and reveals fundamental aspects of the system under study. For the electrode-electrolyte interface found in an EDLC, the current-voltage response is modeled by a capacitor in series with a resistor. The voltage is given

by $V = IR + \frac{q}{C}$. The time derivative of this voltage yields the scan rate *v*. Integrating then yields the current as a function of time, scan rate, resistance, and capacitance.

$$I = \nu C(1 - e^{-t/RC}) \tag{8}$$

For higher scan rates, the current response will be greater. If the resistance is taken to be zero, a step function results, implying a perfect rectangle would be formed by the data during a CV trial. As the resistance increases, the sharp edges of the rectangle become more curved as seen in Fig. 2.2 below. The capacitance can be determined by dividing the area of the curve by the scan rate multiplied by twice the voltage range. For EDLCs, this is a useful technique for measuring the capacitance at different charge rates.

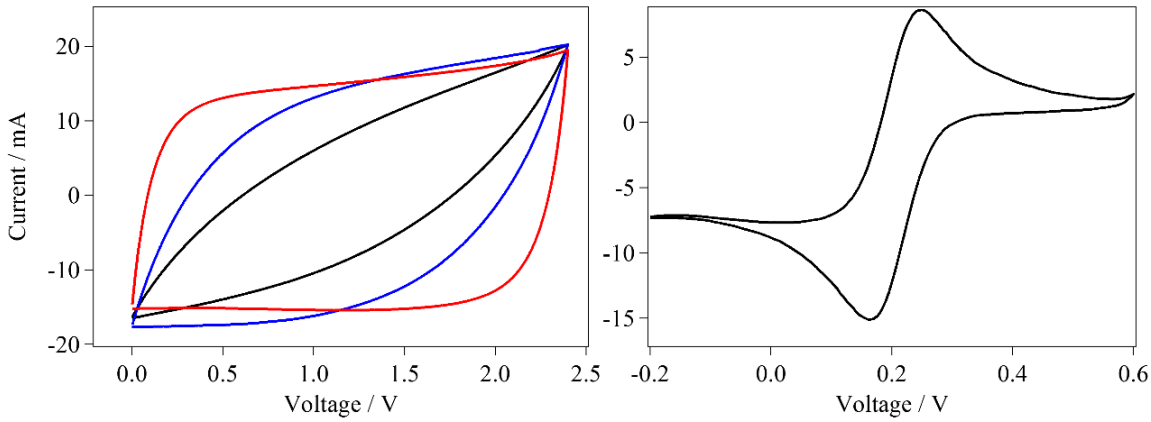

Figure 2.2: L) CV curves for three EDLCs of different resistance values. The outer curve corresponds to the most conductive electrode material while the inner curve corresponds to the least conductive material. The conductivity was adjusted by adding MWNTs to activated carbon. R) The CV trace of the potassium ferricyanide redox reaction in aqueous media. The voltage is measured with respect to a Ag/AgCl reference electrode.

For a battery, the trace will show current peaks at the voltage where a reaction occurs. This can be seen above in the right panel of Fig. 2.2. As the voltage begins to approach the point where a chemical reaction is forced, the current will begin to increase as the first components of the reaction reach the electrode surface and charge begins to be transferred. As the reaction continues, reactants build up at the electrode interface, creating a barrier through which new reactants must diffuse in order to transfer charge. This is reflected in a decrease in current after the voltage passes the peak current voltage. If the scan rate is slow, more time is allowed for the diffusion of chemical species, thus resulting in improved resolution of current peaks. Greater resolution is important in systems where multiple charge transfer processes may be taking place simultaneously or in close succession. High voltage scan rates result in wide current peaks which may overlap if redox processes occur in close proximity. When the direction of the voltage sweep reverses, the current will still be positive because the voltage is still great enough to drive the reaction in the forward direction. As the voltage begins to approach and then passes the initial reaction point, the products reform the initial reactants and the current becomes negative. The edge of the electrolyte voltage window becomes apparent when the current begins to increase very rapidly, indicating breakdown of the electrolyte solvent.

The reversibility of the reactions can also be ascertained from the CV trace. A reversible reaction is one in which the rate of electron transfer is greater than the rate of mass transfer, suggesting no significant structural reorganization takes place during the redox step. If the process is reversible, the voltage of the forward and reverse peaks will be largely independent of scan rate. The separation between the forward and reverse peaks

should be small, approximately 60/*n* mV where *n* is the number of electrons transferred per molecule during the reaction, and constant with scan rate. This essentially means the forward and reverse peaks should be mirror images of each other. For the case of a quasi-reversible reaction, restructuring takes place within the system during the redox process, but the chemical bonds of the electrodes or electrolyte are not broken. Intercalation is often a quasi-reversible process. The forward and reverse peaks are not of the same magnitude, but should have the same area within the curves. Their separation is also greater.

2.1.3 ELECTROCHEMICAL IMPEDANCE SPECTROSCOPY

One of the most useful and often misunderstood techniques used in the analysis of electronic devices is EIS.[34] In this technique, a perturbative AC voltage usually on the order of 10 mV is added to a DC voltage applied to the cell. The frequency of the AC perturbation ranges over several orders of magnitude, usually from 0.1 mHz to 100 kHz. Caution must be taken that the cell is at a relatively stable state at the applied DC voltage lest the low frequency AC perturbation drive the cell reaction, leading to suspect data in the low frequency range. The driving voltage and response current can be expressed respectively as

$$E = E_0 e^{i\omega t} \tag{9}$$

$$I = I_0 e^{i(\omega t - \phi)}$$

where ω is the frequency. The current response I is seen to lag the applied voltage by a phase factor φ. The impedance is the ratio of the time dependent voltage and current and is expressed as

$$Z = Z_0 e^{i\phi} = Z_0(cos\phi + isin\phi) \quad (10)$$

which is seen to have a real and imaginary component dependent on the phase factor φ. A plot of the response current versus the driving voltage is known as a Lissajous figure, as displayed in Fig 2.3a and from which the phase factor φ can be determined. The measured impedance response is typically plotted as the imaginary (Z″) versus real (Z′) component of the impedance (a Nyquist plot), or the magnitude of the total impedance and the phase

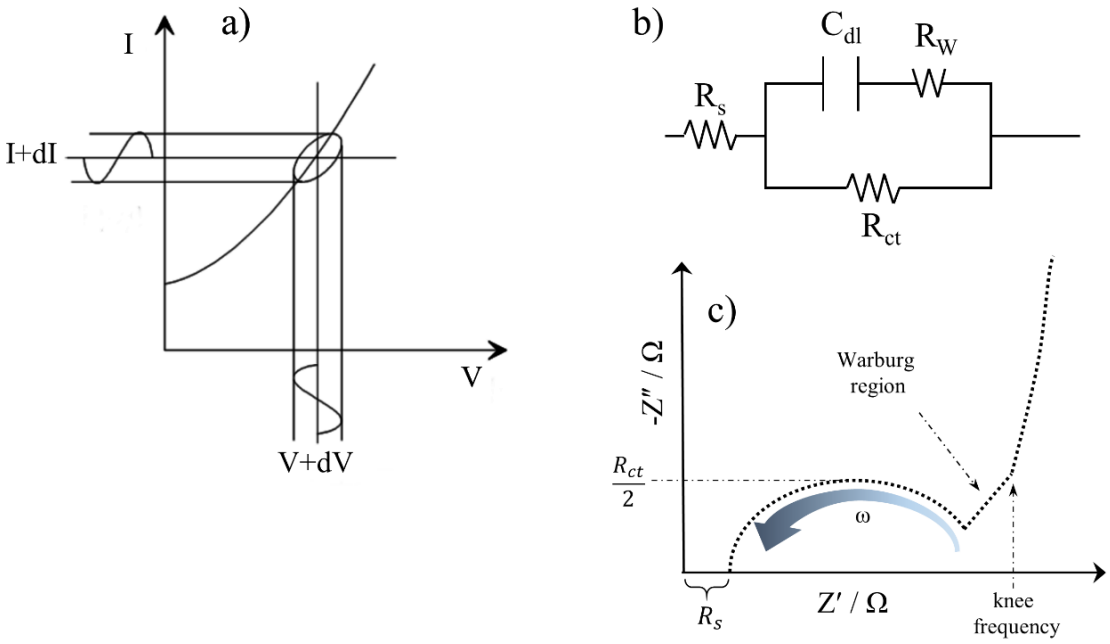

Figure 2.3: a) The Lissajous plot is formed from the time dependent voltage and current signals. It allows for the calculation of the phase factor. b) Randles cell modified with a Warburg impedance in series with the double layer capacitance. c) Nyquist plot illustrating the resistance values, knee frequency, and Warburg region. The frequency is greatest near the origin.

versus the frequency (a Bode plot), each of which emphasize different aspects of the system under investigation.

EIS has proven to be a valuable tool in analyzing battery electrodes and EDLCs. It can be used to determine the charge transfer resistance associated with redox reactions on and within electrodes, as well as the diffusion resistance, (known as the Warburg impedance), of electrolyte ions within porous structures.[35–41] The various interfaces at which redox reactions occur, and passages through which ions travel give rise to multiple time constants that appear as curves in the Nyquist plot. The plot can be fitted to a circuit model by making some assumptions about the underling mechanisms and solving a series of differential equations to yield useful quantitative information. This can be conveniently implemented through use of the Gamry Echem Analyst software. In my work, the need did not arise to accurately determine all parameters that can be derived from the Nyquist plot. A qualitative comparison of curves was enough to justify the conclusions I came upon.

Several important features are present in the Nyquist plots of capacitors and faradaic cells. For an ideal faradaic cell, the locus of points determined by the frequencies will form a semi-circle in the high-frequency region. This profile is easily derived from a parallel resistor and capacitor in series with another resistor as shown in Fig. 2.3b. For this configuration, the impedance Z is given as

$$\mathrm{Z} = \mathrm{Z}' + i\mathrm{Z}'' = \mathrm{R_s} + \frac{R_{ct}}{1+(R_{ct}\omega C)^2} - i\,\frac{R_{ct}^2\omega C}{1+(R_{ct}\omega C)^2} \qquad (11)$$

where R_{ct} is the charge transfer resistance associated with the reaction occurring between the redox active species and the electrode material. The Z'' expression can then be maximized with respect to ω and evaluated to find $R_{ct} = 2Z''(\omega_{max})$, meaning R_{ct} is twice the Z'' value found at the peak of the high frequency semi-circle. For porous electrodes, the Warburg impedance must be added as an additional element in the circuit diagram. In the Nyquist plot, it corresponds to a 45° slope at lower frequencies following the initial semi-circle. Beyond this, there is a point known as the knee frequency where the frequency is low enough to display purely capacitive behavior, and the line becomes almost vertical. At frequencies higher than the knee frequency, the resistance is highly dependent on the frequency, and capacitance is greatly diminished. The knee frequency thus marks the effective frequency range for energy storage in an EDLC.

For lithium ion batteries, or any cell wherein a solid-electrolyte interphase (SEI) is formed, it is generally accepted that the highest frequency semi-circle is due to ion diffusion through this SEI layer. Following this is a second semi-circle due to charge transfer of electrons to the ions or molecules that may be at the electrode surface or intercalated within the electrode material. The charge transfer resistance is very dependent on temperature. It will decrease as the temperature increases due to an increased transfer current density.[35] This is because the transfer current itself displays Arrhenius behavior given by

$$i_0 \, \alpha \, A_0 e^{-\frac{E_a}{kT}} \tag{12}$$

At a lower frequency than the SEI formation and charge transfer curves, a 45° sloped section of the plot is indicative of the Warburg impedance. Following this, at very low frequencies, a large curve may be found that indicates capacitance caused by the accumulation and depletion of ions within a layered electrode.[37,41] For executing EIS, a 3-electrode cell is desirable in most cases. If only two electrodes are employed, the impedance aspects of each electrode will be present in the measurement, thus convoluting the desired data.[42]

2.1.4 CHARGE/DISCHARGE CYCLING

The simplest method of evaluating the life span of a cell is to charge and discharge it within the optimal voltage range for many cycles and observe how the capacity and efficiency change over during the process. It is an easy test to perform, though very time consuming, as the cycling can last many hours or several days. For batteries and EDLCs, it is typical to observe large changes of the efficiency and capacity during the first few cycles due to an initial breakdown of electrolyte, intercalation, or settling of active material. Discharge curves also allow for calculating the energy and power density of a cell. The discharge data are usually plotted as voltage vs. specific capacity (mA h g^{-1}) which is normalized to either the mass of the electrode materials or to the mass of the entire cell. Integrating the *V* vs. capacity curve yields the energy density in units of W h kg^{-1}. Dividing the energy density by the time necessary to discharge the cell to an arbitrary voltage yields the power density in units of W kg^{-1}. The power and energy densities can then be plotted against each other in what is known as a Ragone plot. This plot serves as a map for device

performance, comparing high energy batteries and fuel cells with high power capacitors. The ultimate goal of energy storage technology is to combine the best characteristics of batteries and capacitors in order to exceed the high power and energy output derived from burning fossil fuels. Ragone plots help to monitor progress in this regard.

2.2 RAMAN SPECTROSCOPY

When one thinks of the process of absorbance of electromagnetic energy, a picture may come to mind of an electron being excited from its position in the valence band to a particular energy level in the conduction band, after which the electron relaxes to the band edge and falls back to the valence band, releasing a new photon. This is an example of a transition between "real" states. Though analogous, the process is different for Raman scattering, which often involves transitions of excited electrons between "virtual" states. The difference between real and virtual states is best explained from a quantum mechanical perspective, but it is also informative to conceptualize the physics of the overall process using a classical approach. In this brief introduction to the subject, I will start from a classical perspective.

2.2.1 CLASSICAL DESCRIPTION

In Raman scattering, light of frequency ω_1 incident on a specimen is scattered via electron-phonon interactions, resulting in scattered light that has been shifted in frequency by ω_q. The normal modes of the crystal lattice or molecules that compose the specimen are

what determine the vibrational response to the incident light and thus ω_q. The change in energy and momentum is given by

$$E_f = E_i \pm E_q \text{ and } k_f = k_i \pm q \tag{13}$$

where *i* and *f* denote the initial and final states of the photon and electron while *q* denotes the energy and momentum of the phonon which is created or destroyed during the process. These phonons are related to how the polarizability of the medium changes due to the excitation of an electron resulting from the absorption of the incident photon. This effect on the polarizability is embodied in the electron-phonon interaction. In classical electrodynamics, the polarization of a solid $\boldsymbol{P}$ is given in terms of the polarizability tensor $\boldsymbol{\alpha}$ and the electric field $\boldsymbol{E}$ as

$$\boldsymbol{P} = \boldsymbol{\alpha} \cdot \boldsymbol{E} \tag{14}$$

where it should be noted that the electric field $\boldsymbol{E}$ is the local electric field around an atom inside the solid and not simply the incident electric field. The electric field oscillates in time with the incident field frequency ω_1 as

$$\boldsymbol{E} = \boldsymbol{E}_0 \sin(\omega_i t). \tag{15}$$

The polarizability will be modulated by the normal modes of the crystal lattice with frequency ω_q as

$$\alpha = \alpha_0 + \alpha_1 \sin(\omega_q t). \tag{16}$$

With this, the polarization induced by the incident electric field is now given by

$$P = E_0(\alpha_0 + \alpha_1\, sin(\omega_q t))\, \sin(\omega_i t) \tag{17}$$

$$P = E_0 \left[\alpha_0 \sin(\omega_i t) + \frac{1}{2}\, \alpha_1 \cos\big(\, \omega_i - \omega_q\big)\, t - \frac{1}{2}\alpha_1 \cos\big(\omega_i + \omega_q\big)\, t\right].$$

The first term in eq. 17 is for the elastic response known as Rayleigh scattering, while the other two terms show the inelastic response. The inelastically scattered light will be shifted in frequency by $\pm\omega_q$. The downshift in ω_q corresponds to a Stokes process where the excited electron relaxes by creating a phonon while the upshift corresponds to an anti-Stokes process where the excited electron absorbs a phonon before the relaxation process. All Raman measurements made herein were recorded from the Stokes process.

2.2.2 QUANTUM MECHANICAL DESCRIPTION

Quantum mechanics offers a more informative approach for formulating the Raman process. It also answers the question of why a certain normal mode would be Raman active through the use of group theory, which works nicely with the matrix manipulations common to quantum mechanics.

In the quantum mechanical formulation, Raman scattering can be expressed via perturbation theory.[43] In a first-order Raman process, the momentum change of an excited electron is neglected, so q=0 in this case. This assumption is justified by the flat band structure about the Γ-point of the Brillouin zone and the small change in electron wave vector following excitation. For an optical excitation, the photon wavelength is on the order of 10^{-7} m while the length of a repeating unit of the crystal lattice is on the order of 10^{-10} m. It follows that the change in electron wave vector (given by $k = 2\pi/x$) imparted

by an optical photon is a very small fraction of the Brillouin zone. Because q is taken to be zero, a first order process will take place at the Γ-point within the first Brillouin zone. The electron is excited to a certain state after which it relaxes within the conduction band to a virtual state before returning to the valence band concurrent with photon emission. In the framework of quantum mechanics, a virtual state is a linear combination of electron eigenstates that has a large energy uncertainty and thus very short lifetime. These first order Raman processes therefore involve only three interactions; first being electron-photon, second being electron-phonon, and lastly another electron-photon interaction. Because of this, the perturbation is third order and the intensity is given by

$$I(\omega_q, \omega_i) = \left| \Sigma_{m,n} \frac{<f|H_{eR}(\omega_q)|n><n|H_{eQ}|m><m|H_{eR}(\omega_i)|i>}{\Delta E} \right|^2 \qquad (18)$$

where m and n represent the intermediate excited electron states. The denominator is the product of the energy differences associated with each process shown in the numerator.

The dipole interaction that embodies the change in polarizability is governed by the electron-photon and electron-phonon Hamiltonians H_{eR} and H_{eQ}, that act upon the various electron states. For second-order processes where $q \neq 0$, higher order perturbations must be used which entails adding more terms to the above formula as needed. For example, many important Raman features of graphene are due to second-order processes taking place about the K-point. These can be described by a fourth-order perturbation where an electron is excited, then transferred to and from the K-point by phonons or defects, then relaxes while emitting a photon. These modes can be referred to as "double resonance" modes since there

are two scattering processes involved and thus two terms in the denominator. The double resonance explanation for certain features in the graphite Raman spectra was first proposed by Thomsen and Reich in 2000, several years before graphene was isolated.[44]

2.2.3 IMPORTANT RAMAN FEATURES OF GRAPHENE AND CARBON NANOTUBES.

Figure 2.4a shows the Raman spectra for single layer graphene. The peaks marked in the figure are caused by scattering events of different order and location within the Brillouin zone and hence convey different information. The *G*-band located at ~1580 cm^{-1} is the only feature caused by a first-order process. It arises from the in-plane transverse optical (iTO) and longitudinal optical (LO) modes of the hexagonal lattice. The iTO mode is shown in Fig. 2.4b. The transverse and longitudinal directions are taken with respect to the axis between the A and B carbon atoms in the graphene repeat unit as shown in Fig. 1.1a. In graphene, these modes are degenerate at the Γ-point and so combine to form a single peak. The vibrational frequency of these modes is dependent on the electron density in the graphene sheet, and hence charge transfer to or from the graphene layer will cause the *G*-band to shift down or up respectively. In the case of carbon nanotubes, the curvature of the tube breaks the symmetry about the Γ-point and the *G*-band is split into two peaks as can be seen in the inset showing the spectra of a SWCNT. The two peaks correspond to modes along the chiral vector and the translational vector of the tube. For MWNTs, the coupling between layers and the differing mode frequencies cause the split *G*-band to once again coalesce into a single peak. The *D*-band is located at ~1350 cm^{-1} and is caused by edge defects present in the graphene sheet. Due to momentum conservation requirements,

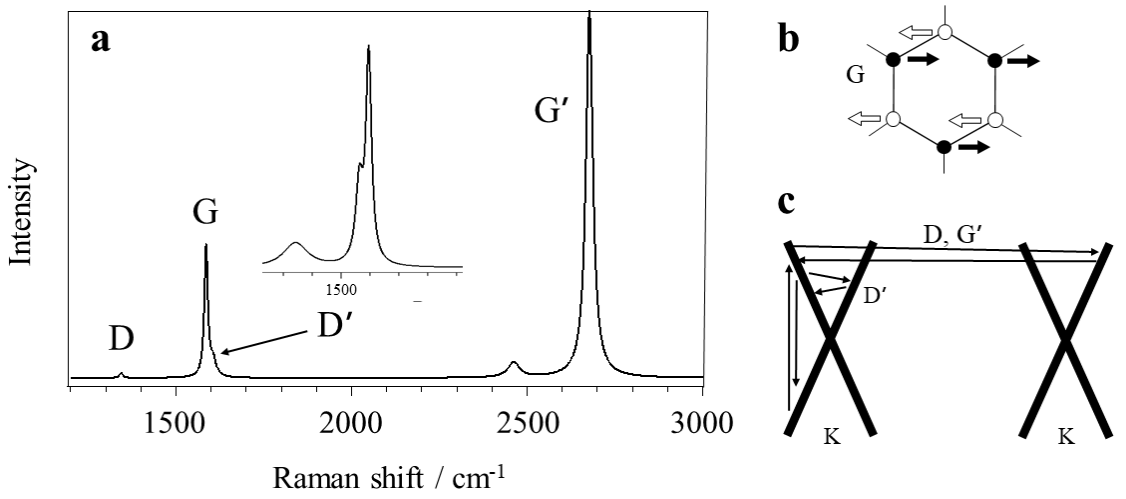

Figure 2.4: a) Raman spectra of single layer graphene. The prominent features are marked and explained in the text. The inset shows the split *G*-band of a single-wall carbon nanotube. **b**) Diagram of one of the E_{2g} vibrational modes of the graphene lattice responsible for the *G*-band, the only first-order Raman process in graphene. **c**) Diagram of second-order scattering processes taking place about the K-points in the Brillouin zone.

only armchair edge defects contribute to the *D*-band intensity. An excited electron at a *K*-point can couple to an iTO phonon and be scattered to an adjacent *K*-point then return the original point by scattering from an armchair defect. The electron could also be scattered first by a defect, then an iTO phonon. The ratio of *D*/*G* peak intensities can be used to estimate the mean distance between defects in the graphene plane, as first demonstrated by Tuinstra and Koenig for graphite.[45] The *G′*-band located at 2700 cm^{-1} is caused by a similar scattering process to the *D*-band involving two iTO phonons, hence it occurs at twice the wavenumber of the *D*-band. The *G′*-band is significant in that its shape is indicative of the number of graphene layers. When multiple layers are present, the band

structure at the *K*-points become a series of nested cones, resulting in more pathways for electron-phonon scattering. These additional pathways result in a greater width and lower intensity of the *G′*-band for multiple layers of graphene. For a single layer, the *G′*-band is sharp and of greater intensity than the *G*-band. The *D′*-band at ~1600 cm^{-1} is also due to defects, but it is not constricted by the momentum conservation rules required to access an adjacent *K*-point, hence it is related to both armchair and zigzag edge defects. In graphene, the conduction and valence bands converge at the *K*-point, where the energy dispersion relation is linear as shown in Fig. 2.4c. Due to the intersection of the bands, all Raman features related to the *K*-points are dispersive, meaning the peak positions will shift with a change in excitation energy.

2.3 INSTRUMENTATION AND EQUIPMENT

2.3.1 RAMAN SPECTROMETER

Raman measurements were carried out using a Renishaw inVia micro-Raman spectrometer. A Spectra-Physics Stabilite argon laser was used for 514.5 nm excitation, a Crystalaser diode laser was used for 532 nm excitation, and an Innovative Photonic Solutions R-type diode laser was used for 785 nm excitation. Edge filters blocked out Rayleigh scattered light below a shift of ~110 cm^{-1} for each principle wavelength. A Leica confocal microscope is used for imaging and focusing the laser on samples. Measurements were made with an objective lens with magnification of 50x and a numerical aperture of 0.75.

2.3.2 GAMRY REFERENCE 3000

Electrochemical measurements were carried out in part with a Gamry Reference 3000 potentiostat/galvanostat. The Gamry Framework software was used for controlling the instrument. It is capable of executing all basic electrochemical procedures and was here used for CV, EIS, and cycling of cells.

2.3.3 KEITHLEY 2400

A Keithley 2400 source meter was also used for electrochemical measurements. It was used for the purpose of CV measurements of AIB pouch cells and controlled charging of an AIB for in-situ Raman measurements. It was controlled through the use of LabView 2014 software. The two codes I created for CV and charge/discharge measurements are reproduced in Appendix A. Basic programs for establishing a connection with the instrument and acquiring data were found in the National Instruments VI database. From there, the programs were expanded upon to create the CV and charge control programs.

2.3.4 CELLS FOR ELECTROCHEMISTRY

For 3-electrode measurements, two different cell types were used. Both were made primarily of PTFE as it is a chemically inert insulating material. One cell, shown in Fig. 2.5, employs an open design with a 0.785 cm^2 hole in the bottom where the active material is exposed to electrolyte as the working electrode. Once the active material is secured, the top reservoir is filled with electrolyte. The counter and reference electrodes can be chosen by the user and are immersed in the electrolyte. In my work, this cell was mainly employed for measuring the capacitance of CNT arrays on steel substrates and CNT BPs, as discussed

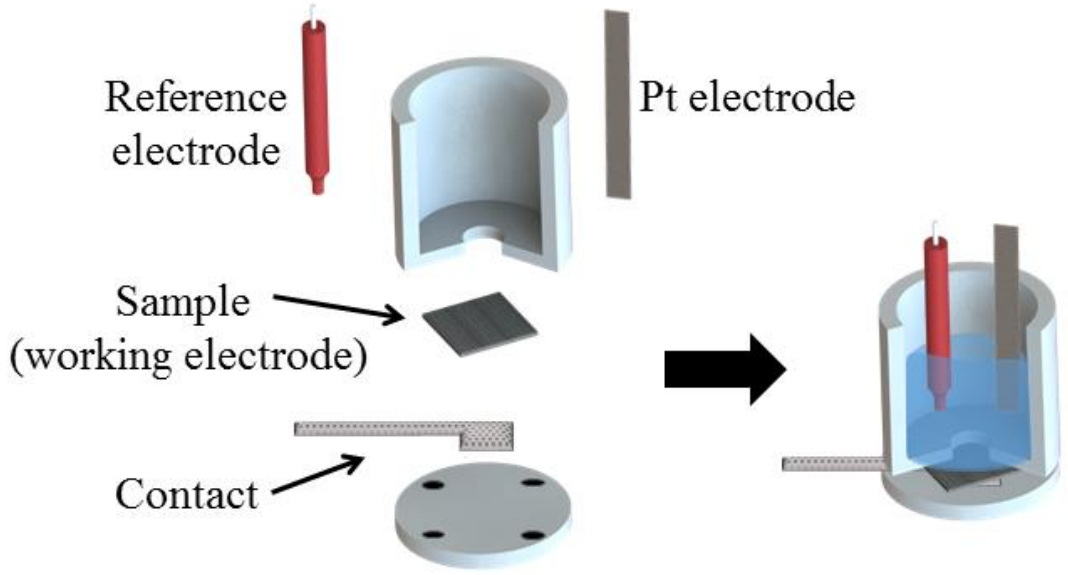

Figure 2.5: General purpose 3-electrode cell. A lid (not shown) is used to cover the electrolyte reservoir and fits over the reference and counter electrodes.

in chapter 4. The second cell type shown in Fig. 2.6 was made specifically for AIB testing. The design is taken from Song et al.[42], but with nickel used as the current collectors. The rubber O-ring makes the cell air tight and the PTFE inner sleeve keeps the ionic liquid in the center of the cell. For this cell, only a small amount of electrolyte is needed, just enough to soak the electrode materials and the separator. A typical volume of electrolyte is 0.2 ml.

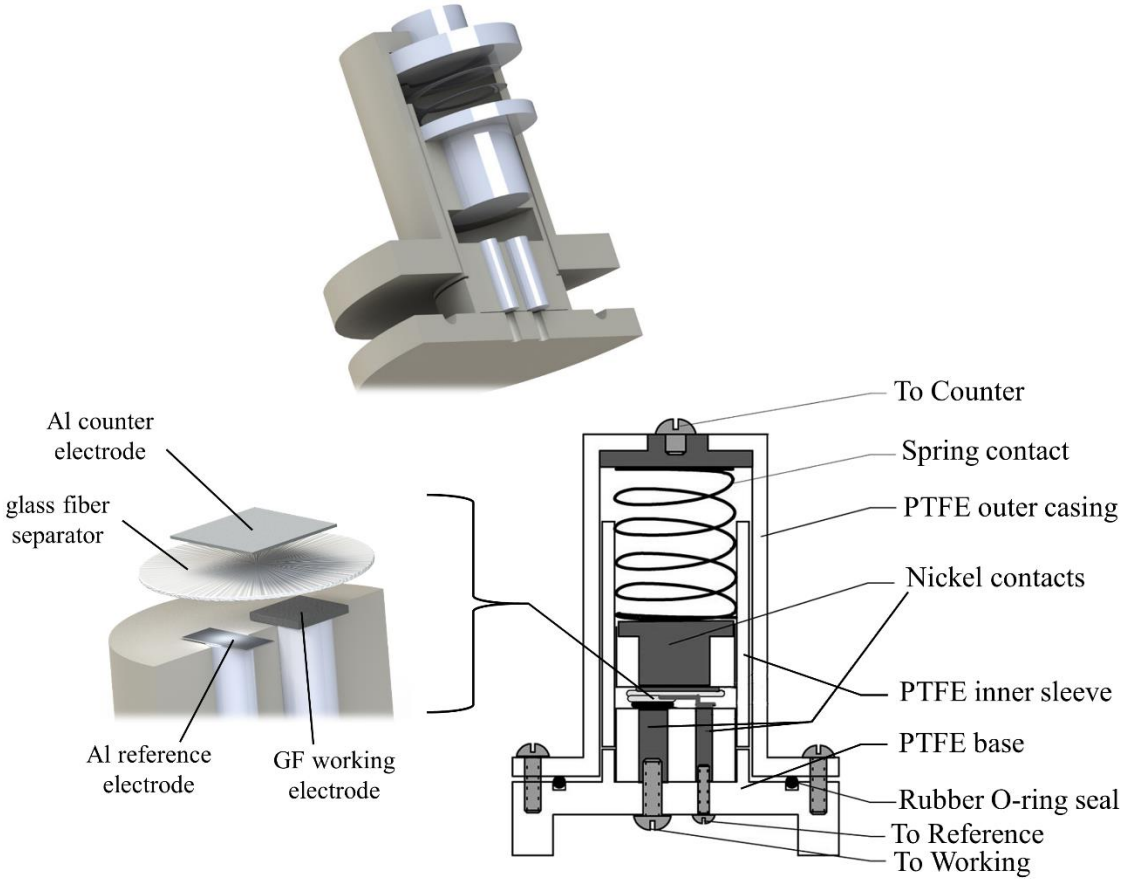

Figure 2.6: The 3-electrode cell used for testing AIBs. The top and left images are cross sectional views of the cell created in SolidWorks. The schematic on the right is modified from reference [42]. When assembled, the cell is air-tight. The nickel current collectors are not corroded within the potential range used for analyzing AIBs.

CHAPTER 3: GRAPHENE FOAM AS THE CATHODE IN AN ALUMINUM-ION BATTERY

3.1 THE ALUMINUM-ION CELL

3.1.1 INTRODUCTION

Lithium ion batteries (LIBs) have become ubiquitous with regard to products such as mobile phones, laptop computers, and electric vehicles. They currently dominate the market for these applications and much research has been devoted in recent decades to improve LIB performance. However, for future battery applications that require high power as well as high energy densities, other architectures will be required. New alternatives (e.g., Li-S, Li-air) still rely on Li metal, which is potentially unsafe and whose reserves could be depleted in as little as fifty years if the demand for electric vehicles grows as expected.[46] Choosing newer materials beyond Li is imperative for replacing environmentally harmful and volatile Li-chemistries. Aluminum has long been considered for use in battery systems as it possesses several properties that are germane to practical energy storage. It is the most abundant metal in the Earth's crust, (~8% versus 0.0065% for Li) [47], displays three-electron redox properties, and possesses a four-fold higher volumetric capacity than Li (~8040 mA h cm^{-3} vs. ~2000 mA h cm^{-3}). Research on aluminum batteries has been ongoing for decades and review articles on the subject are available in the literature.[48,49] Unfortunately, the propensity for the formation of Al_2O_3 and hydrogen gas in aqueous media precludes the use of aqueous electrolytes for a secondary Al-ion battery, though they

have been considered for use in fuel cells. To develop batteries with stable charge/discharge characteristics, aprotic electrolytes are a necessity.

In 1982, a new class of room temperature ionic liquids composed of dialkylimidazolium chloroaluminate salts was introduced which would prove to be very useful as aprotic electrolytes.[50] They were the result of work completed by Wilkes and Levisky in 1981 in the pursuit of high power thermal batteries for use by the U.S. Air Force.[51] In that work, a series of dialkylimidazolium halogen salts were tested for stability. The most useful cation of the series has proven to be 1-ethyl-3-methylimidazolium (EMI) due to its favorable electrochemical stability window and ease of preparation. When EMI·Cl is paired with a chloroaluminate salt such as $AlCl_3$, an ionic liquid is formed. The electrochemical stability window will vary with the ratio of components, but it is typically ~3 V. At the cathodic limit, the EMI^+ ion will be irreversibly reduced or Al will be plated out from $Al_2Cl_7^-$ depending on the ratio of components in the ionic liquid. At the anodic limit, chlorine gas will be produced from $AlCl_4^-$ and $Al_2Cl_7^-$. Since its discovery, the reaction mechanisms and electrochemical properties of $EMI{\cdot}AlCl_4$ have been explored in depth.[52–57] It was also found to be a good medium for electroplating aluminum which created interest in using it for aluminum battery systems.[58–62] Thus, with suitable ionic liquid electrolytes, the possibility of viable rechargeable Al-ion batteries (AIBs) caught the attention of researchers. The typical cathode material used in the AIB cells was graphite, but due to the large size of the intercalating $AlCl_4^-$ ions, the graphite cathodes suffered from disintegration during cycling. Other materials such as layered vanadium oxide were also tested, but issues such as low

cell discharge voltage, and insufficient cycle life with concomitant loss of capacity were still present with the AIB cathode.[59,61,63–68] These problems, and the sudden interest in lithium chemistries following the commercial release of the Li-ion cell in 1991 led to a decline in AIB research that would not recover for several decades.

It was only recently that Lin et al. addressed some of the problems with AIB cathodes by using EMI·$AlCl_4$ ionic liquid as the electrolyte and redox medium while replacing the standard graphite cathode with a three-dimensional few-layer graphene (FLG) foam.[62] Graphene and its derivatives have found abundant applications in energy storage research, and several recent review articles are available on the subject.[69–72] AIBs reported by Lin et al. exhibited very fast charge rates (~4 A g^{-1}) and minimal capacity loss after 700 cycles. Notwithstanding this progress, the gravimetric energy density of these AIBs still remains far below that of LIBs. Furthermore, the reaction and intercalation mechanisms between the EMI·$AlCl_4$ electrolyte and graphene layers still remain ambiguous, motivating the present investigation through detailed spectroelectrochemistry.

The following reaction, which is consistent with past research into chloroaluminate ionic liquid chemistry,[50,54–57,73] has been proposed in the literature to describe the redox and intercalation mechanisms in AIBs

$$Al + 4AlCl_4^- + 3(C_n^+ AlCl_4^-) \;\rightleftarrows\; 4Al_2Cl_7^- + 3C_n \qquad (19)$$

where the discharge process is from left to right.[59,62] While charging, Al is plated onto the anode (Al metal) via the reduction of $Al_2Cl_7^-$, and $AlCl_4^-$ ions intercalate into the cathode (FLG/graphite) lattice. During discharge, the $AlCl_4^-$ ions leave the graphite host to

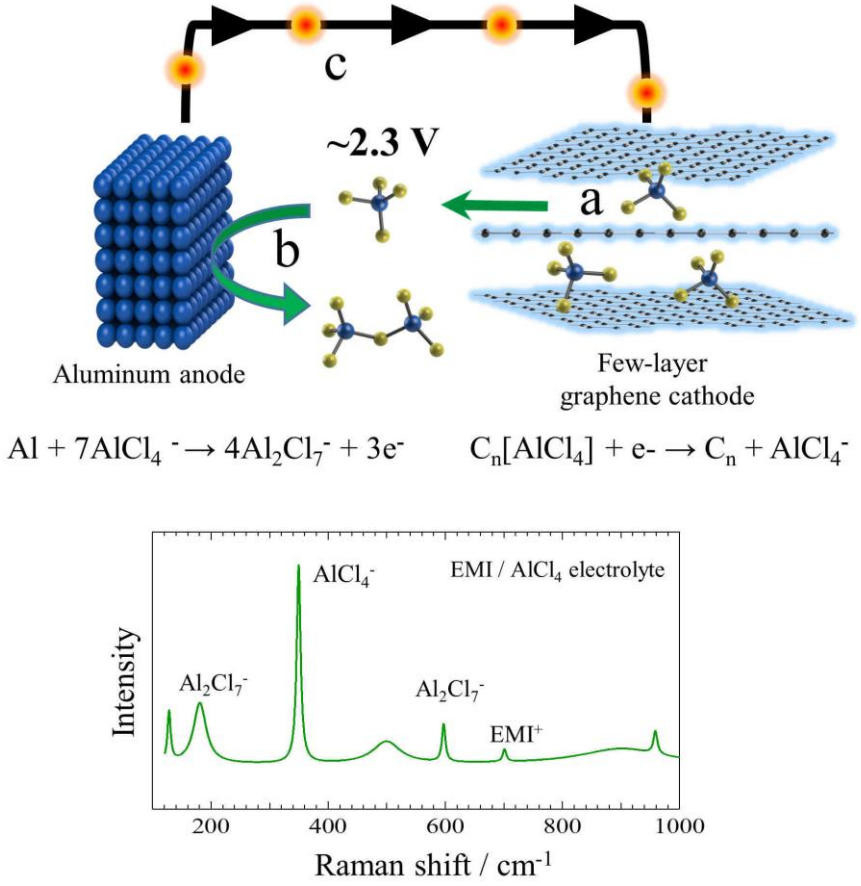

Figure 3.1: Discharge mechanism of an AIB. Note that (a), (b), and (c) occur simultaneously and are initiated by completing an external circuit which provides a path for the electrons. a) Intercalated $AlCl_4^-$ accepts electrons and is forced into solution as negative ions. b) Al metal is oxidized to Al^{3+} ions which complex with $AlCl_4^-$ to form $Al_2Cl_7^-$. c) Electrons move from anode to cathode, powering an external device. Below the schematic, the Raman spectrum for the ionic liquid is displayed.

react with the Al metal anode forming $Al_2Cl_7^-$ ions. A diagram of the AIB chemistry and the Raman spectrum [74] of EMI·$AlCl_4$ is shown in Fig. 3.1. These intercalation/de-intercalation processes in AIBs, which either limit the charge rates or expand the

FLG/graphite cathode to the point of disintegration, are poorly understood with contrasting theoretical explanations. For example, based on density functional theory (DFT) calculations, Jung et al. concluded that the pyramidal $AlCl_4^-$ ions intercalate in FLG while retaining their geometry and also stack within the gallery space between the graphene sheets.[75] In contrast, DFT studies by Wu et al. suggested that $AlCl_4^-$ ions may become planar when sandwiched between graphene layers, leading to an improved rate of ion diffusion through the cathode.[76] It has also been proposed that intercalation occurs via free Al^{3+} ions or Cl_2 molecules.[61,64]

Here, I present a comprehensive spectroelectrochemical study, along with DFT calculations, to elucidate reactions at the cathode in AIBs with Al metal anode and FLG foam cathodes in EMI·$AlCl_4$ electrolyte. The cyclic voltammograms (CVs) of the AIBs display three distinct redox processes that were concomitantly tracked using in situ Raman spectroscopy, providing insight into the intercalation/de-intercalation of the $AlCl_4^-$ ions. DFT calculations are used to model the charge transfer between the graphene sheets and the $AlCl_4^-$ ions, the results of which concur with our spectroscopic measurements. From these insights, graphene-based AIBs are fabricated with the high energy and power densities (~200 Wh kg^{-1} at 200 W kg^{-1} and ~160 Wh kg^{-1} at 5000 W kg^{-1}) that exhibit a slow decrease in energy at higher power densities.

In one of our previous works, it was shown that defects and dopants in FLG result in a shift of the Fermi energy, while pores in the outer graphene sheets allow better access to interior surface area. These features led to energy densities beyond the theoretical limit in

graphene-based supercapacitors.[77] Motivated by this work, Yu et al. fabricated AIBs using FLG foam cathodes subjected to plasma processing.[78] Their cells exhibited low charge voltage (cutoff at 2.3 V), high capacity (123 mA h g^{-1} at current of 5000 mA g^{-1}), and excellent cycling ability due to defect and nanoribbon formation. Zhang et al. have reported that the diffusion of $AlCl_4^-$ ions in FLG could be hindered due to carboxyl and hydroxyl functional groups at the edges of the basal planes through which the ions must pass.[79] In the current work, a systematic study is undertaken to understand how plasma induced surface defects may influence the reactions at the cathode. It is found that the energy and power densities of the FLG cathode, as well as the intercalation mechanism, are insensitive to in-plane surface defects as long as such defects do not significantly alter the electrical connectivity. Lastly, the effects of nitrogen doped FLG cathodes on AIB cell performance is investigated, partially motivated by the previous work on capacitors. Others have found that adding nitrogen to the graphene lattice is beneficial for cells relying on the intercalation of cations for the formation of donator-type graphite intercalation compounds (GICs).[80–82] In contrast, I show that in AIBs which rely on anion intercalation the presence of N-dopants in the FLG cathode inhibits intercalation and leads to poor cell performance

3.1.2: MATERIALS AND METHODS

The synthesis of graphene on nickel substrates is akin to a recrystallization process. Carbon, being relatively soluble in nickel and possessing a high diffusivity [83], will infiltrate the nickel at high temperatures then diffuse to the surface as the nickel slowly cools and phase separation occurs. During this cooling and diffusion process, the carbon

relaxes into a stable morphology, which is the hexagonal lattice of graphene.[84] The source of carbon is typically methane or ethane, which decompose into atomic carbon upon contact with the heated nickel surface. The grain boundaries within nickel also play an important role in growth.[84] The high surface curvature of the nickel at grain boundaries and the greater carbon solubility within the boundaries favors the nucleation of few-layer graphene. Nickel foam (MTI Corp.) was used as the substrate for the synthesis of the FLG cathodes. Several pieces of Ni foam (dia. ~16 mm, thickness ~1 mm) were placed in a 1" diameter quartz tube furnace and first annealed at 900 °C for one hour under flowing Ar (230 sccm) and H_2 (120 sccm). Next, the furnace temperature was reduced to 850 °C, and methane (100 sccm) was introduced for one hour. The furnace was then cooled to 400 °C under continued Ar flow, and allowed to dwell for two hours. The furnace was finally shut off and allowed to cool to room temperature in flowing Ar. The mass of FLG was determined by weighing the Ni foam before and after the FLG growth using a Radwag micro balance. I found that Ni foam (dia. ~16 mm, thickness ~1 mm) could be consistently loaded with ~1.1 mg of FLG using the above growth parameters. To induce defects, the FLG coated Ni foams were exposed to varying powers (25 W, 50 W, 75 W, and 100 W) of Ar plasma in a Plasma Etch plasma-cleaning chamber for 60 s at a chamber pressure of ~100 mTorr.

The pristine and plasma etched FLG were coated with a 5 wt.% solution of polymethyl methacrylate dissolved in propyl acetate to improve the structural integrity of the foams, and also improve the cell performance by creating a hydrophobic layer on the cathode surface.[85,86] The Ni foam that served as the sacrificial substrate was then etched

away by submerging the samples in 5 M HCl for ~12 hours, after which they were rinsed with a 0.25 M KOH solution to remove the residual HCl. Finally, the samples were rinsed with DI water and dried thoroughly overnight in an oven (120 °C) along with the Al foil anodes and glass fiber separators.

The EMI·$AlCl_4$ ionic liquid electrolyte was prepared by combining $AlCl_3$ with EMICl in a 1.3:1 molar ratio. This ratio has been shown to yield nearly equal amounts of $AlCl_4^-$ and $Al_2Cl_7^-$ anions, which are needed for the initial intercalation into the FLG foam cathode and plating on the Al anode, respectively.[56] Prior to combining the components, EMICl was heated under vacuum at 140 °C for at least 48 hours to remove any residual moisture. This was done by placing the EMICl in a glass vial while still inside the glovebox. The vial was sealed with a plastic cap through the top of which a ¼″ diameter opening was made by melting the plastic with a heated steel rod. Through this hole, a ¼″ tube was passed and sealed with epoxy, allowing the vial to be connected to a vacuum pump. After drying, it was allowed to cool slowly by ramping down the temperature while still under vacuum, yielding a pale yellow crystalline solid. The ionic liquid components were mixed in an Ar filled glove box that contained less than 10 ppm oxygen and moisture. When combining the components, care must be taken to slowly add the fine $AlCl_3$ powder to the crystalized EMICl as the reaction is highly exothermic and the evolved heat can lead to degradation of the organic component. Typically, a small portion of the $AlCl_3$ was added to the EMICl while rotating the vial to keep the evolved liquid in motion. Having the EMICl in a crystallized form as opposed to a powder helps to slow the reaction and reduce heat as there is less surface area at which the reaction can take place. A schematic for the cell

construction is shown in Fig. 3.2a. All components were assembled into pouch cells using aluminized plastic as the container and Ni tabs (MTI Corp.) as current collectors. Each cell was loaded with ~0.5 ml of electrolyte prior to sealing. The cells do not require conditioning as in an LIB, but they should be cycled once or twice via cyclic voltammetry before testing. This is because an irreversible oxidation peak is present at ~ 1.1 V that only persists for the first one or two cycles and is likely related to reactions involving residual moisture in the ionic liquid.

The DFT calculations were performed using Quantum ESPRESSO. The approach included the van der Waals interaction in DFT-D2 formalism under a generalized gradient approximation (GGA) of the exchange correlation functional. The cell size for each graphene layer was chosen to be 4x4 unit cells. The ultrasoft pseudopotential (Rappe Rabe Kaxiras Joannopoulos) was used for all species with GGA. The energy cutoff for the wave function and the charge were set to 35 Ry and 350 Ry, respectively. The structure containing intercalated $AlCl_4^-$ within two graphene layers was fully relaxed until all force components were smaller than 10^{-3} Ry/Bohr, in order to obtain the exact position and orientation for the molecule. The region between the graphene layers was sliced into 1000 planes parallel to graphene and the charge transfer profile was determined by computing the charge averaged over each plane.

Electrochemical characterization of the cells was carried out using a Gamry Reference 3000, Keithley 2400 source meter and a Solartron 1470 battery test unit. The Raman spectra were collected using a Renishaw InVia micro-Raman spectrometer (50x objective) with a 532 nm diode laser (Crystalaser). In situ Raman measurements were

accomplished by assembling a cell on a glass microscope slide and sealing the edges with epoxy as shown in Fig. 3.2.

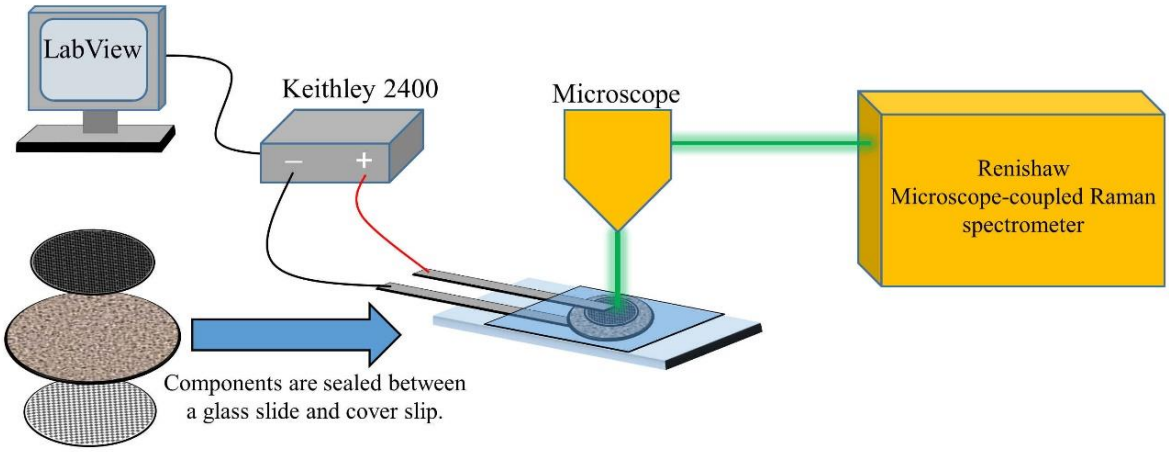

Figure 3.2: Diagram showing the method used for in-situ Raman spectroscopy. Cell components were assembled between a glass slide and cover slip that were then sealed with epoxy.

3.1.3 RESULTS AND DISCUSSION

Figure 3.3a shows a schematic of the cells which were used for all trials. Representative CV curves for AIBs with pristine and plasma treated cathodes are displayed in Fig. 3.3b. The FLG foam cathodes used are either pristine or were exposed to varying intensities of Ar plasma for 60 seconds as indicated in the figure legend. The plasma treatment serves to induce pores and defects in the surface of the FLG, which could possibly alter the intercalation behavior as reflected by a change in voltage or capacity. Three peaks located at ~1.9, 2.1, and 2.38 V are observed in the CV plots while charging.

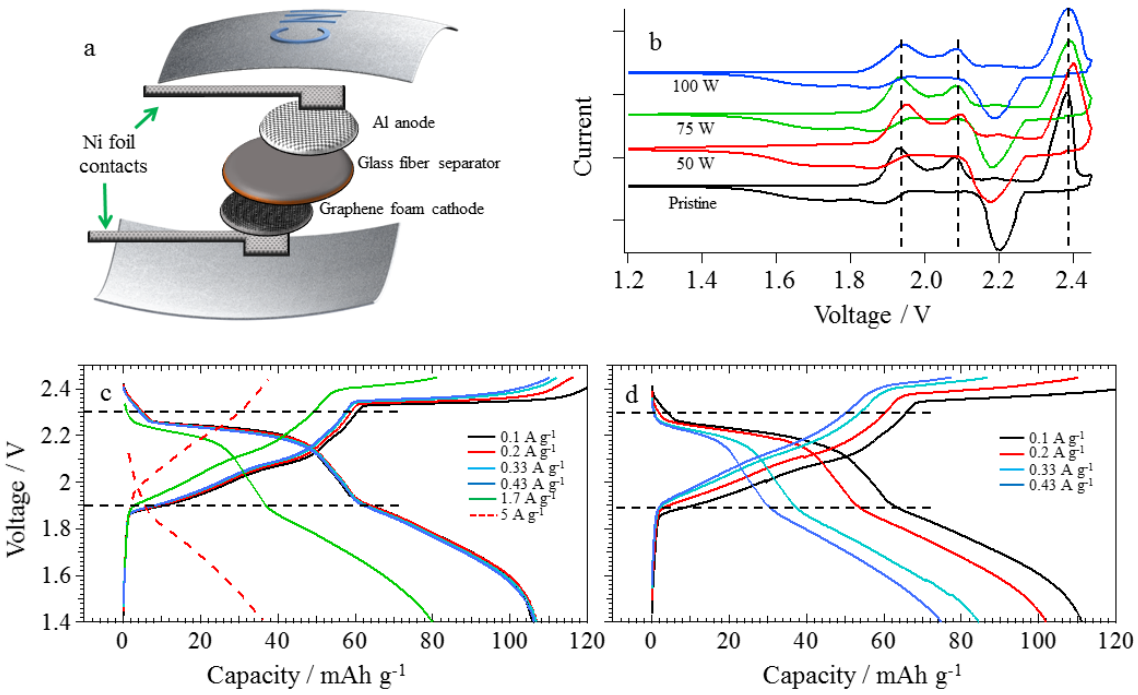

Figure 3.3: a) A schematic showing the components of an Al-ion battery (AIB). The upper and lower sheets are aluminized plastic. b) Cyclic voltammograms of AIBs with pristine and plasma treated FLG foam cathodes. The dashed lines correspond to redox processes in the AIB. c) and d) Charge/discharge characteristics for AIBs with a pristine and a 100 W plasma treated cathode, respectively. The dashed lines correspond to the peaks shown in panel b.

These voltage values correspond to the onset of the charging plateaus displayed in Figures 3.3c and 3.3d. The corresponding discharge valleys are located at 2.2 V for the charging peak at 2.38 V while a broad valley appears at 1.9 V encompassing the 1.9 and 2.1 V charging peaks. The dashed lines in the plots serve as reference points to illustrate that there is no significant difference in peak voltage or voltage plateaus between different

cathodes. It should be noted that for plasma treated cathodes, the capacity was observed to decrease at a faster rate with increasing discharge current densities than was seen for their pristine counterparts. Previous work done on Li intercalation into graphite showed similar peaks in the CV curves, and it was found through x-ray diffraction (XRD) measurements that they correspond to the onset of staging as the graphite transitions from a high-stage or dilute stage-one GIC to a stage-one GIC.[87–89] As evinced by the Raman spectra, I deduce that the three redox peaks in the CV for the FLG foam cathode in AIB correspond to staging of the $AlCl_4^-$ anions ultimately leading to a stage-one intercalated FLG.

Raman spectroscopy has been widely used for monitoring charge transfer processes in both donor and acceptor GICs.[90–96] The in-plane vibrations of C atoms with E_{2g2} symmetry in graphite appear as the so-called graphitic or *G*-band at ~1585 cm^{-1} in the Raman spectrum. The *G*-band is highly sensitive to both charge transfer and changes in interlayer interactions during intercalation/de-intercalation. For acceptor GICs, the formation of a dilute stage-one GIC where each layer is sparsely occupied by intercalant is associated with a steady upshift in the *G*-band frequency from its initial position of ~1585 cm^{-1}. Sudden changes in the graphene layer stacking caused by staging and the associated stresses result in a discrete split of the *G*-band. The interior unperturbed graphene layers will continue to exhibit a ~1585 cm^{-1} (E_{2g2i}) mode while the bounding layers adjacent to the intercalant ions display a peak at an upshifted discrete frequency (E_{2g2b}). The degree of the shift is dependent upon the stage of intercalation.

Figures 3.4a and 3.4b show the in situ Raman spectra obtained for an FLG foam cathode during a typical charge (a) and discharge (b) cycle. While charging, no shift in the

G-band frequency is observed below 1.8 V. A slight upshift is evident as the voltage increases to 1.9 V (corresponding to the first redox peak in Fig. 3.3b) at which point the *G*-band splits into two Raman modes for the reasons explained above, the second peak appearing at 1603 cm^{-1} being the E_{2g2b} mode. The upshift in peaks observed during charging is due to charge extraction from graphene layers in the FLG foam by the intercalated $AlCl_4^-$ ions, indicating an acceptor GIC type behavior.[97] The splitting of the *G*-band located at ~1585 cm^{-1} at 1.9 V is due to the onset of ordered staging where intercalant layers influence the frequency of the E_{2g2i} mode, leading to a discrete upshift by 18 cm^{-1} to 1603 cm^{-1} (E_{2g2b} mode). As charging continues past 1.9 V, the GIC transitions to lower stages (i.e., more intercalation leading to more bounding layers) as seen by the diminishing intensity of the E_{2g2i} mode accompanied by a continual upshift in E_{2g2b} mode frequency, which was initially located at ~1603 cm^{-1}. The E_{2g2i} mode disappears as the voltage reaches 2.1 V, which corresponds to the second redox peak observed in Fig. 3.3b, indicating that interior layers no longer exist and a stage-two GIC is formed.[98] Beyond this point during charging, the voltage rises rapidly, and the E_{2g2b} mode intensity begins to diminish with a concomitant increase in the intensity of a new Raman mode at ~1635 cm^{-1} (Figure 2a). The emergence of this new E_{2g2b} mode at ~1635 cm^{-1} marks a transition from a stage-two to a stage-one GIC, and its corresponding signature is the top most plateau in the charging curve occurring at ~2.3 V (Fig. 3.3c) and the largest peak in the CV profile (Fig. 3.3b).

The total shift of the E_{2g2} mode during charging was found to be ~49 cm^{-1} for AIBs comprised of pristine FLG foam cathodes with the maximum frequency being 1634 cm^{-1}.

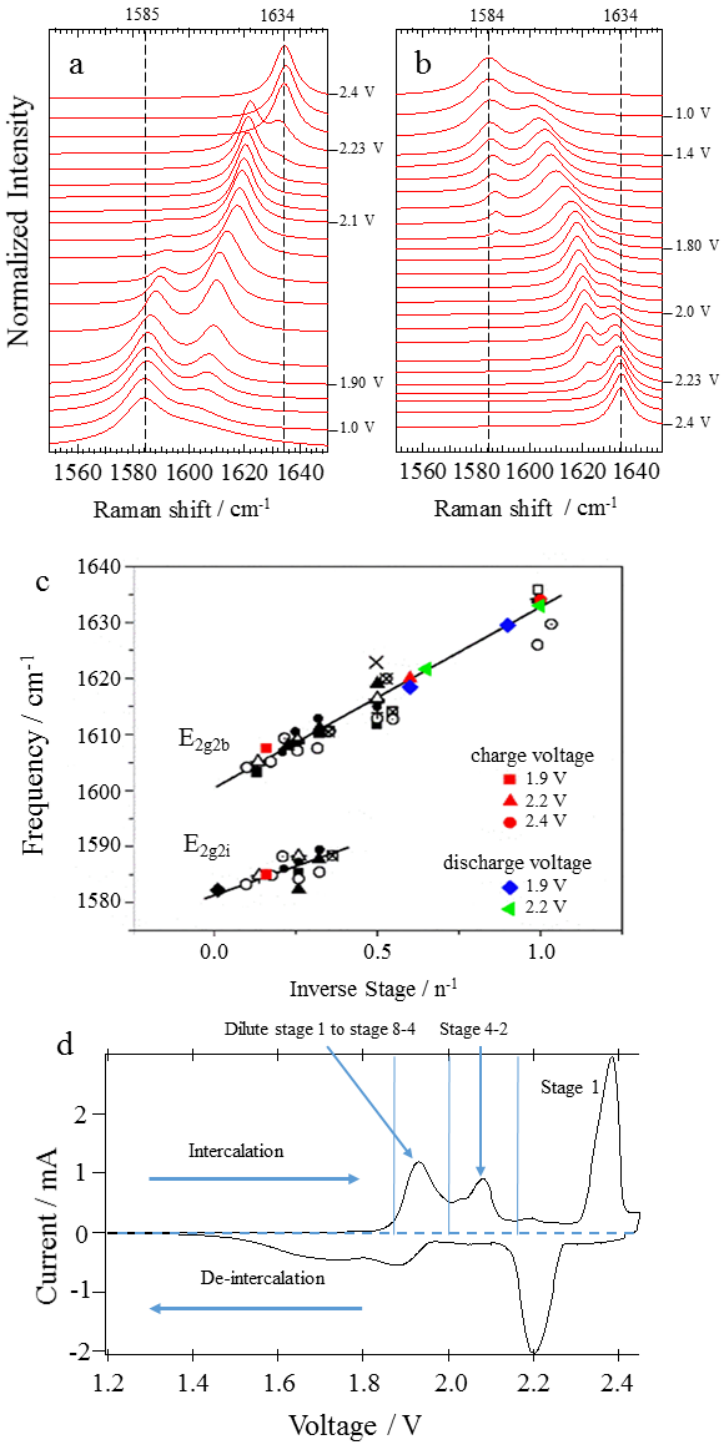

Figure 3.4: a) and b) Raman spectra of the FLG cathode during the charge (a) and discharge (b) process. c) A further confirmation of a stage-one GIC is evident when the peak positions (from panels a and b) are overlaid on the universal plot for *G*-band shifts as a function of reciprocal stage index for acceptor type GICs (taken from ref. [99]). d) The voltages at which peak current values are obtained track well with the onset of the *G*-band splitting events, as well as the charge/discharge plateaus shown in Fig. 3.3.

This trend in the upshift and splitting of the E_{2g2} mode is in excellent agreement with the trends exhibited by other acceptor GICs (Fig. 3.4c), which was originally compiled by

Dresselhaus and Dresselhaus.[99] The overlaid data in Fig. 3.4c confirmed that the fully charged FLG foam cathodes were indeed stage-one GICs. Fig. 3.4d correlates the staging (as determined through Raman spectroscopy) with the CV response for an AIB comprised of pristine FLG foam cathodes. Notably, both Raman and CV data strongly indicate that the charge-discharge processes are highly reversible, and that the EMI·$AlCl_4$ system is capable of reversible stage-one intercalation with the FLG cathode yielding good cell performance. Similar shifts in the Raman spectra were observed during the discharging process (Fig. 3.4b). The in situ Raman spectra for an AIB comprised of a 100 W plasma treated FLG foam cathode exhibits similar characteristics to those of the pristine examples depicted in Figs. 3.4a and 3.4b, and the Raman shifts also fall on the universal acceptor plot to coincide with a stage-one GIC. No differences in the magnitude of peak shifts are seen between pristine and plasma treated samples indicating that surface defects do not significantly affect the intercalation process. However, as discussed below, the energy and power densities of the 100 W plasma treated FLG cathode is poor compared to the pristine FLG.

The acceptor nature of the $AlCl_4^-$ ion is further demonstrated by DFT modelling as shown in Fig. 3.5. The $AlCl_4^-$ ion is positioned between two layers of Bernal stacked graphene, each containing 32 carbon atoms. Upon relaxation of the system, charge is transferred from the graphene sheets to the chlorine atoms of the $AlCl_4^-$ molecule. As shown in Fig. 3.5b, the charge is uniformly depleted from carbon atoms present within the geometrical shadow of $AlCl_4^-$ ion. We also observe that the tetrahedal structure of $AlCl_4^-$ is slightly deformed upon intercalation (Fig. 3.5c). The amount of transferred negative

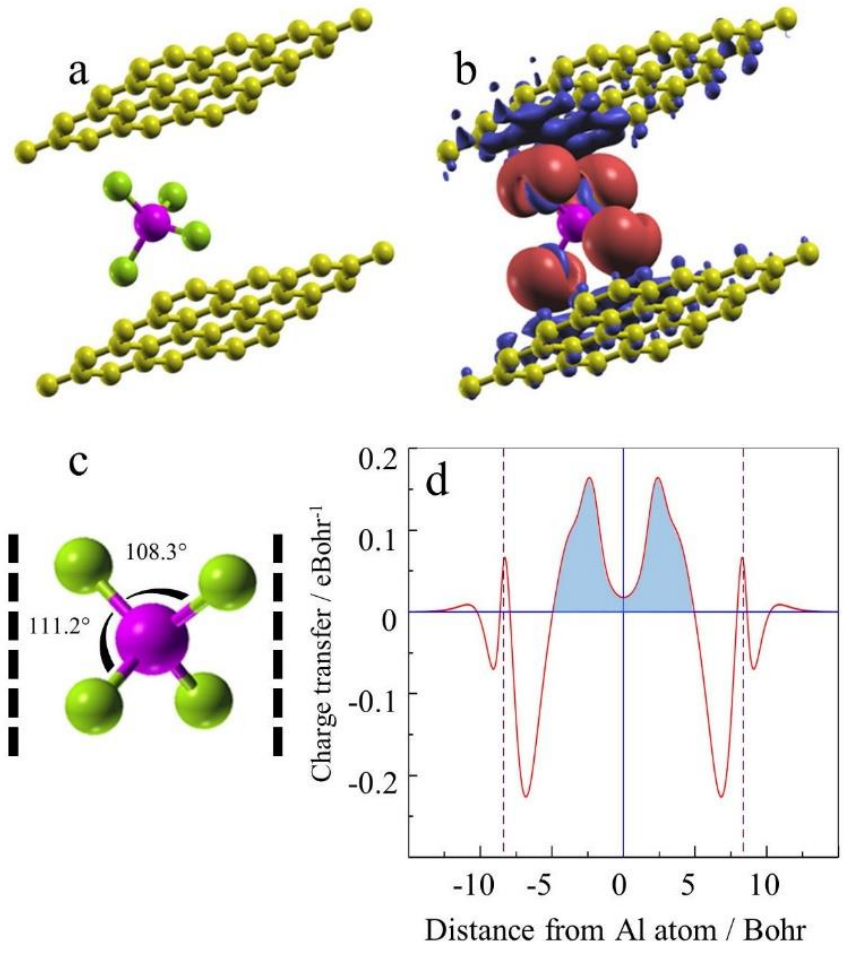

Figure 3.5: DFT model of charge transfer between graphene layers and $AlCl_4^-$ intercalant ion. a) and b) show the system before and after relaxation respectively. Negative charge is transferred from the blue regions to the red. c) Bond angles of the distorted $AlCl_4^-$ ion oriented between two graphene planes (dashed lines). The unperturbed bond angles in $AlCl_4^-$ are 109.5°. d) Charge transfer distribution as a function of distance from the central Al atom, the dashed lines marking the position of the graphene planes. The shaded area was integrated to obtain the net charge transfer.

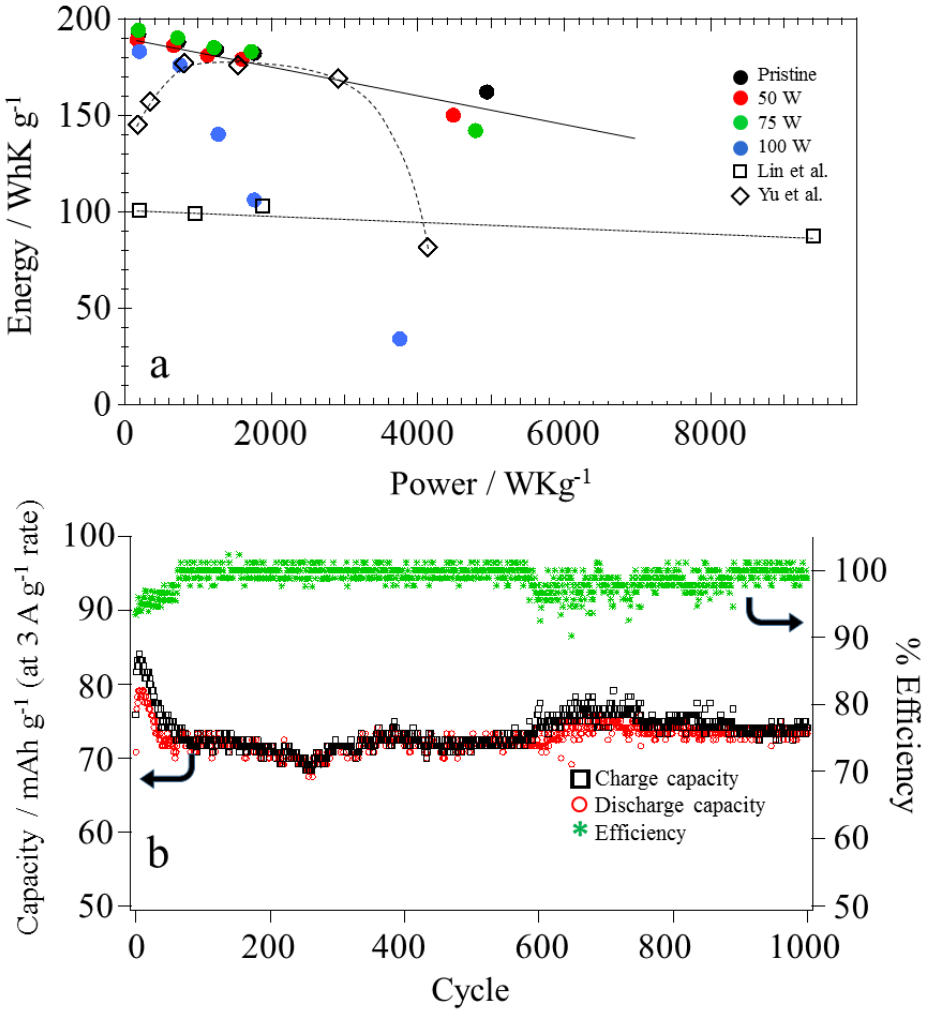

Figure 3.6: a) Ragone plot for AIBs made using pristine and plasma treated FLG foam cathodes. The legend shows the power of the plasma to which the FLG was exposed. The poor performance for the cell which uses the 100 W cathode is due to structural damage caused by the high plasma power. Data for AIBs reported by Lin et al.[62], and Yu et al. [78] are also included in the Ragone plot for comparison. b) Charge/discharge cycling of a pristine AIB subjected to 1000 cycles at a rate of 3 A g^{-1} with a potential limit of 2.4 V.

charge is determined by integrating the area between the zero-energy intercept points of the charge transfer curve (~ -5 to 5 Bohr) indicated by the shaded area in Fig. 3.5d, yielding 0.8 *e* per intercalant ion.

Figure 3.6a is a Ragone plot which summarizes the performance of AIBs with FLG cathodes. The specific energy values for the AIBs were determined by integrating the areas under the plateaus shown in the voltage vs. capacity plots in Figs. 3.2c and 3.2d, and the specific power was calculated by dividing the specific energy with the discharge time. The Ragone plot also displays the performance of AIBs demonstrated by other researchers in the recent literature.[62,78] The power and energy densities of their AIBs were determined by integrating the capacity curves provided in their data. My AIBs with pristine FLG show a marked increase in power and energy density over those previously published.

I attribute this increased performance to the robustness of the FLG cathodes, which allow intercalation to a fully stage-one GIC unlike studies reported by other groups. For example, in the study by Yu et al., their CV data did not display the three distinct redox peaks during charging (cf. Fig. 1b), and their galvanostatic discharge plots only showed a very weak plateau at ~2.1 V, indicating that a stage-one GIC was not achievable under their experimental conditions, which adversely affected the cell performance. In the work by Lin et al., they used XRD measurements of a charged cathode and determined it to be a stage-four GIC when charged. This was corroborated by their in situ Raman data taken while the cell was charged to 2.42 V. The *G*-band of their cathode was located at ~1625 cm^{-1} while charged, indicating that a stage-one GIC was not realized under their experimental conditions either.

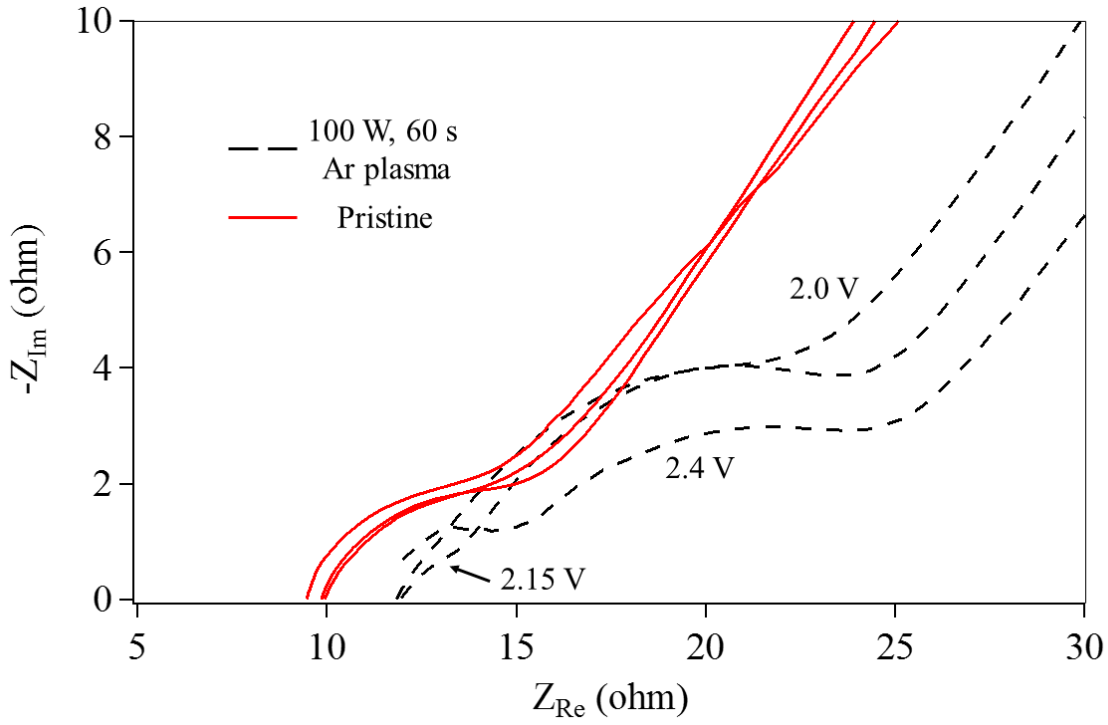

Figure 3.7: Electrochemical impedance spectra of pristine and 100 W plasma treated FLG measured at several voltage values. The voltages correspond to the peak current voltage values found in CV scans. The larger semicircles of the plasma treated FLG demonstrate greater charge transfer resistance compared to pristine FLG.

I also evaluated the stability of a pristine AIB, wherein the cathode reaches full stage-one intercalation, by using galvanostatic cycling at 3 A g^{-1} and a peak voltage of 2.4 V. As shown in Fig. 3.6b, the AIBs yielded a coulombic efficiency near 100% up to 1000 cycles with minimal loss of capacity. The initial increase in capacity has yet to be investigated but could be related to chemistry at the surface of the Al anode. The AIBs require no conditioning since no surface-electrolyte interface layer is formed using this ionic liquid electrolyte.

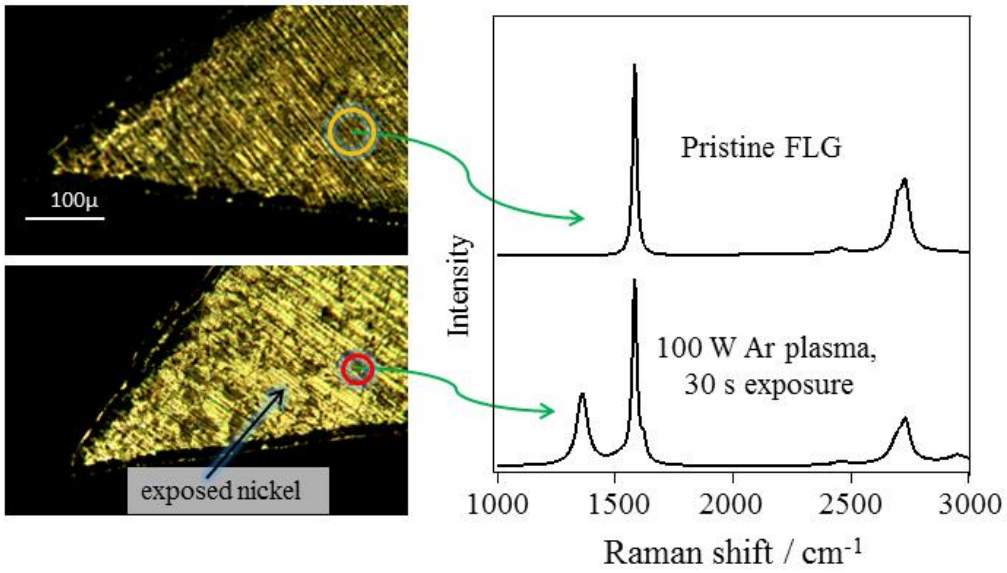

Figure 3.8: The top optical microscope image shows FLG on Ni foil next to its associated Raman spectrum. Notice that the Ni foil appears dark and the Raman *D*-band is absent signifying the high quality of the FLG. The bottom optical image shows the same area after being exposed to 100 W Ar plasma for 30 s revealing the relatively brighter surface of the Ni foil.

Though the spectroelectrochemical signature of the FLG foam cathode exposed to 100 W plasma is identical to the pristine cathode, its energy and power densities deteriorate rapidly. I attribute this deterioration of performance to the poor connectivity of graphene grains due to damage induced by plasma treatment. It is well known that defects in the graphene lattice increase sheet resistivity,[100–103] and the same can be inferred from Fig. 3.7 which displays Nyquist plots at several voltages for pristine FLG and FLG treated with 100 W plasma. The high-frequency semicircles of the plasma treated FLG are larger than those exhibited by their pristine counterparts, indicating greater charge-transfer resistance

in the former. Furthermore, the semicircles also change as the voltage is increased for the plasma treated FLG, with the clear formation of a second semicircle at higher frequencies for higher voltage values, a trend that was absent for pristine FLG. Indeed, I found that treating the cathodes at the maximum power of 100 W for longer periods of time resulted in the ablation of all carbon from the Ni foam substrate, prompting further study to investigate the structure of the FLG foam when exposed to plasma. FLG grown on Ni foil was used in this experiment because the smooth foil surface allows much easier observation of the FLG before and after plasma treatment. In Fig. 3.8, the top image shows FLG grown on Ni foil while the bottom image is the same FLG following 30 s exposure to 100 W Ar plasma. The brighter areas of the substrate correspond to exposed Ni while the darker areas are FLG, demonstrating the ablation of carbon material when the FLG is exposed to the high power plasma. Their corresponding Raman spectra are shown to the right where the *D*-band (~1350 cm^{-1}) is very prominent for the plasma treated sample. The *G′*-band located at 2700 cm^{-1} indicates the presence of multiple layers, concurring with the AFM images displayed in Fig. 3.9 showing the FLG to be ~5 nm thick. The graphene flakes analyzed via AFM were created by sonicating a piece of graphene foam and spin coating the resulting suspension onto a silicon substrate. Measurements of multiple flakes give a consistent thickness of ~5nm. Considering that profile measurements of a single graphene layer vary due to surface-graphene and graphene-tip interactions, it is customary to subtract ~0.5 nm from an FLG measurement to account for this systematic error.[104] This correction combined with the fact that the interplanar spacing of Bernal stacked graphene is 0.335 nm shows the samples to be composed of ~13 graphene layers. The ablation of

FLG due to excessive plasma treatment, as shown in Fig. 3.8, would deteriorate structural integrity and electrical connectivity within the FLG foam cathode, ultimately resulting in a loss of capacity.

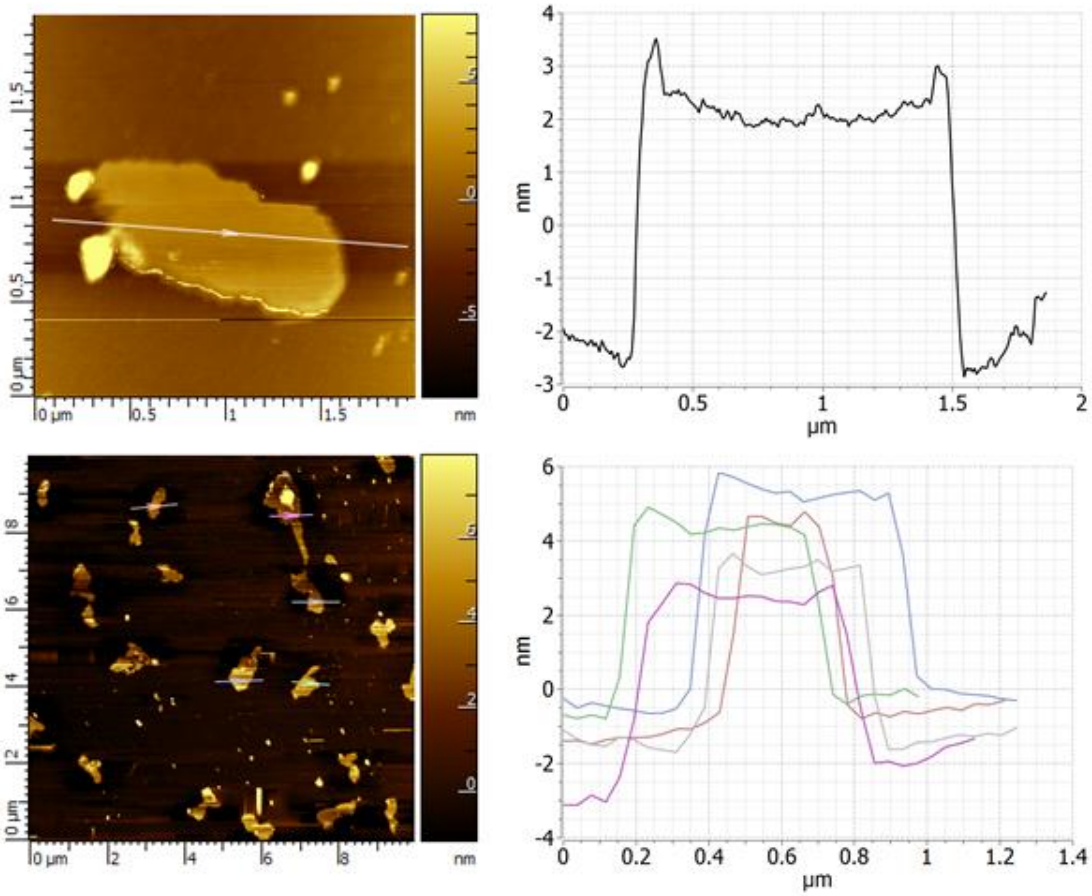

Figure 3.9: AFM measurements of graphene flakes. As an example, the top left panel shows a line scan over one of the flakes and its corresponding height profile is shown in the top right panel. The bottom panels show the same measurements for several flakes.

3.2 NITROGEN DOPED FLG

3.2.1 INTRODUCTION

In section 3.1, I examined the role of defects induced by exposing the FLG cathode to argon plasma. The edge defects and vacancies created by the argon plasma are known to induce *p*-doping in graphene, and they were found to not adversely affect the performance of the AIB. In previous work, our group has conducted similar experiments for FLG electrodes in EDLCs and have also found that nitrogen doped FLG (N-FLG) electrodes yielded an increase in capacitance via increasing the amount of edge defects and altering the density of states within the graphene.[77] In this section, I extend the investigation to *n*-type defects in AIBs by comparing the performance of AIBs prepared with N-FLG cathodes.

The doping of graphitic electrodes with nitrogen has been found to be an effective method for improving the performance of certain cell chemistries. N-FLG was found to improve the capacity and rate capability of K-ion cells when used as an anode by providing reactive sites that are amenable to charge transfer.[80] N-doped carbon nanofibers derived from polypyrrole were found to improve the function of sodium ion batteries by having a larger spacing between carbon layers and increasing sodium ion adsorption.[105] Polyprryole-functionalized graphene sheets have also been used to improve Na-ion batteries in the same manner.[106] Li-ion cells have benefitted from N-doped graphitic electrodes: One to two-layer N-doped graphene showed almost double the capacity of pristine analogs due to increased surface defects,[107] Silicon nanowires coated with N-

doped graphene improved lithium adsorption through the presence of dangling bonds,[108] and N-doped graphite oxide sheets allow greater Li-ion capacity.[109] In all of the above examples [95-99], the intercalating species are monatomic cations which can benefit from the increased electronegativity provided by the nitrogen. In the case of the AIB chemistry where $AlCl_4^-$ anions are the intercalating species, I have found N-dopants to be detrimental to intercalation and cell performance, except in the case that N-dopants are created by nitrogen plasma exposure.

Nitrogen dopants are known to adopt three main configurations within the graphene lattice; graphitic, pyridinic, and pyrrolic. These configurations are illustrated in Fig. 3.10a. In the graphitic configuration, carbon atoms are substituted with nitrogen without disrupting the lattice, while for the pyridinic and pyrrolic configurations, vacancies in the lattice are necessary. Each configuration alters the local electronic density of states around the nitrogen site in the graphene lattice.[77,110] The pyrrolic configuration is known to have the greatest local electronic density of states while being the most reactive due to the pentagonal distortion of the graphene lattice. The configuration also determines whether the graphene will display *n* or *p*-doping characteristics. Nitrogen in the graphitic configuration results in *n*-doping of the lattice while pyridinic results in *p*-doping due to the dangling bonds of the carbon vacancies.[111,112] However, hydrogenated pyridinic sites cause *n*-doping. Experimental results for pyrrolic defects have found that they cause *n*-doping, contrary to predictions from DFT.[111,113,114] In my work, the etching process wherein the FLG is exposed to concentrated HCl would likely yield hydrogenated nitrogen defect sites, resulting in *n*-type doping of the graphene. In previous work, our group found

that altering the chemicals introduced during the FLG growth would result in different ratios of the nitrogen configurations.[115] In this section, I use this growth method along with post growth treatment of FLG to create samples with varying amounts and configurations of nitrogen dopants. The N-FLG samples were then evaluated as cathode materials for AIBs.

3.2.2 RESULTS AND DISCUSSION

A detailed synthesis of the FLG cathode can be found in section 3.1.2. Briefly, four different N-FLG samples were prepared; two via in-situ doping during CVD growth and two via post-growth treatment. For the samples prepared via CVD, Ar gas was bubbled at 50 sccm for the entire 60 minute growth period through acetonitrile (#1) or a 1:3 volume mixture of acetonitrile:benzylamine (ACN:$BzNH_3$) (#2). For post-growth processing, pristine FLG samples were first exposed to 2 minutes of 100 W N_2 plasma (#3, #4), then #4 was annealed in acetonitrile vapors at 600°C for one hour. Their respective Raman spectra are shown in Fig. 3.10b, which have been normalized to the prominent *G*-band found at ~1585 cm^{-1} for a meaningful comparison. The magnitude of the *D*-band present at ~1350 cm^{-1} correlates with the amount of defects present in the graphene lattice.[116] As evident in Fig. 3.10b, sample #4 exhibited the smallest *D*-band intensity, which is attributed to the fact that this sample was annealed in ACN vapors at 600°C causing a reduction in defects.

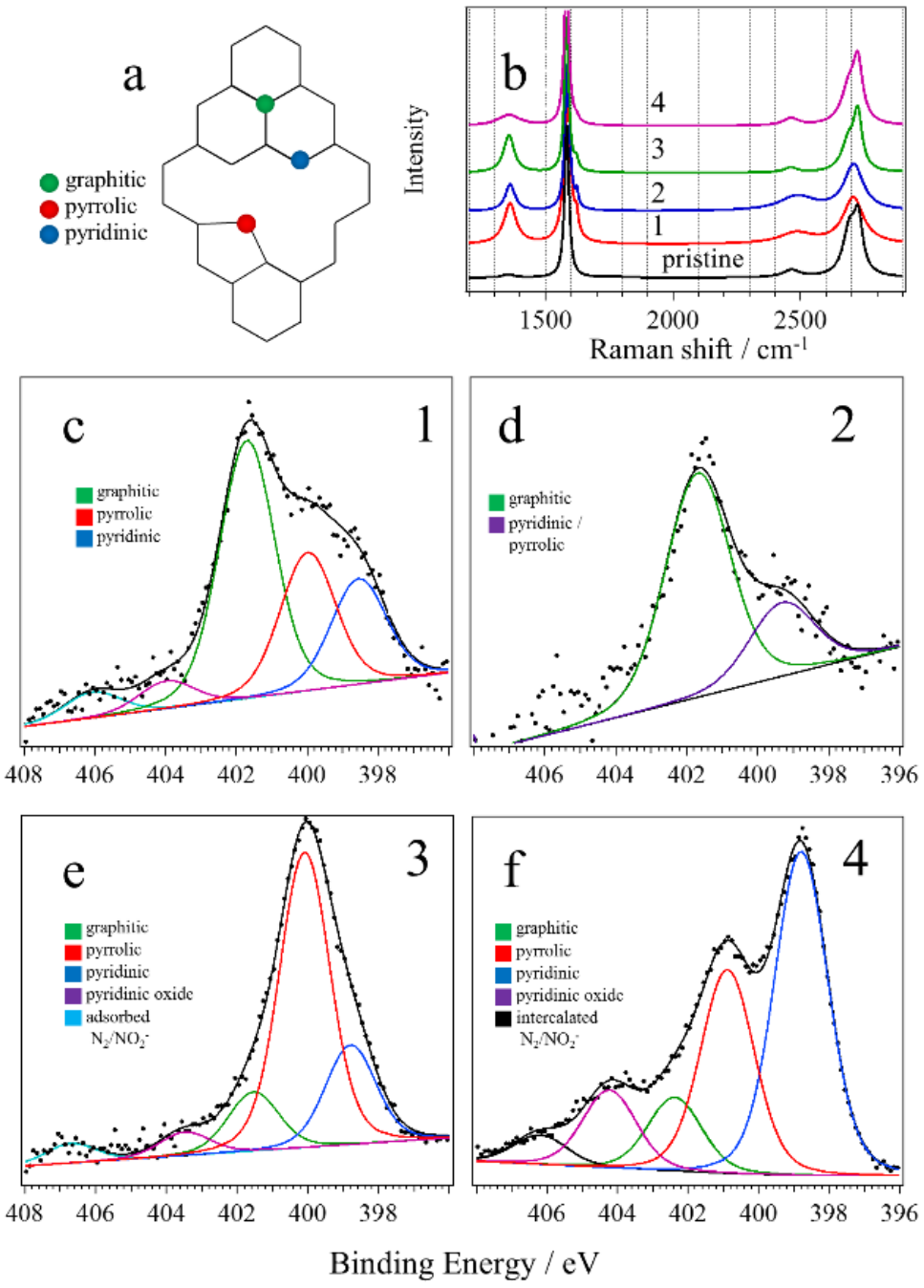

Figure 3.10: a) Different configurations of nitrogen dopants in the graphene lattice. b) Raman spectra of N-FLG samples. c-f) XPS spectra of N-FLG samples.

The XPS data showing N1s peaks for each sample can be seen in Figs. 3.10c-f, where c-f correspond to samples #1-#4 respectively. The spectra were recorded on a Kratos Axis Supra XPS using a survey pass energy of 160 eV. For samples #1 and #2, the nitrogen content is 0.30% and 0.13% respectively, where the N-dopants mainly appear in the graphitic configuration. For sample #3, the N_2 plasma treatment yielded a nitrogen content of 0.57%, mostly in the pyrrolic configuration. The predominance of pyrrolic defects following plasma exposure has also been observed by other researchers.[117] The annealing process following the N_2 plasma treatment increases the nitrogen content to 1.74% for sample #4. The relative peak sizes demonstrate that the annealing also created a predominance of pyridinic type defects, possibly from the conversion of pyyrolic ones. Oxygen was also found to be present in all samples. Previous studies have shown that edge defects in the graphene lattice are highly active and will form oxygen containing groups when exposed to air.[118,119]

The electrochemical properties of the samples were analyzed by assembling cells and coupling cyclic voltammetry with in-situ Raman spectroscopy. The Raman spectra of pristine and N-FLG during the charging process can be seen in Fig. 3.11a. The left and center spectra are taken from a pristine FLG cathode and FLG exposed to only N_2 plasma (sample #3) respectively, while the right spectra are typical for samples #1 and #2. Sample #4 showed poor charging characteristics likely due to a lack of intercalation, thus its spectra are not included in Fig. 3.11. The lowest curve in the series of spectra is taken prior to charging. In this initial state, as expected, the *G*-band is found at ~1584 cm^{-1}. As charging

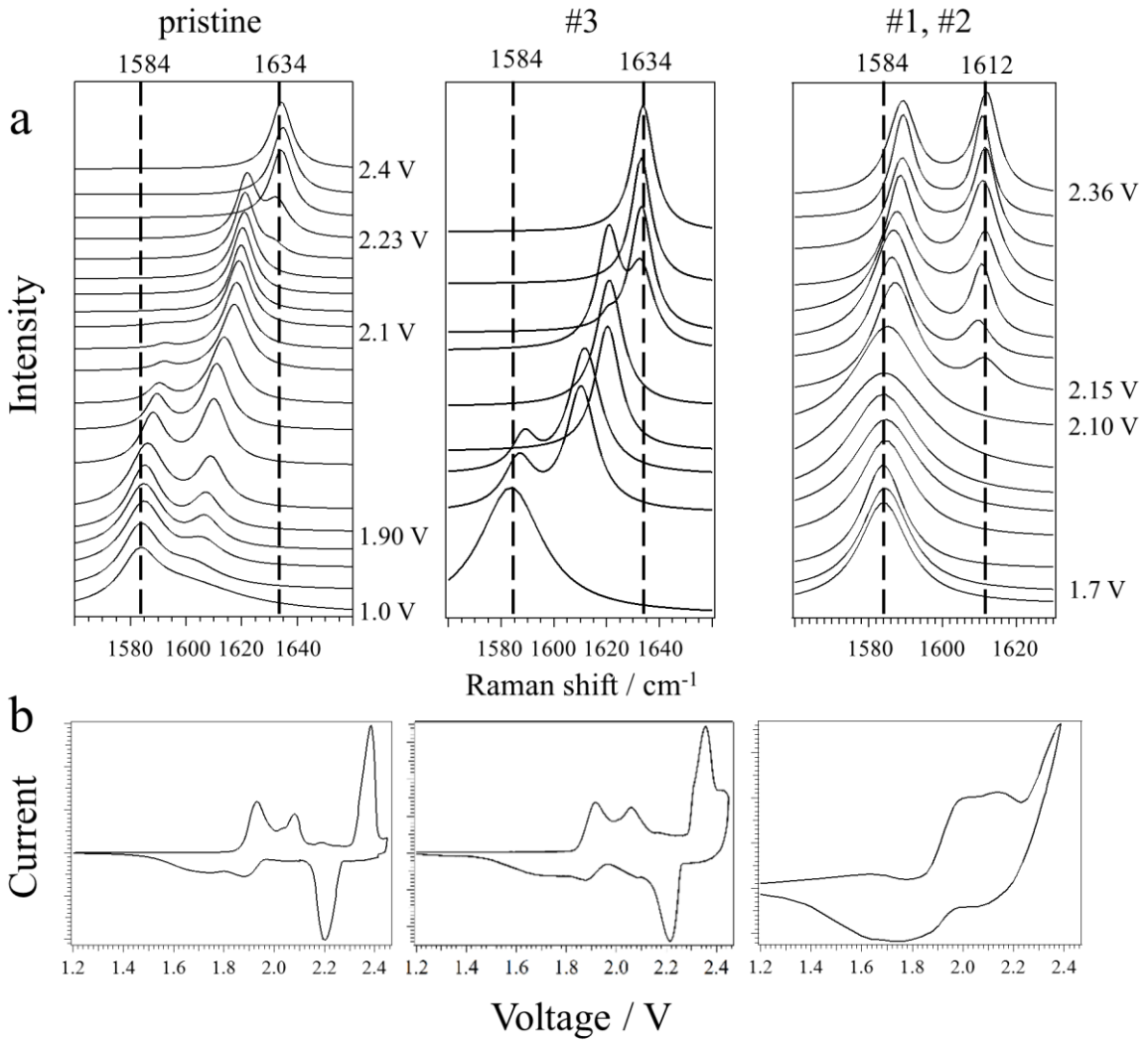

Figure 3.11: a) in situ Raman spectra taken during the charging of pristine and N-FLG cathodes. b) Corresponding cyclic voltammograms of the Raman spectra.

begins and intercalation commences at ~1.9 V for the pristine FLG and #3 and ~2.10 V for #1/#2. As the voltage further increases, The *G*-band splits due to staging of the FLG. For the pristine FLG and #3 there is an additional splitting at higher voltage as the FLG transitions to a stage-one intercalation compound.[120] The staging process should also result in a complete suppression of the original 1584 cm^{-1} peak, which is still present in the

spectra of #1/#2. The split for these samples occurs at ~2.1 V, significantly higher compared to that of un-doped FLG. The E_{2g2i} mode originating at 1584 cm^{-1} is seen to remain throughout the charging process, showing the N-doped FLG cathode is only in a mixed phase of staging and fails to achieve even stage-two intercalation. These results indicate that the N-FLG prepared via in-situ doping does not charge properly due to poor intercalation, preventing the FLG from forming a fully charged intercalation compound. This can also be seen from the cyclic voltammograms in Fig. 3.11b that correspond with the Raman spectra. For samples #1/#2, the current peaks associated with intercalation are very broad to the point where the two neighboring peaks are almost indistinguishable. In the process of cyclic voltammetry, the applied voltage will force the charge-transfer process. In this case, the initial intercalation occurs relatively slowly as seen by the broad peaks. This can be compared to the profile of the pristine FLG and sample #3 that show three easily distinguishable peaks, the third peak being at the highest voltage and associated with a transition to a stage-one intercalation compound. Charging of samples #1, #2, and #4 also resulted in the evolution of chlorine gas, which was not the case with sample #3. The gas evolution was inferred from the expansion of the pouch cells during cycling. The chlorine gas would evolve from the oxidation of the $AlCl_4^-$ ions at the higher end of the voltage range as known from the cell chemistry, and which is consistent with the catalytic properties of N-doped graphene.[121–124]

Modeling of the charge transfer between the graphene planes and $AlCl_4^-$ ions have been carried out via density functional theory (DFT), using Quantum ESPRESSO software. The parameters used in the calculations can be found in section 3.1.2. Modeling was carried out

for pristine FLG as well as the graphitic and pyridinic configurations. The pyrrolic configuration did not converge during modelling, so its parameters could not be determined in this analysis. Figures 3.12a and 3.12b show models for charge transfer between the graphene planes and intercalated ions for the pristine and pyridinic configurations. The red color indicates charge extraction from the graphene planes by the ion, the magnitude of which was found by integration of the curve in Fig. 3.12c. The charge transferred is 0.8 electrons per intercalant ion and is similar even with the presence of nitrogen dopants. For modelling the various N-dopant configurations, the $AlCl_4^-$ ion and the adjacent graphene planes were first allowed to relax individually before they were brought together as the intercalated system and allowed to relax. The difference in energy values between the individual and coupled systems was then taken as the formation energy where a positive energy value indicates a more favorable configuration.

From this method, the pristine FLG/ion system is shown to be somewhat more favorable than the pyridinic analog with energies of 0.998 eV and 0.896 eV respectively. However, the graphitic configuration was much more favorable than either at 2.226 eV. This result contrasts with the experimental results showing a lack of intercalation and breakdown of electrolyte for samples #1 and #2 whose defects are predominantly in the graphitic configuration as seen in the XPS data. This result indicates that even though intercalated $AlCl_4^-$ ions are relatively stable at graphitic N-dopant sites, the reactivity of the system and the presence of other types of dopants is enough to prevent proper intercalation. It also raises doubts as to the importance of the nitrogen in that the observed

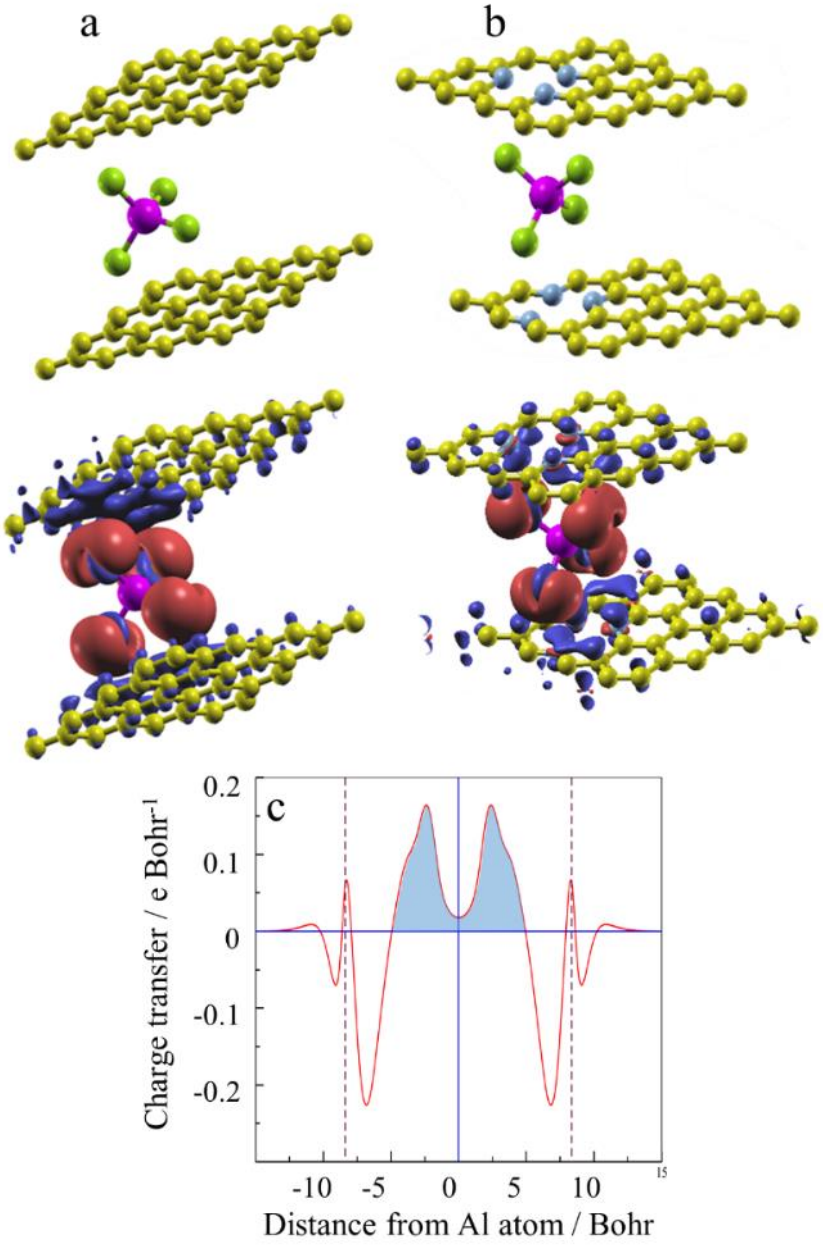

Figure 3.12: a and b) Models of a pristine and N-doped graphene lattice showing charge transfer to an AlCl4- ion. c) Charge transfer as a function of distance between the graphene plane and the ion. The magnitude of charge transfer was similar for pristine and N-doped samples.

behavior could be due to oxygen groups present at the edge defects of the FLG. To investigate this aspect, nitrogen-free samples were prepared that exhibit defects throughout the FLG by including a small amount of acetylene during growth. The presence of defects was confirmed via Raman spectroscopy. Cathodes made using this FLG were able to reach stage-one intercalation as determined by their CV data. The two peaks at the lower range of the voltage were found to overlap somewhat, likely due to the presence of internal defects in the FLG which would allow for different stages of intercalation to occur simultaneously. This result shows the importance of N-dopants in the studied system. However, not all N-doped samples performed the same. In the case of sample #3 which was only exposed to N_2 plasma without further treatment, no detrimental effects were observed as they were for the other N-doped samples. This would follow since the plasma treatment only effects the outer layers of the FLG as shown in section 3.1. If only the surface layers are affected by the plasma, the interior planes would be free of N-dopants so that intercalation can proceed during charging. A common method to force molecules between the layers of a graphitic material is to expose the material to vapors at elevated temperatures. For example, $AlCl_3$ can be intercalated to form a stage-one compound using this method at less than 300°C.[125] It follows that upon annealing in acetonitrile vapors at 600°C, internal formation of N-dopants would occur as the FLG is infiltrated by the vapors. These internal dopants would then cause the very poor performance found for sample #4 and subsequent Cl_2 evolution.

3.3. CONCLUSIONS

To conclude**,** I demonstrated AIBs comprised of FLG foam cathodes whose cell performance exceeded similar systems reported in the literature by achieving stage-one intercalation within the nominal voltage window, thereby fully utilizing the gallery space between graphene layers. Specifically, the excellent correlation observed between the CV plots and in situ Raman spectroscopy during charge/discharge cycles strongly implies that the superior cell performance demonstrated in this study stems from the reversible intercalation/de-intercalation processes supported by the FLG foam cathodes. Notably, I demonstrated AIBs with high energy and power densities (~200 Wh kg^{-1} at 200 W kg^{-1} and ~160 Wh kg^{-1} at 5000 W kg^{-1}) that exhibit a slow decrease in energy at higher power densities. From the CV plots in Fig. 3.3b, it is seen that the peak current potentials do not deviate significantly between cells comprised of pristine or plasma treated FLG foams at different plasma powers, confirming that the presence of in-plane surface defects in FLG cathodes does not alter the staging process. Likewise, in terms of energy and power densities (Fig. 3.6), the FLG foams treated at 50 and 75 W exhibited similar performances as the pristine FLG foam, while FLG foams treated at 100 W showed a comparatively poor performance. Three key insights into AIB batteries have been provided: i) it is necessary to reach stage-one FLG to achieve high energy and power density, which was confirmed using CV curves, DFT calculations, and Raman spectroscopy, ii) the AIB performance and the ion intercalation are insensitive to in-plane surface defects as long as the structural integrity and electrical connectivity of the FLG cathode are retained, and iii) chemical defects such as N-dopants preclude stage-one intercalation and lead to poor performance.

CHAPTER 4: HELICAL CARBON NANOTUBES AS SUPERCAPACITOR ELECTRODES

4.1 INTRODUCTION

As mentioned in section 1.2, electric double layer capacitors (EDLCs), also known as supercapacitors, are energy storage devices capable of power densities far in excess of batteries currently on the market. Conventional EDLCs use highly porous activated carbon powder combined with conductive additives for the electrodes.[126,127] The capacitance of an EDLC is directly proportional to the surface area of the active material, making porosity an important aspect of performance. Carbon nanotubes (CNTs), with their attractive electrical properties and facile synthesis, have opened new avenues for improving EDLC performance and there has been much fruitful research devoted to incorporating CNTs into EDLCs. CNTs are a very versatile material that can be incorporated into electrodes via mixing with activated carbon slurry, free standing CNT films, or as aligned CNT arrays. Vertically aligned carbon nanotube arrays (VACNTs) with high areal density can be grown directly on current collectors, reducing contact resistance and the need for binders.[128–135] Electrodes made in this manner have been shown to possess gravimetric capacitance in excess of 100 F g^{-1}. Emphasis has also been placed on depositing or growing VACNTs in a continuous scalable fashion such that the current collectors can be wound directly into a useable product.[136–139]

One method of increasing the areal capacitance of an array of CNTs is to leverage the morphology of helically coiled carbon nanotubes (HCNTs). An HCNT is a MWNT that grows such that it takes on a helical shape. They can be grown in vertically aligned arrays

wherein adjacent HCNTs are aligned in pitch. Growing arrays of HCNTs directly on current collectors leads to a greater surface area per tube for a given array height compared to linear VACNTs, thus increasing the active surface area per unit area of the current collector. HCNT arrays have been found to possess mechanical properties superior to those of their linear counterparts. They are highly compressible and are able to mitigate impact stress which has led to interest in their use as impact absorption media for sensitive electronics and additives in epoxy based composites.[140–143] However, little research has been done on using HCNTs as an active material for EDLCs. Zeng et al. have used iron tartrate as a catalyst to grow helical carbon nanocoils which were then made into electrodes using a standard slurry recipe which yielded capacitance values of ~100 F g^{-1}.[144] In general, coils such as these are thicker in diameter compared to HCNTs and lack the regular graphitic lattice structure. Reddy et al. tested symmetric capacitors made from helical carbon nanocoils on Si substrates, yielding ~105 F g^{-1}.[145] Rakhi et al. integrated them with conductive polymers in a slurry applied to carbon cloth.[146] Beyond this, a comprehensive investigation into the potential advantages of HCNTs in EDLCs has not yet been undertaken. In this work, I evaluate the performance of HCNTs in the form of vertically aligned arrays and polymer-augmented buckypapers (BPs), and compare them with analogues made from linear CNTs. The areal capacitance values of similar structured electrodes are compared and HCNT susceptibility to plasma induced defects is confirmed. The lignin uptake of the two BPs and the resulting cell performances are also compared, with the HCNT BP showing superior polymer adsorption and capacitance.

Several theoretical explanations have been put forth to explain the growth mechanism of HCNTs.[147–149] During CNT growth via chemical vapor deposition, the use of other catalyst particles in conjunction with the iron catalyst alters the surface interactions between the metal catalyst particle and the hydrocarbon precursors that break down to form nanotubes. The mixed metal catalyst causes the carbon to be extruded at different rates at different sites on the catalyst surface, which produces stresses in the hexagonal lattice of the CNTs leading to the helical shape. One study used in situ XPS to confirm that the HCNTs originate from crystalline particles composed of Fe, In, Sn, and their carbides.[150] The same group also found that HCNTs tend to grow via the tip-growth mechanism. An HCNT is in a higher energy state relative to linear CNTs due to its inherent compressive and tensile stresses, and is therefore more susceptible to chemical modification of its surface. In the graphitic lattice of a CNT, defects in the honeycomb pattern, including pentagons and heptagons, result in local differences of charge density.[151–153] For this reason, HCNTs should be more susceptible to defects induced by exposure to Ar plasma, which can be measured as a change in the capacitance. This hypothesis encompasses the first part of this study wherein the performance of VANCT and HCNT arrays with and without plasma exposure are compared. The electrodes used here are arrays of HCNTs and VACNTs grown on conductive metal substrates. A brief overview of this aspect of the study is shown in the top row of Fig. 4.1. Though the plasma induced defects can be beneficial in some cases, exposure to Ar plasma could compromise the inherent electrical properties of CNTs due to lattice damage.

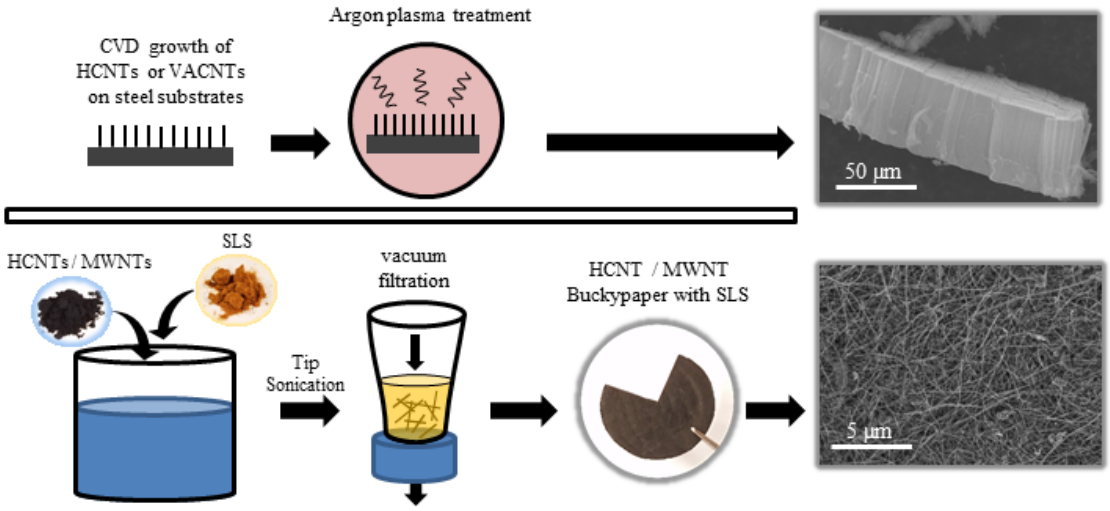

Figure 4.1: Fabrication procedure for the different electrodes used in this study. The top row shows steps used for fabricating the plasma-treated CNTs on steel substrates. The bottom row shows the steps involved in fabricating the BPs used in the second part of the study, where sodium lignosulfate (SLS) is the surfactant. For the arrays on steel, 1 M $TEABF_4$ in acetonitrile is used as the electrolyte whereas 1 M HNO_3 is used as the electrolyte for the BPs.

The second part of the study involves incorporating electroactive polymers into free standing CNT scaffolds known as buckypapers (BPs). BPs are formed from of a network of tightly packed, randomly oriented CNTs, and their structural properties are largely dependent on the quality of nanotubes used during their preparation.[154,155] Typically, they are prepared by dispersing the CNTs in water through the use of surfactants such as sodium dodecyl sulfate (SDS). They are then collected on filter paper via vacuum filtration after which they are dried and removed from the filter in the form of a BP. The fabrication

steps for the BPs are shown in the lower half of Fig. 4.1. They are chemically robust, flexible, conductive, and highly porous, making them ideal candidates as EDLC electrode media suitable for polymer integration. Though the surface area of MWNTs is relatively low, being typically less than 400 $m^2 g^{-1}$,[156–159] the macroporous spacing between the entangled tubes is good for polymer infiltration. It should be noted however that single and double walled CNT BPs possess significantly higher surface area.[155,160] Previously, structural polymers such as polyurethane,[161] polycarbonate,[162] epoxy resins,[154] and polyethyl ethyl ketone [163] have been incorporated into BPs with very high mass loading. However, when using electroactive polymers, the mass loading must necessarily be smaller to allow for electrolyte access within the structure. In the present work, BPs constructed from MWNTs and HCNTs are infiltrated with an electroactive polymer, sodium lignosulfate (SLS), and their performance is compared. The energy density is enhanced when the electroactive SLS polymer undergoes a reversible redox reaction, which increases the capacitance of an EDLC. Composite CNT-polymer composite electrodes can be prepared by including polymer in the CNT solution during the dispersion process or by direct polymerization on the surface of the BP.[146] With additional soaking in polymer solution, the polymer has the ability to further infiltrate the macroporous spaces between the CNTs, resulting in a greater mass loading than would be possible in the initial fabrication process of the CNT-polymer composite electrode.

Lignin is a naturally occurring polymer that is separated from cellulose and discarded during the production of paper products, making it a highly abundant and low-cost additive.[164] Past research has shown SLS to be amenable for use with BPs, possibly due

to the favorable π-π interaction between the aromatic quinone groups and the hexagonal carbon lattice. The quinone groups undergo a redox reaction in an acidic medium at ~0.5 V with respect to Ag/AgCl. Since the backbone of the lignin polymer is not highly conductive, the charge transfer is localized at the quinone site, which leads to sharper redox peaks than would be found for conductive electroactive polymers. The charges delocalize along the conjugated backbone of conductive polymers, resulting in broad redox peaks which manifest over a wide potential range.

4.2 MATERIALS AND METHODS

4.2.1 SYNTHESIS OF VERTICALLY ALIGNED CARBON NANOTUBE ARRAYS

CNTs are most commonly synthesized via chemical deposition. In order for CNT growth to occur, a catalyst and a source of carbon must be present. The preferred catalysts are usually metals with a relatively large carbon solubility such as iron, though many other catalyst particles such as ceramic and semiconducting nanoparticles have been used.[165] The source of carbon is typically a hydrocarbon gas such as ethane, acetylene, or vapors from an organic solvent such as benzene. Within the heat of the furnace, the hydrocarbon feedstock gas decomposes into carbon atoms upon contacting the catalyst surface.[166] The carbon will then saturate the surface layer and begin to recrystallize in the form of graphite. Due to the high curvature of the catalyst particle, and the inability of the carbon to diffuse past the edge of the particle, the recrystallized carbon begins to be extruded in the shape of a tube, thus forming a CNT. The quality of the CNT and its number of walls

depends on the catalyst composition, size, and the temperature of the furnace. In order to obtain SWCNTs, the catalyst particles should be small and the temperature should be high, while for MWNTs, the catalyst particles will be larger and lower temperatures can be used. All of the CNTs used in my work are MWNTs, though their shape may vary as being coiled or linear, and they are organized as aligned arrays or tangled BPs.

A technique that has proven especially useful for MWNT production is the floating catalyst method.[167] In this method, a catalyst precursor is dissolved in a solvent for injection into the furnace as a vapor. Two heating zones are used: one low temperature pre-heating zone for heating the catalyst solution to the point of vaporization, and one high temperature main zone for initiating the formation of catalyst particles and subsequent CNT growth. Ferrocene dissolved in xylene is a typical catalyst solution for this method.[167,168] Once the ferrocene vapors are transported into the main heating zone, it decomposes into metallic iron and two cyclopentadienyl rings. Ferrocene will not decompose in an inert atmosphere below ~1100 K, showing that hydrogen serves a critical role in the decomposition to form iron particles at the temperatures used here.[169,170] In addition to being the solvent for ferrocene, xylene also serves as a carbon source. It decomposes into toluene, benzene, and methane, though most of the nanotube growth comes directly from xylene.[171] Other carbon sources such as ethylene and acetylene can also be introduced during synthesis.

An additional consideration when using acetylene is the purity of the gas. Due to its highly explosive nature, acetylene is typically stored in special cylinders that are filled with

a porous ceramic material to inhibit the spread of a conflagration. The acetylene itself is also dissolved in acetone to reduce its potential for explosion. For this reason, the acetylene gas contains a sizeable fraction of impurities.[172] For cylinder grade acetylene, the major contaminants have been found to be O_2 (0.779%), N_2 (3.78%), and acetone, the concentration of which can vary from 1%-10%, increasing as the cylinder is discharged. Phosphine and H_2 have also been found to be present at 0.06% and 0.023% respectively. The large proportion of acetone contaminants and the propensity of acetylene to polymerize and decompose before reaching the catalyst leads to the buildup of amorphous carbon on the catalyst and nanotubes. The amorphous carbon acts to poison the catalyst and halt CNT growth. This problem can be mitigated by allowing hydrogen or a small portion of water vapor to flow during the synthesis process, which act to etch away the amorphous carbon.

For this work, HCNTs were synthesized in a manner similar to a previous method.[149] They are typically prepared at 750°C, thus stainless steel was selected as the substrate as it can withstand the temperatures required of HCNT synthesis and steel foils could be adapted for use in a continuous process. The steel substrates were prepared by sanding followed by washing in soap and water, then ten minutes of 100 W Ar plasma treatment. They were subsequently coated with 10 nm of aluminum via thermal vapor deposition before being placed inside of a quartz tube positioned in a tube furnace. The main furnace was heated to 750°C and the preheater furnace was heated to 200°C under 500 sccm Ar and 100 sccm H_2 flow. Once the furnaces reached their proper temperatures, a floating catalyst method was used for growing the nanotube arrays.[173] For the VACNTs, 66.7 mg ml^{-1} of ferrocene in

xylene was used as the catalyst while for the HCNTs the mixture was 66.7 mg ml^{-1} ferrocene, 83.2 mg ml^{-1} indium (III) isopropoxide, and 26.4 mg ml^{-1} tin (IV) isopropoxide in xylene. The isopropoxide salts used for HCNT growth are very sensitive to moisture and were handled in a glovebox with less than 10 ppm oxygen and moisture. For proper synthesis, the indium (III) isopropoxide should be an off-white color. If it has been exposed to moisture, it will be orange in color and will not dissolve in the xylene. The tin (IV) isopropoxide should be white. The liquid catalysts were injected into the preheater furnace at 1.5 ml $hour^{-1}$. Simultaneous to injecting the catalyst solution, a flow of acetylene was introduced at 40 sccm. The time of the reaction ranged from 10-40 minutes to obtain arrays of different heights.

4.2.2 BUCKYPAPER FABRICATION

To fabricate the BPs, the as-grown HCNTs and VACNTs were transferred from their steel substrates. To make the BPs, dispersions of HCNTs and MWNTs were prepared such that the CNTs were 0.3 mg ml^{-1} while the surfactant was 3.3 mg ml^{-1}. The surfactant was 25 wt.% SDS and 75 wt.% SLS. About 200 ml of each CNT dispersion was filtered through a Whatman Nylon filter and the resulting BP was peeled from the filter and dried prior to testing. Each BP was rinsed through with 600 ml of water which then allowed a fair comparison of the lignin affinity to each type of CNT. BPs were also soaked in 5 g L^{-1} SLS solution in order to allow further polymer absorption.

4.2.3 CHARACTERIZATION

A Hitachi S-4800 scanning electron microscope was used to determine the heights of the arrays and electrochemical analyses such as cyclic voltammetry (CV) and electrochemical impedance spectroscopy (EIS) were carried out on a Gamry 3000 potentiostat/galvanostat. Raman spectroscopy was performed using a Renishaw inVia micro-Raman system with excitation wavelength of 785 nm. Nanotube samples were taken from the steel current collectors and dispersed in methanol before being drop cast on glass so that Raman measurements could be made of the interior areas and not just the top surface of the arrays, as the surface of the arrays are known to terminate in tangled nanotubes.

To conduct electrochemical analyses, the HCNT/VACNT covered stainless steel pieces were positioned as the working electrodes in a house-built polytetrafluoroethylene 3-electrode test cell where 0.785 cm^2 of the active material is exposed to electrolyte. Platinum mesh was used as the counter electrode, and 1 M $TEABF_4$ in acetonitrile was used as the electrolyte in a voltage range of -1.2 V to 1.2 V with respect to Ag/AgCl. Voltage scan rates of 3, 10, 30, and 100 mV/s were used for cyclic voltammetry, but the capacitance values used in the Fig. 4.3 are calculated from the 100 mV/s dataset only. For the BPs containing SLS, testing was carried out in 1 M HNO_3 in order to promote the redox reaction of the quinone group, with voltage ranging from -0.2 V to 1 V with respect to Ag/AgCl. Acetonitrile is a suitable solvent for use with carbon based EDLCs. However, an aqueous environment is required for the acidic reaction of the SLS in the case of the BPs. The BPs were cycled at 10 A g^{-1} for 10,000 cycles.

4.3 RESULTS AND DISCUSSION

When comparing the capacitance of HCNTs and MWNTs grown on steel substrates, the capacitance values were not normalized by mass due to difficulties involved with weighing the active area after exposing CNTs to the solvent and electrolyte salts. Instead, the performance was normalized by the array height and electrode area as reported in a previous publication demonstrating the roll-to-roll production of CNTs on Al foil.[137] SEM images of CNT arrays of different heights are shown in Fig. 4.2a. Examples of typical CV curves for VACNTs and HCNTs are shown in Figs. 4.2a and 4.2b respectively, showing a purely capacitive response, as expected since no redox component is present. The specific capacitance values of HCNTs and VACNTs as a function of array height are shown in Figs. 4.3a and 4.3b respectively. In order to determine the uncertainty in array heights, several sites on each substrate were analyzed via SEM and their heights were averaged. The slopes of the linear fits to the data indicate that the capacitance of the HCNTs exceeds that of the VACNTs for the pristine samples that were not exposed to plasma. This result is likely due to a combination of greater surface area for the HCNTs as well as a greater density of inherent defects as shown by the Raman spectra in Fig. 4.3d. Contrary to the initial prediction, the plasma treated VACNTs display greater capacitance than the plasma treated HCNTs as evinced by their respective slopes. The VACNTs only showed a small change in the slope after plasma treatment, an increase of 4%, while the HCNTs showed a slope decrease of 28%. Previous work has shown that Ar plasma can be used to enhance the capacitance of carbon nanostructures through the addition of extrinsic

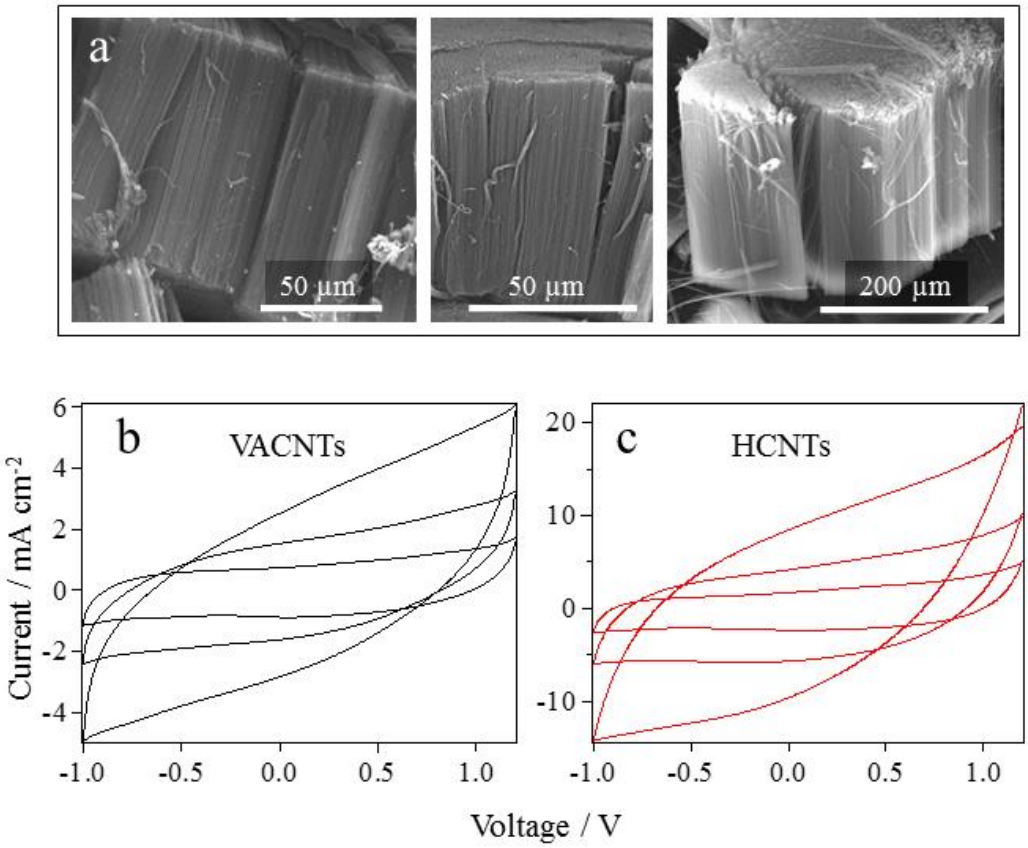

Figure 4.2: a) SEM images showing CNT arrays of different heights. b) and c) Cyclic voltammograms taken at several scan rates for VACNTs and HCNTs respectively of a given height.

defects,[152,174] but the effects were found to be deleterious to the performance of HCNTs in this case. The greater amount of inherent defects in the HCNTs likely contribute to their susceptibility to further structural damage caused by Ar plasma. When comparing the surfaces of straight versus coiled nanotubes, the surface energy of the coiled tubes will be greater due to the torsional stresses on the hexagonal lattice of the tube walls.[147] This higher surface energy would reduce the energy barrier required for creating defects in the surface via plasma treatment. The plasma treated VACNTs do not display significant

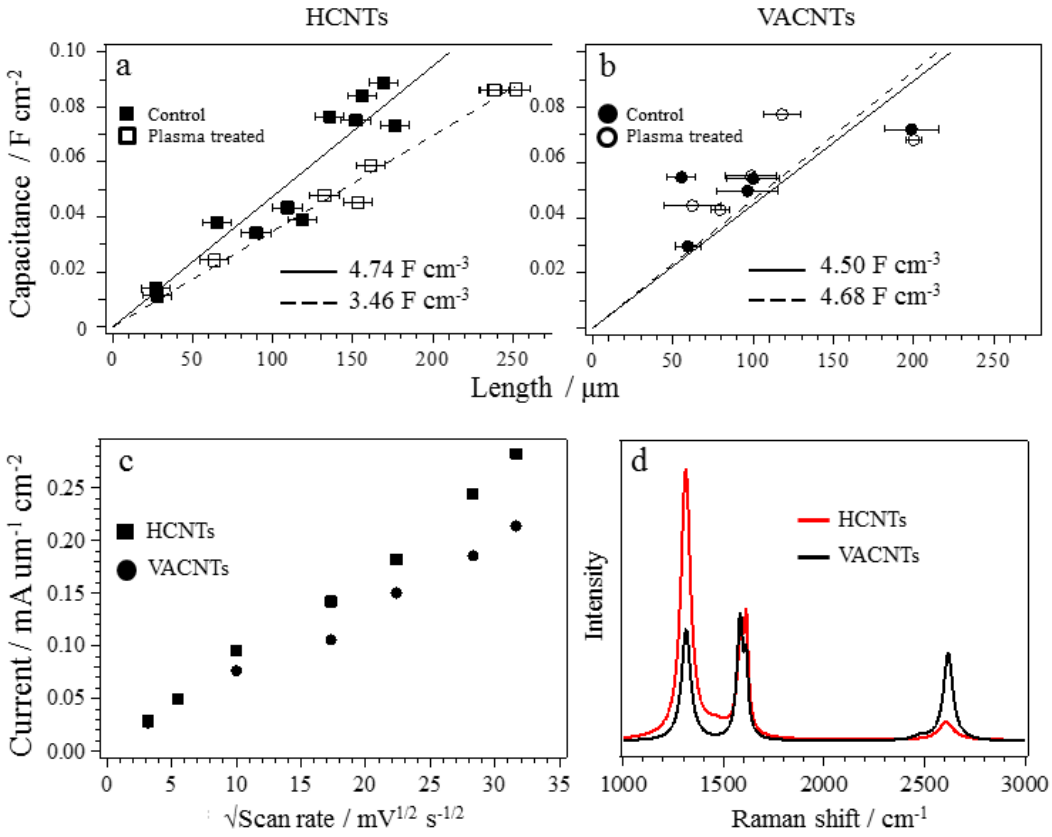

Figure 4.3: a) and b) show capacitance versus array height for HCNTs and VACNTs recorded at 100 mV s^{-1}. The data compare control samples to those exposed to 100 W Ar plasma for 10 minutes. The slopes of the trend lines are shown below the data. The HCNTs showed a greater change in capacitance after plasma treatment than the VACNTs as shown by their respective trend lines. The HCNT slope decreased by 28% while the VACNT slope increased by only 4%. c) Current vs the square root of scan rate demonstrates linear trends. d) The Raman spectra shows HCNTs have a more prominent *D*-band at 1350 cm^{-1} than the VACNTs.

improvement over the control. A possible explanation for this is that the plasma is only affecting the outer wall of the multi-walled nanotubes. Jorio et al. have studied similar

effects by subjecting multiple layers of graphene to Ar ion bombardment.[175] They found that the ions only affected the outer layers of the graphene which would be analogous to the MWNTs in this case. CNT arrays grown on steel substrates by the ferrocene/xylene method using acetylene also tend to have a large number of defects as indicated by the Raman spectra. Nyquist plots of HCNT EIS impedance data (not shown) show a difference in the series resistance between HCNTs and VACNTs. The series resistances of VACNTs obtained through EIS are approximately the same for several samples while the HCNTs display much more variation, likely due to a relatively poor adhesion of the mixed Fe/Sn/In catalyst particles to the steel substrate. This has been observed in past studies that found HCNTs tend to grow via the tip growth mechanism as opposed to root growth where the catalyst particle remains in contact with the substrate.[150,176] To determine how the linear and helically coiled morphologies affect ion diffusion, peak current versus the square root of scan rate are plotted in Fig. 4.3c. The VACNT and HCNT samples demonstrating the best electrochemical characteristics were used for the comparison. The trend remains linear after the initial low scan rates for HCNTs and VACNTs, indicating diffusion limited charge/discharge behavior for each sample.

To summarize the first part of the study, the HCNTs demonstrated superior capacitance to the VACNTs prior to plasma treatment, but suffered a greater loss in performance subsequent to plasma treatment.

The results for the BPs will now be discussed. The structure of the HCNTs can be seen in Fig. 4.4a. The SEM image shows a cross section of an HCNT array while the inset TEM

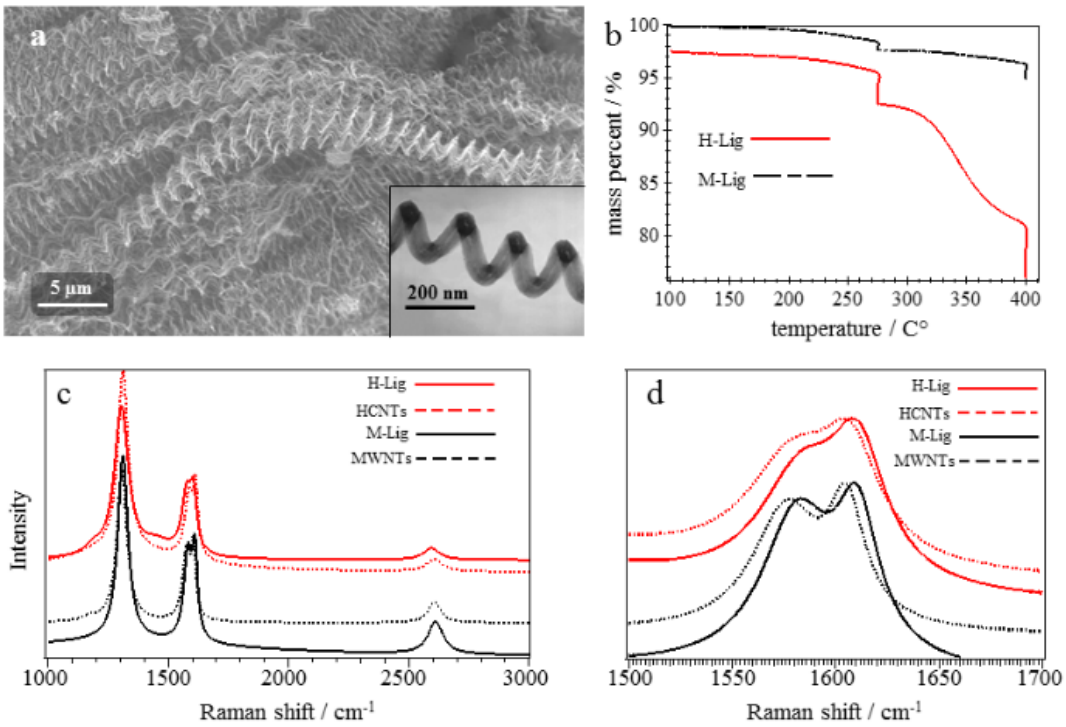

Figure 4.4: a) SEM image of HCNTs. The inset is a TEM image of a single helically coiled nanotube. b) TGA results of BPs made from HCNTs and MWNTs. The lignin begins to burn off above 300°C and the HCNTs were found to hold more lignin than MWNTs by mass percent. HCNTs also contained more SDS which is seen to burn off above 250°C. c) Raman spectra of pristine HCNTs and MWNTs compared to lignin infused BPs, taken with 785 nm excitation. d) Magnified view of the *G*-band. The *G*-band up-shifts after the lignin is adsorbed, indicating some degree of charge abstraction from the graphitic lattice.

image shows a closer view of the helicity of the nanotubes. When preparing the BPs from HCNTs and MWNTs, caution was taken to maintain the same mass ratios of surfactant to CNTs. The thermal gravimetric profile of each type of BP is shown in Fig. 4.4b. From the

large difference in the loss of mass, it is evident that the HCNTs retained several times more polymer than the MWNTs. The drop in mass at 275°C is due to the loss of SDS surfactant while the loss starting after 300°C is attributed to SLS. From the TGA of the surfactants (not shown), SDS was found to degrade much faster and more suddenly than SLS. This is to be expected as the molecular structure of polymeric SLS is much more complex than that of SDS. Beyond the helical structure, defects may also play a role in the superior adsorption of lignin by the HCNTs. The altered charge density localized to defects within the hexagonal lattice is known to have an effect on the binding energy of adsorbates.[177–179] This effect could promote the adsorption of SLS onto HCNTs over MWNTs due to the larger amount defects present in HCNTs. Evidence for surfactant adsorption can also be found in the Raman spectra of the prepared BPs. Raman spectra for each type of BP as well as the bare CNTs are shown in Figs. 4.4c and 4.4d. The spectra were taken with 785 nm excitation and the *G*-band feature can be found at ~1580 cm^{-1}. When polymer is adsorbed to the surface of the CNTs, the vibrational modes of the hexagonal lattice are affected by the altered charge distribution, resulting in a shift of the *G*-band of a few wave numbers. This effect is seen in Fig. 4.4d where the *G*-band peaks are magnified. The *G*-band for MWNTs shifts from 1577 to 1584 cm^{-1} while for the HCNTs it shifted from 1580 to 1586 cm^{-1}. These shifts were found to remain consistent between multiple spectra. Previous work on this topic found that polymer adsorption resulted in an upshift of the *G*-band by ~10 cm^{-1} and claimed it was due to van der Waals forces between the polymer and nanotube that increase the energy necessary for vibrations to occur.[180,181] It is also well known from the literature on graphite intercalation

compounds that the *G*-band frequency will upshift when in the presence of an electron accepting intercalant.[99]

The electrochemical characteristics of each type of BP are displayed in Fig. 4.5. Figure 4.5a shows the redox reaction of lignin that occurs during cycling of the BPs. Nyquist plots of the impedance data for the BPs taken before and after 10,000 cycles at 10 A g^{-1} are displayed in Fig. 4.5b. The HCNTs are seen to possess a slightly lower series resistance than the MWNTs, and the high frequency semi-circle is seen to become slightly depressed after cycling, almost forming a second semi-circle. The BPs were also tested after being soaked in a 5 g L^{-1} SLS solution for 24 hours in order to absorb more polymer. The soaking resulted in an increase of mass by 6% for the HCNTs and 2% for the MWNTs as determined by microbalance measurements. These soaked samples displayed similar EIS spectra to those found in Fig. 4.5b. In Fig 4.5c, typical mass normalized CV curves for the BPs are displayed. Data is also displayed for a BP that was compressed at ~170 lbs in^{-2}. The redox reaction of the SLS associated with the quinone group takes place from ~0.55 to 0.6 V and is highly reversible under the present conditions. The larger peak was found to diminish after compression of the BPs, indicating less charge transfer was able to occur for that case. Conversely, the smaller peak was unaffected by the compression indicating it may be due to a different source than the redox reaction of the quinone group. In a traditional Randles cell, the diameter of the semi-circle in the Nyquist plot is indicative of charge transfer resistance between the electroactive species and the active material of the electrode. In this case however, the diameter is also related to the diffusion

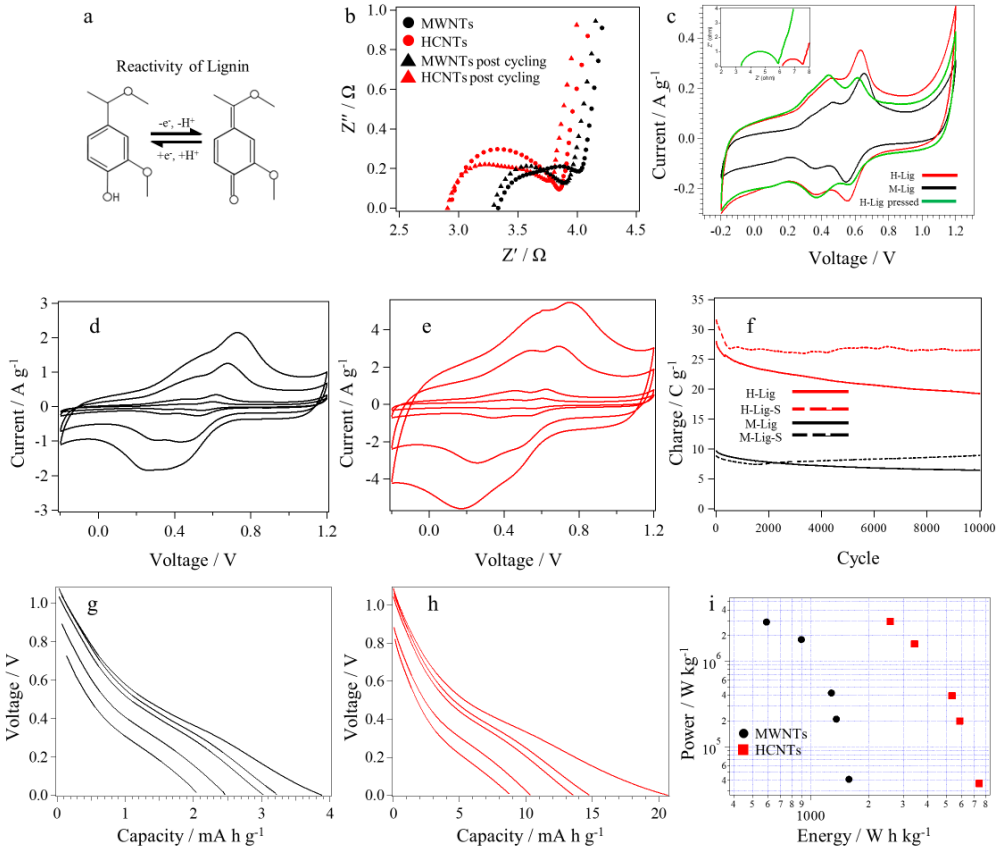

Figure 4.5: Electrochemical data for as-prepared and lignin solution soaked BPs. HCNTs and MWNTs are prefixed as H and M respectively, while the BPs soaked in lignin solution are suffixed with S. a) Redox reaction of SLS in acidic media. b) Nyquist plot for the BPs are compared before and after cycling. c) Comparison of CV curves taken at 3 mV s^{-1} for HCNTs and MWNTs. The capacitances measured from the curves of the HCNTs and MWNTs are 593 mF cm^{-2} (125.0 F g^{-1}) and 379 mF cm^{-2} (69.7 F g^{-1}), respectively. The inset shows Nyquist plots for an HCNT BP before and after pressing. d) and e) CV curves of MWNT and HCNT BPs respectively, taken at scan rates ranging from 3-100 mV s^{-1}. Comparison of the capacity of each type of sample after 10000 cycles at 10 A g^{-1}. g) and h) Discharge curves for MWNT and HCNT BPs respectively, ranging from 10 A g^{-1} to 0.1 A g^{-1}. i) Ragone plot showing power and energy densities.

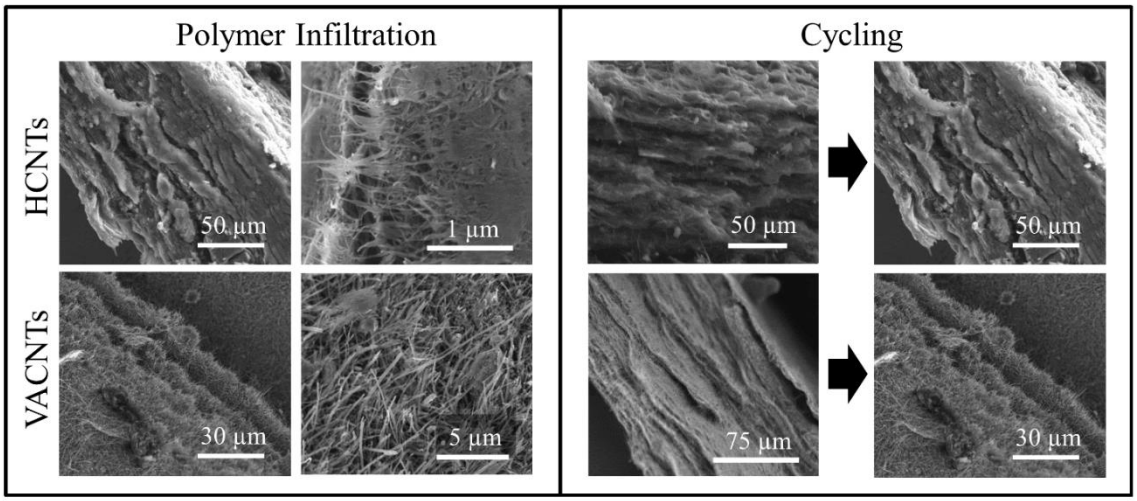

Figure 4.6: Left) SEM images showing HCNTs (top) and MWNTs (bottom) after soaking in SLS solution. Right) HCNTs and VACNTs before and after 10,000 cycles at 10 A g^{-1}.

resistance of ions migrating through the CNT/polymer system. This was confirmed by conducting EIS on the compressed BP specimen. This data is shown in the inset of Fig. 4.5c. By compressing the BP, the ability of molecules to diffuse through the system would be hindered while the series resistance would be decreased due to greater connectivity within the electrode. The reduced series resistance is shown by the Z' intercept which is seen to decrease for the compressed sample. Concomitant with the reduced series resistance is an increase in the semi-circle diameter. It thus stands to reason that the increased diameter is related to the increased diffusion resistance. Past research found similar effects for the case of porous sulfur electrodes where compression led to an increase in semi-circle diameter.[40] The capacitance of the HCNT BPs was found to be superior to the MWNT BPs at all scan rates. This is reflected by the CV curves shown in Figs. 4.5d and 4.5e for

VACNTs and HCNTs respectively. The cycling rates here ranged from 3 mV s^{-1} to 100 mV s^{-1}. For the 3 mV s^{-1} CV curves shown in Fig. 4.5c, the measured capacitances of the HCNT and MWNT BPs are 593 mF cm^{-2} (125.0 F g^{-1}) and 379 mF cm^{-2} (69.7 F g^{-1}) respectively. To investigate the durability of the BP electrodes, they were cycled at a rate 10 A g^{-1} for 10,000 cycles as shown in Fig. 4.5f. The BPs that were soaked in SLS showed an obvious improvement in capacity after soaking. The increase in capacity is much greater for the HCNT BP compared to the smaller improvement for the MWNT BP, due to the greater amount of adsorbed SLS in the former. Overall, the HCNT BPs demonstrate superior capacity to the MWNTs. Traces showing the discharge capacity of the BPs are shown in Figs. 4.5g and 4.5h. The discharge rates ranged from 10 A g^{-1} to 0.1 A g^{-1}. Data from the discharge process is also displayed as a Ragone plot in Fig. 4.5i. While the HCNT BPs show greater energy density relative to MWNT BPs, their power densities and capacity fade are similar.

Structural changes caused by soaking and cycling are shown by SEM images in Fig. 4.6. The images shown in the left panel of Fig. 4.6 show HCNT and MWNT BPs after soaking in SLS solution. A cross section of the BPs showing their layered structure and gallery space as well as a magnified image are shown. In the magnified image, the HCNTs are seen to be embedded in polymer while the coating for the MWNTs is sparser. The right panel shows changes associated with cycling of the BPs. From the images, no apparent difference in the structure of the BPs is observed, consistent with their robust mechanical properties.

4.4 CONCLUSIONS

I have grown HCNTs to determine their effectiveness as capacitor electrodes and compared their performance to electrodes made from VACNTs and MWNT BPs. The capacitance of electrodes made from HCNT and VACNT arrays display a linear dependence on height and showed diffusion limited behavior below the maximum scan rate studied of 1 V s^{-1}. The HCNT arrays demonstrated greater capacitance than their VACNT analogs, but had greater susceptibility to the plasma treatment, which was detrimental to their performance. However, the HCNTs showed a superior ability to adsorb polymer when made into BPs and displayed capacitance values far exceeding BPs made from MWNTs as well as the arrays of HCNTs and VACNTs. This shows that HCNTs are well suited for use as binderless electrodes that can be augmented with electroactive polymers.

REFERENCES

[1] K.S. Novoselov, A.K. Geim, S. V Morozov, D. Jiang, Y. Zhang, S. V Dubonos, I. V Grigorieva, A.A. Firsov, Science 306 (2004) 666–9.

[2] S. V Morozov, K.S. Novoselov, F. Schedin, D. Jiang, A.A. Firsov, A.K. Geim, Phys. Rev. B - Condens. Matter Mater. Phys. 72 (2005) 2–5.

[3] K.S. Novoselov, A.K. Geim, S. V Morozov, D. Jiang, M.I. Katsnelson, I. V Grigorieva, S. V Dubonos, A.A. Firsov, Nature 438 (2005) 197–200.

[4] A.A. Balandin, S. Ghosh, W. Bao, I. Calizo, D. Teweldebrhan, F. Miao, C.N. Lau, Nano Lett. 8 (2008) 902–907.

[5] H. Kataura, Y. Kumazawa, Y. Maniwa, I. Umezu, S. Suzuki, Y. Ohtsuka, Y. Achiba, Synth. Met. 103 (1999) 2555–2558.

[6] A.J. Bard, L.R. Faulkner, Electrochemical Methods: Fundamentals and Applications, John Wiley and Sons, 2001.

[7] M. Gouy, J. Phys. Théorique Appliquée 9 (1910) 457–468.

[8] D.L. Chapman, London, Edinburgh, Dublin Philos. Mag. J. Sci. 25 (1913) 475–481.

[9] J. Chmiola, G. Yushin, Y. Gogotsi, C. Portet, P. Simon, P.L. Taberna, Science (80-.). 313 (2006) 1760–1763.

[10] R.H. Baughman, Science (80-.). 297 (2002) 787–792.

[11] K.H. An, W.S. Kim, Y.S. Park, J.-M. Moon, D.J. Bae, S.C. Lim, Y.S. Lee, Y.H. Lee, Adv. Funct. Mater. 11 (2001) 387–392.

[12] E. Frackowiak, F. Béguin, Carbon N. Y. 40 (2002) 1775–1787.

[13] Y. Honda, T. Haramoto, M. Takeshige, H. Shiozaki, T. Kitamura, M. Ishikawa, Electrochem. Solid-State Lett. 10 (2007) A106.

[14] D.N. Futaba, K. Hata, T. Yamada, T. Hiraoka, Y. Hayamizu, Y. Kakudate, O. Tanaike, H. Hatori, M. Yumura, S. Iijima, Nat. Mater. 5 (2006) 987–994.

[15] C. Du, J. Yeh, N. Pan, Nanotechnology 16 (2005) 350–353.

[16] J. Chen, C. Li, G. Shi, J. Phys. Chem. Lett. 4 (2013) 1244–1253.

[17] W.-Y. Tsai, R. Lin, S. Murali, L. Li Zhang, J.K. McDonough, R.S. Ruoff, P.-L. Taberna, Y. Gogotsi, P. Simon, Nano Energy 2 (2013) 403–411.

[18] M.S. Wang, W.L. Song, L.Z. Fan, ChemElectroChem 2 (2015) 1699–1706.

[19] B. Rangasamy, J.Y. Hwang, W. Choi, Carbon N. Y. 77 (2014) 1065–1072.

[20] H. Yue, Q. Li, D. Liu, X. Hou, S. Bai, S. Lin, D. He, J. Alloys Compd. 744 (2018) 243–251.

[21] G. Zhou, F. Li, H.-M. Cheng, Energy Environ. Sci. 7 (2014) 1307–1338.

[22] B.J. Landi, M.J. Ganter, C.D. Cress, R.A. DiLeo, R.P. Raffaelle, Energy Environ. Sci. 2 (2009) 638.

[23] M. Volder, S. Tawfick, R. Baughman, A.J. Hart, Science (80-.). 339 (2013) 535–539.

[24] J. Guo, Y. Xu, C. Wang, Nano Lett. 11 (2011) 4288–4294.

[25] Y. Wang, H.C. Zeng, J.Y. Lee, Adv. Mater. 18 (2006) 645–649.

[26] Z. Wen, Q. Wang, Q. Zhang, J. Li, Adv. Funct. Mater. 17 (2007) 2772–2778.

[27] L.-F. Cui, L. Hu, J.W. Choi, Y. Cui, ACS Nano 4 (2010) 3671–3678.

[28] K. Evanoff, J. Khan, A.A. Balandin, A. Magasinski, W.J. Ready, T.F. Fuller, G. Yushin, Adv. Mater. 24 (2012) 533–537.

[29] W.C. Forsman, T. Dziemianowicz, K. Leong, D. Carl, Synth. Met. 5 (1983) 77–100.

[30] L.B. Ebert, Annu. Rev. Mater. Sci. 6 (1976) 181–211.

[31] A.G. Khachaturyan, Phys. Status Solidi 60 (1973) 9–37.

[32] S.A. Safran, Phys. Rev. Lett. 44 (1980) 937–940.

[33] C. Liu, Z.G. Neale, G. Cao, Mater. Today 19 (2016).

[34] M. Orazem, B. Tribollet, Electrochemical Impedance Spectroscopy, John Wiley and Sons, 2008.

[35] J. Gomez, R. Nelson, E.E. Kalu, M.H. Weatherspoon, J.P. Zheng, J. Power Sources 196 (2011) 4826–4831.

[36] M. Doyle, J.P. Meyers, J. Newman, J. Electrochem. Soc. 147 (2000) 99.

[37] F. La Mantia, J. Vetter, P. Novák, Electrochim. Acta 53 (2008) 4109–4121.

[38] B. Markovsky, M.D. Levi, D. Aurbach, Electrochim. Acta 43 (1998) 2287–2304.

[39] M. Itagaki, N. Kobari, S. Yotsuda, K. Watanabe, S. Kinoshita, M. Ue, J. Power Sources 135 (2004) 255–261.

[40] C. Barchasz, J.-C. Leprêtre, F. Alloin, S. Patoux, J. Power Sources 199 (2011) 322–330.

[41] P.L. Moss, G. Au, E.J. Plichta, J.P. Zheng, J. Electrochem. Soc. 155 (2008) A986.

[42] J.Y. Song, H.H. Lee, Y.Y. Wang, C.C. Wan, J. Power Sources 111 (2002) 255–267.

[43] A. Jorio, M. Dresselhaus, R. Saito, G. Dresselhaus, Raman Spectroscopy of Graphene Related Systems, Wiley-VCH Verlag, 2011.

[44] C. Thomsen, S. Reich, Phys. Rev. Lett. 85 (2000) 5214–5217.

[45] F. Tuinstra, J.L. Koenig, J. Chem. Phys. 53 (1970) 1126.

[46] M.Z. Jacobson, M.A. Delucchi, Energy Policy 39 (2011) 1154–1169.

[47] M. Fleischer, Circ. Geol. Surv. 285 (1953) 1–6.

[48] Q.F. Li, N.J. Bjerrum, J. Power Sources 110 (2002) 1–10.

[49] G.A. Elia, K. Marquardt, K. Hoeppner, S. Fantini, R. Lin, E. Knipping, W. Peters, J.-F. Drillet, S. Passerini, R. Hahn, Adv. Mater. (2016).

[50] J.S. Wilkes, J.A. Levisky, R.A. Wilson, C.L. Hussey, Inorg. Chem. 21 (1982) 1263–1264.

[51] J.S. Wilkes, J.A. Levisky, Rep. FJSRL-TR-81-0001 0 (1981).

[52] B.J. Piersma, J.S. Wilkes, Frank J. Seiler Res. Lab. Tech. Rep. FJSRL-TR-82-0004 (1982).

[53] A.A. Fannin, L.A. King, J.A. Levisky, J.S. Wilkes, J. Phys. Chem. 88 (1984) 2609–2614.

[54] J.J. Auborn, Y.L. Barberio, J. Electrochem. Soc. 132 (1985) 598–601.

[55] P.K. Lai, M. Skyllas-Kazacos, J. Electroanal. Chem. 248 (1988) 431–440.

[56] H.A. Øye, M. Jagtoyen, T. Oksefjell, J.S. Wilkes, Mater. Sci. Forum 73-75 (1991) 183–190.

[57] T. Jiang, M.J.C. Brym, G. Dube, A. Lasia, G.M. Brisard, Surf. Coat. Technol. 201 (2006) 1–9.

[58] R.T. Carlin, H.C. Delong, J. Fuller, P.C. Trulove, J. Electrochem. Soc. 141 (1994) L73–L76.

[59] N. Jayaprakash, S.K. Das, L.A. Archer, Chem. Commun. 47 (2011) 12610–12612.

[60] G. Cohn, L. Ma, L.A. Archer, A Novel Non-Aqueous Aluminum Sulfur Battery, 2015.

[61] H. Sun, W. Wang, Z. Yu, Y. Yuan, S. Wang, S. Jiao, Chem. Commun. 51 (2015) 11892–11895.

[62] M.C. Lin, M. Gong, B.G. Lu, Y.P. Wu, D.Y. Wang, M.Y. Guan, M. Angell, C.X. Chen, J. Yang, B.J. Hwang, H.J. Dai, Nature 520 (2015) 325.

[63] J. V. Rani, V. Kanakaiah, T. Dadmal, M.S. Rao, S. Bhavanarushi, J. Electrochem. Soc. 160 (2013) A1781–A1784.

[64] P.R. Gifford, J.B. Palmisano, J. Electrochem. Soc. 135 (1988) 650–654.

[65] M. Chiku, H. Takeda, S. Matsumura, E. Higuchi, H. Inoue, ACS Appl. Mater. Interfaces 7 (2015) 24385–24389.

[66] H. Wang, Y. Bai, S. Chen, X. Luo, C. Wu, F. Wu, J. Lu, K. Amine, ACS Appl. Mater. Interfaces 7 (2015) 80–84.

[67] J. Hu, J. Ma, L. Wang, H. Huang, L. Ma, Powder Technol. 254 (2014) 556–562.

[68] W. Wang, B. Jiang, W. Xiong, H. Sun, Z. Lin, L. Hu, J. Tu, J. Hou, H. Zhu, S. Jiao, Sci. Rep. 3 (2013) 2093–2104.

[69] R. Raccichini, A. Varzi, S. Passerini, B. Scrosati, Nat. Mater. 14 (2014) 271–279.

[70] F. Bonaccorso, L. Colombo, G. Yu, M. Stoller, V. Tozzini, A.C. Ferrari, R.S. Ruoff, V. Pellegrini, Science (80-.). 347 (2015) 1246501–1246501.

[71] C. Hu, L. Song, Z. Zhang, N. Chen, Z. Feng, L. Qu, Energy Environ. Sci. 8 (2015) 31–54.

[72] W. Lv, Z. Li, Y. Deng, Q.-H. Yang, F. Kang, Energy Storage Mater. 2 (2016) 107–138.

[73] A.A. Fannin, L. a. King, J. a. Levisky, J.S. Wilkes, J. Phys. Chem. 88 (1984) 2609–2614.

[74] S. Takahashi, L.A. Curtiss, D. Gosztola, N. Koura, M.-L. Saboungi, Inorg. Chem 34 (1995) 2990–2993.

[75] S.C. Jung, Y.J. Kang, D.J. Yoo, J.W. Choi, Y.K. Han, J. Phys. Chem. C 120 (2016) 13384–13389.

[76] M.S. Wu, B. Xu, L.Q. Chen, C.Y. Ouyang, Electrochim. Acta 195 (2016) 158–165.

[77] J. Zhu, A.S. Childress, M. Karakaya, S. Dandeliya, A. Srivastava, Y. Lin, A.M. Rao, R. Podila, Adv. Mater. 28 (2016) 7185–7192.

[78] X. Yu, B. Wang, D. Gong, Z. Xu, B. Lu, Adv. Mater. 29 (2016) 1604118.

[79] L. Zhang, L. Chen, H. Luo, X. Zhou, Z. Liu, Adv. Energy Mater. (2017) 1700034.

[80] K. Share, A.P. Cohn, R. Carter, B. Rogers, C.L. Pint, ACS Nano 10 (2016) 9738–9744.

[81] H. Wang, C. Zhang, Z. Liu, L. Wang, P. Han, H. Xu, K. Zhang, S. Dong, J. Yao, G. Cui, A.K. Geim, M. Rühle, D.L. Carroll, J. Mater. Chem. 21 (2011) 5430.

[82] Z.-S. Wu, W. Ren, L. Xu, F. Li, H.-M. Cheng, ACS Nano 5 (2011) 5463–5471.

[83] J.J. Lander, H.E. Kern, A.L. Beach, J. Appl. Phys. 23 (1952) 1305–1309.

[84] L. Baraton, Z.B. He, C.S. Lee, C.S. Cojocaru, M. Châtelet, J.-L. Maurice, Y.H. Lee, D. Pribat, EPL (Europhysics Lett. 96 (2011) 46003.

[85] Z. Chen, W. Ren, L. Gao, B. Liu, S. Pei, H.-M. Cheng, Nat. Mater. 10 (2011) 424–428.

[86] R. Santhanam, M. Noel, J. Power Sources 63 (1996) 1–6.

[87] M.D. Levi, D. Aurbach, J. Electroanal. Chem. 421 (1997) 79–88.

[88] M.D. Levi, E.A. Levi, D. Aurbach, J. Electroanal. Chem. 421 (1997) 89–97.

[89] M. Noel, V. Suryanarayanan, J. Power Sources 111 (2002) 193–209.

[90] J. Song, D. Chung, P. Ekiund, M. Dresselhaus, Solid State Commun. 20 (1976) 1111–1115.

[91] S.A. Solin, Mater. Sci. Eng. 31 (1977) 153–156.

[92] R.J. Nemanich, S.A. Solin, D. Guerard, Phys. Rev. B 16 (1977) 2965–2972.

[93] J.C. Chacón-Torres, L. Wirtz, T. Pichler, ACS Nano 7 (2013) 9249–59.

[94] J.C. Chacón-Torres, L. Wirtz, T. Pichler, Phys. Status Solidi 251 (2014) 2337–2355.

[95] N. Jung, N. Kim, S. Jockusch, N.J. Turro, P. Kim, L. Brus, Nano Lett. 9 (2009) 4133–4137.

[96] K. Share, A.P. Cohn, R.E. Carter, C.L. Pint, Nanoscale 8 (2016) 16435–16439.

[97] P.C. Eklund, E.T. Arakawa, J.L. Zarestky, W.A. Kamitakahara, G.D. Mahan, Synth. Met. 12 (1985) 97–102.

[98] M. Inaba, H. Yoshida, Z. Ogumi, T. Abe, Y. Mizutani, M. Asano, J. Electrochem. Soc. 142 (1995) 20.

[99] M.S. Dresselhaus, G. Dresselhaus, Adv. Phys. 51 (2002) 1–186.

[100] C. Gómez-Navarro, R.T. Weitz, A.M. Bittner, M. Scolari, A. Mews, M. Burghard, K. Kern, Nano Lett. 7 (2007) 3499–3503.

[101] W. Tian, W. Li, W. Yu, X. Liu, Micromachines 8 (2017) 163.

[102] N. Gorjizadeh, A.A. Farajian, Y. Kawazoe, Nanotechnology 20 (2009) 015201.

[103] L. Vicarelli, S.J. Heerema, C. Dekker, H.W. Zandbergen, ACS Nano 9 (2015) 3428–35.

[104] C.J. Shearer, A.D. Slattery, A.J. Stapleton, J.G. Shapter, C.T. Gibson, Nanotechnology 27 (2016) 125704.

[105] Z. Wang, L. Qie, L. Yuan, W. Zhang, X. Hu, Y. Huang, Carbon N. Y. 55 (2013) 328–334.

[106] H. Wang, Z. Wu , F. Meng , D. Ma , X. Huang , L. Wang, X. Zhang, ChemSusChem 6 (2013) 56–60.

[107] A.L.M. Reddy, A. Srivastava, S.R. Gowda, H. Gullapalli, M. Dubey, P.M. Ajayan, ACS Nano 4 (2010) 6337–6342.

[108] Y.J. Cho, H.S. Kim, H. Im, Y. Myung, G.B. Jung, C.W. Lee, J. Park, M.-H. Park, J. Cho, H.S. Kang, J. Phys. Chem. C 115 (2011) 9451–9457.

[109] H. Wang, C. Zhang, Z. Liu, L. Wang, P. Han, H. Xu, K. Zhang, S. Dong, J. Yao, G. Cui, A.K. Geim, M. Rühle, D.L. Carroll, J. Mater. Chem. 21 (2011) 5430.

[110] N. Ketabi, T. de Boer, M. Karakaya, J. Zhu, R. Podila, A.M. Rao, E.Z. Kurmaev, A. Moewes, T. Hayashi, J. Kong, H. Terrones, G. Dresselhaus, M. Endo, M. Terrones, M.S. Dresselhaus, M.S. Hybertsen, A.N. Pasupathy, RSC Adv. 6 (2016) 56721–56727.

[111] T. Schiros, D. Nordlund, L. Pálová, D. Prezzi, L. Zhao, K.S. Kim, U. Wurstbauer, C. Gutiérrez, D. Delongchamp, C. Jaye, D. Fischer, H. Ogasawara, L.G.M. Pettersson, D.R. Reichman, P. Kim, M.S. Hybertsen, A.N. Pasupathy, Nano Lett. 12 (2012) 4025–4031.

[112] D. Usachov, A. Fedorov, O. Vilkov, B. Senkovskiy, V.K. Adamchuk, L. V. Yashina, A.A. Volykhov, M. Farjam, N.I. Verbitskiy, A. Grüneis, C. Laubschat, D. V. Vyalikh, Nano Lett. 14 (2014) 4982–4988.

[113] Y.-F. Lu, S.-T. Lo, J.-C. Lin, W. Zhang, J.-Y. Lu, F.-H. Liu, C.-M. Tseng, Y.-H. Lee, C.-T. Liang, L.-J. Li, ACS Nano 7 (2013) 6522–6532.

[114] J. Zhang, C. Zhao, N. Liu, H. Zhang, J. Liu, Y.Q. Fu, B. Guo, Z. Wang, S. Lei, P.A. Hu, Sci. Rep. 6 (2016) 28330.

[115] R. Podila, J. Chacón-Torres, J.T. Spear, T. Pichler, P. Ayala, A.M. Rao, Appl. Phys. Lett. 101 (2012) 123108.

[116] A.C. Ferrari, Solid State Commun. 143 (2007) 47–57.

[117] M. Rybin, A. Pereyaslavtsev, T. Vasilieva, V. Myasnikov, I. Sokolov, A. Pavlova, E. Obraztsova, A. Khomich, V. Ralchenko, E. Obraztsova, Carbon N. Y. 96 (2016) 196–202.

[118] C.E. Banks, T.J. Davies, G.G. Wildgoose, R.G. Compton, Chem. Commun. (2005) 829–

841.

[119] G. Abbas, P. Papakonstantinou, G.R.S. Iyer, I.W. Kirkman, L.C. Chen, Phys. Rev. B - Condens. Matter Mater. Phys. 75 (2007).

[120] A.S. Childress, P. Parajuli, J. Zhu, R. Podila, A.M. Rao, Nano Energy 39 (2017) 69–76.

[121] J. Wu, L. Ma, R.M. Yadav, Y. Yang, X. Zhang, R. Vajtai, J. Lou, P.M. Ajayan, ACS Appl. Mater. Interfaces 7 (2015) 14763–14769.

[122] Y. Shao, S. Zhang, M.H. Engelhard, G. Li, G. Shao, Y. Wang, J. Liu, I.A. Aksay, Y. Lin, J. Mater. Chem. 20 (2010) 7491.

[123] D.S. Su , J. Zhang, B. Frank, A. Thomas, X. Wang, J. Paraknowitsch, R. Schlögl, ChemSusChem 3 (2010) 169–180.

[124] J. Liu, D. Takeshi, D. Orejon, K. Sasaki, S.M. Lyth, J. Electrochem. Soc. 161 (2014) 544–550.

[125] G.M. Gualberto, C. Underhill, S.Y. Leung, G. Dresselhaus, Phys. Rev. B 21 (1980) 862–868.

[126] L.L. Zhang, X.S. Zhao, Chem. Soc. Rev. 38 (2009) 2520–2531.

[127] W.T. Gu, G. Yushin, Wiley Interdiscip. Rev. Environ. 3 (2014) 424–473.

[128] G. Atthipalli, Y. Tang, A. Star, J.L. Gray, Thin Solid Films 520 (2011) 1651–1655.

[129] S. Dorfler, I. Felhosi, T. Marek, S. Thieme, H. Althues, L. Nyikos, S. Kaskel, J. Power Sources 227 (2013) 218–228.

[130] K.Y. Lee, Y.S. Lin, Y.M. Chen, Y.S. Huang, Phys. E-Low-Dimensional Syst. Nanostructures 42 (2010) 2799–2803.

[131] W. Lu, L.T. Qu, K. Henry, L.M. Dai, J. Power Sources 189 (2009) 1270–1277.

[132] M. Noked, S. Okashy, T. Zimrin, D. Aurbach, Carbon N. Y. 58 (2013) 134–138.

[133] C.L. Pint, N.W. Nicholas, S. Xu, Z.Z. Sun, J.M. Tour, H.K. Schmidt, R.G. Gordon, R.H. Hauge, Carbon N. Y. 49 (2011) 4890–4897.

[134] R. Reit, J. Nguyen, W.J. Ready, Electrochim. Acta 91 (2013) 96–100.

[135] R. Shah, X.F. Zhang, S. Talapatra, Nanotechnology 20 (2009) 395202.

[136] D. Villoria, A.J. Hart, B.L. Wardle, R. Guzma, (2011) 4850–4857.

[137] M.R. Arcila-Velez, J. Zhu, A. Childress, M. Karakaya, R. Podila, A.M. Rao, M.E. Roberts, Nano Energy 8 (2014) 9–16.

[138] L. Oakes, T. Hanken, R. Carter, W. Yates, C.L. Pint, ACS Appl. Mater. Interfaces 7 (2015) 14201–14210.

[139] M. Karakaya, J. Zhu, A.J. Raghavendra, R. Podila, S.G.P. Jr, P. James, A.M. Rao, M. Karakaya, J. Zhu, A.J. Raghavendra, 263103 (2014).

[140] C. Daraio, V.F. Nesterenko, S. Jin, W. Wang, A.M. Rao, J. Appl. Phys. 100 (2006) 064309.

[141] R. Thevamaran, M. Karakaya, E.R. Meshot, A. Fischer, R. Podila, A.M. Rao, C. Daraio, RSC Adv. 5 (2015) 29306–29311.

[142] X.-F. Li, K.-T. Lau, Y.-S. Yin, Compos. Sci. Technol. 68 (2008) 2876–2881.

[143] K. Lau, M. Lu, K. Liao, Compos. Part A Appl. Sci. Manuf. 37 (2006) 1837–1840.

[144] Q. Zeng, H. Tian, J. Jiang, X. Ji, D. Gao, C. Wang, RSC Adv. 7 (2017) 7375–7381.

[145] A. Leela Mohana Reddy, R.I. Jafri, N. Jha, S. Ramaprabhu, P.M. Ajayan, J. Mater. Chem. 21 (2011) 16103.

[146] R.B. Rakhi, W. Chen, H.N. Alshareef, J. Mater. Chem. 22 (2012) 5177.

[147] S. Amelinckx, X.B. Zhang, D. Bernaerts, X.F. Zhang, V. Ivanov, J.B. Nagy, Science (80-.). 265 (1994) 635–639.

[148] P.R. Bandaru, C. Daraio, K. Yang, A.M. Rao, J. Appl. Phys. 101 (2007) 094307.

[149] W. Wang, K.Q. Yang, J. Gaillard, P.R. Bandaru, A.M. Rao, Adv. Mater. 20 (2008) 179–182.

[150] K. Nishimura, L. Pan, Y. Nakayama, Jpn. J. Appl. Phys. 43 (2004) 5665–5666.

[151] J.A. Robinson, E.S. Snow, Ş.C. Bădescu, T.L. Reinecke, F.K. Perkins, Nano Lett. 6 (2006) 1747–1751.

[152] P.R. Bandaru, H. Yamada, R. Narayanan, M. Hoefer, Mater. Sci. Eng. R-Reports 96 (2015) 1–69.

[153] S. Ihara, S. Itoh, J. Kitakami, Phys. Rev. B 48 (1993) 5643–5647.

[154] B. Ashrafi, J. Guan, V. Mirjalili, P. Hubert, B. Simard, A. Johnston, Compos. Part A Appl. Sci. Manuf. 41 (2010) 1184–1191.

[155] M. Cinke, J. Li, B. Chen, A. Cassell, L. Delzeit, J. Han, M. Meyyappan, Chem. Phys. Lett. 365 (2002) 69–74.

[156] R. Smajda, Á. Kukovecz, Z. Kónya, I. Kiricsi, Carbon N. Y. 45 (2007) 1176–1184.

[157] S. Inoue, N. Ichikuni, T. Suzuki, T. Uematsu, K. Kaneko, J. Phys. Chem. B 102 (1998) 4689–4692.

[158] Á. Kukovecz, T. Kanyó, Z. Kónya, I. Kiricsi, Microporous Mesoporous Mater. 80 (2005) 85–94.

[159] G. Onyestyák, J. Valyon, K. Hernádi, I. Kiricsi,, L.V.C. Rees, Carbon N. Y. 41 (2003) 1241–1248.

[160] H. Muramatsu, T. Hayashi, Y.A. Kim, D. Shimamoto, Y.J. Kim, K. Tantrakarn, M. Endo, M. Terrones, M.S. Dresselhaus, Chem. Phys. Lett. 414 (2005) 444–448.

[161] J.-H. Han, H. Zhang, M.-J. Chen, G.-R. Wang, Z. Zhang, Compos. Sci. Technol. 103 (2014) 63–71.

[162] S. Wang, Z. Liang, G. Pham, Y.-B. Park, B. Wang, C. Zhang, L. Kramer, P. Funchess, Nanotechnology 18 (2007) 095708.

[163] A.M. Díez-Pascual, J. Guan, B. Simard, M.A. Gómez-Fatou, Compos. Part A Appl. Sci. Manuf. 43 (2012) 1007–1015.

[164] F.S. Chakar, A.J. Ragauskas, Ind. Crops Prod. 20 (2004) 131–141.

[165] K.A. Shah, B.A. Tali, Mater. Sci. Semicond. Process. 41 (2016) 67–82.

[166] W.-H. Hung, S.L. Bernasek, Surf. Sci. 339 (1995) 272–290.

[167] R. Andrews, D. Jacques, A.M. Rao, F. Derbyshire, D. Qian, X. Fan, E.C. Dickey, J. Chen, Chem. Phys. Lett. 303 (1999) 467–474.

[168] L. Samandari-Masouleh, N. Mostoufi, A. Khodadadi, Y. Mortazavi, M. Maghrebi, Ind. Eng. Chem. Res 51 (2012) 1143–1149.

[169] K. Kuwana, K. Saito, Carbon N. Y. 43 (2005) 2088–2095.

[170] G.J.M. Dormans, J. Cryst. Growth 108 (1991) 806–816.

[171] K. Kuwana, H. Endo, K. Saito, D. Qian, R. Andrews, E.A. Grulke, (n.d.).

[172] M.R. Hyman, D.J. Arp, 53 (1987) 298–303.

[173] S.B. Sinnott, R. Andrews, D. Qian, A.M. Rao, Z. Mao, E.C. Dickey, F. Derbyshire, Chem. Phys. Lett. 315 (1999) 25–30.

[174] M. Hoefer, P. Bandaru, J. Electrochem. Soc. 160 (2013) H360–H367.

[175] A. Jorio, M.M. Lucchese, F. Stavale, E.H.M. Ferreira, M.V.O. Moutinho, R.B. Capaz, C. a Achete, J. Phys. Condens. Matter 22 (2010) 334204.

[176] L. Pan, M. Zhang, Y. Nakayama, J. Appl. Phys. Appl. Phys. Lett. 91 (2002).

[177] M. Hoefer, P.R. Bandaru, Appl. Phys. Lett. J. Appl. Phys. 95 (2009) 183108–34308.

[178] J.A. Nichols, H. Saito, C. Deck, P.R. Bandaru, J. Appl. Phys. 102 (2007) 064306.

[179] J.A. Robinson, E.S. Snow, Ş.C. Bădescu, T.L. Reinecke, F.K. Perkins, Nano Lett. 6 (2006) 1747–1751.

[180] V.A. Sinani, M.K. Gheith, A.A. Yaroslavov, A. Anna, K. Sun, A.A. Mamedov, J.P. Wicksted, N.A. Kotov, A.A. Rakhnyanskaya, Phys. Rev. Lett. (2005) 3463–3472.

[181] G. Milczarek, in:, 9th IEE Conf. Nanotechnology, IEE NANO, 2009, p. 5394616.

Appendix A: LabView diagrams

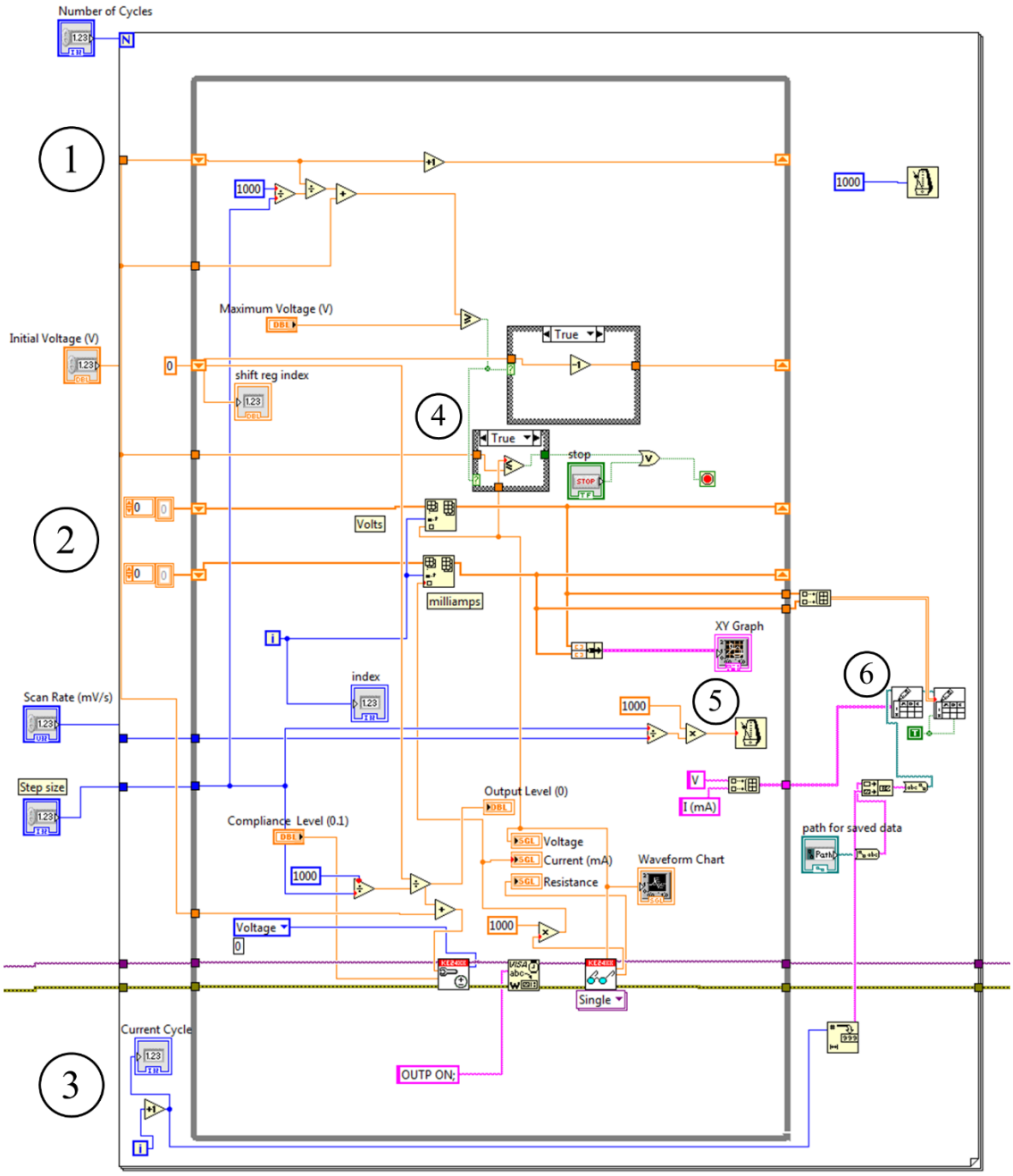

Figure A1: program for cyclic voltammetry.

The program in Figure A1 is constructed around the Keithley 2400 “read single” VI that can be downloaded from the National Instruments VI database. It enables a user to connect with a Keithley 2400, set the current or voltage, and read the output. It should be noted that this program was made using LabView 2014, and certain Vis may be obsolete in later versions. For example, as of this writing, the read/write VIs that output the data to text files have been replaced by newer iterations in LabView 2017. If replication of these programs is attempted, the user should understand this and be flexible in using new Vis. The modifications to the “read single” VI are built around the “configure output” and “read” VIs that are found in the lower center of the diagram. The sub-VIs that connect to and configure the Keithley 2400 are also included, but are not shown here. User inputs such as initial voltage, scan rate, and step size are seen on the left of the diagram outside of the loops. The inner loop is a “While loop” that will continue to ramp the voltage until a target voltage is met. The outer loop is a “For loop” that allows the user to set the number of cycles to execute. A shift register is used in conjunction with a loop and stores data from one loop iteration to the next. The lateral orange lines crossing the inner loop are shift registers. Some important features are explained below.

1: This shift register increments the voltage and tells the Keithley 2400 what voltage to output. Once the voltage reaches or exceeds the maximum voltage setting, the voltage increment is multiplied by -1 so that the voltage will then be subtracted from the maximum value until the initial voltage is reached.

2: These two shift registers acquire the current and voltage measurements from the “Read” VI and put the values into arrays which are displayed in the XY graph and output as data in a text file.

3: The “i” in the corner is an index counter. It begins at zero and increases by one for each loop iteration. For the outer loop, the index is used to indicate the current CV cycle. There is also an

index counter within the inner loop. In that case it is used to order the current and voltage values that are added to their respective arrays.

4: Here can be found two case squares. Their functions change depending on whether the input is true or false. The top in is used to decrement the voltage once the maximum voltage is reached while the bottom one is used to terminate the loop once the initial voltage is reached.

5: The metronome controls the delay time between loop iterations. In this case it is controlled by the scan rate and step size inputs from the user.6: This block that is outside the inner loop creates the data files compiled from the current and voltage values. The names of the data files are suffixed with the cycle increment, so that each CV cycle will have its own file.

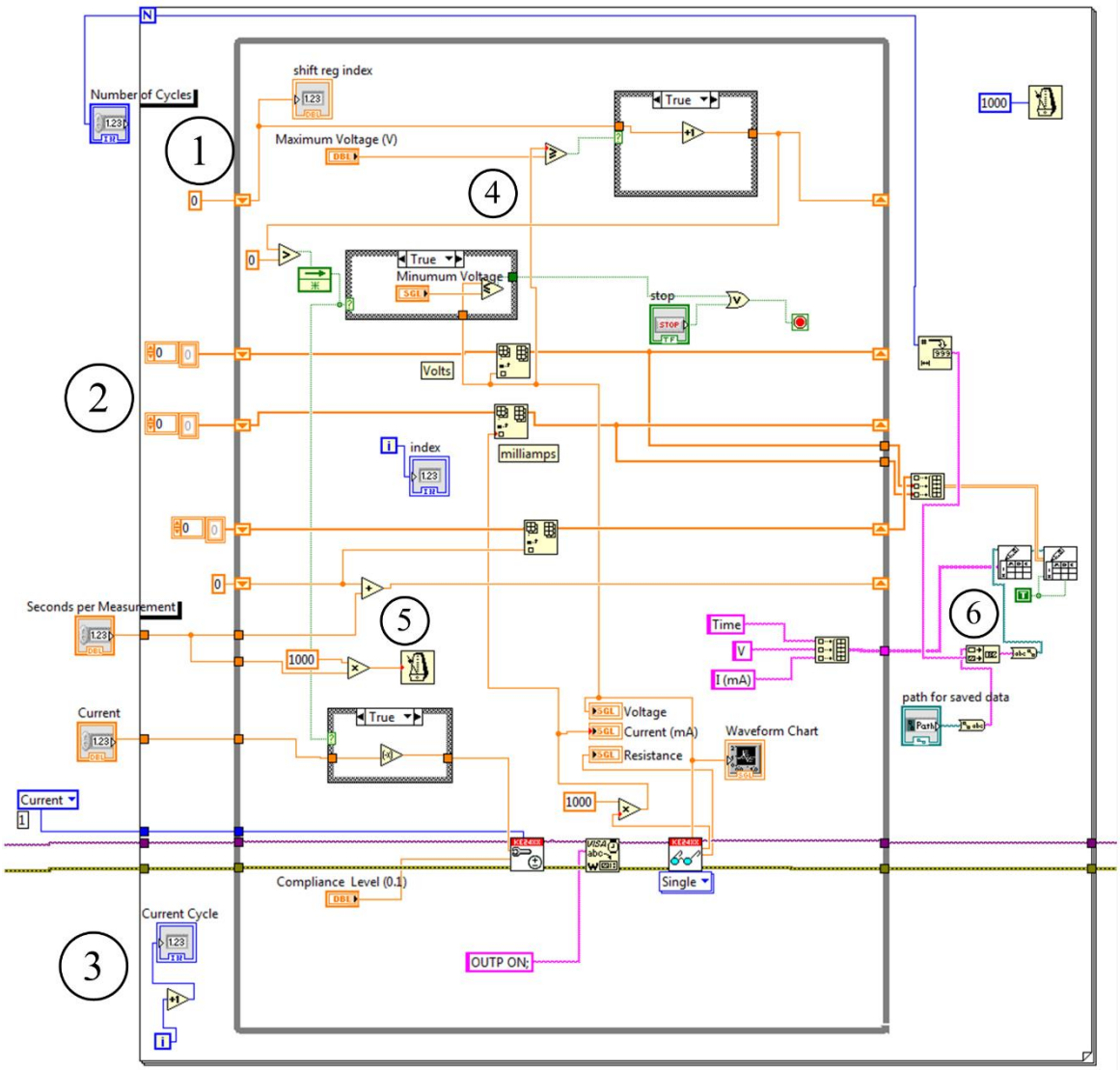

Figure A2: Charge/discharge program

This program is similar to the previous except that instead of sweeping the voltage and recording current, the current is held constant and the change in voltage is recorded. The numbered points are used for the same mechanisms outlined above.